Mikko Ruskola

Numerical Modelling of Pulsed Electric Current Sintering Process

School of Chemical Technology

Thesis submitted for examination for the degree of Master of Science in Technology.

Espoo 14.9.2014

Thesis supervisor:

Prof. Simo-Pekka Hannula

Thesis advisor:

M.Sc. (Tech.) M. Erkin Cura

Aalto University
School of Chemical Technology

AALTO UNIVERSITY
SCHOOL OF CHEMICAL TECHNOLOGY

ABSTRACT OF THE
MASTER'S THESIS

Author: Mikko Ruskola

Title: Numerical Modelling of Pulsed Electric Current Sintering Process

Date: 14.9.2014 Language: English Number of pages:7+88

Department of Materials Science and Engineering

Professorship: Materials Science Code: MT-45

Supervisor: Prof. Simo-Pekka Hannula

Advisor: M.Sc. (Tech.) M. Erkin Cura

The goal of this thesis was to construct a finite element model (FEM) for numerical simulation of pulsed electric current sintering. Coupled thermal–electrical and thermal–electrical–mechanical models were constructed. The models were constructed as stationary, time dependent or PID controlled time dependent versions. Materials properties required for accurate modelling were determined. Differences in results using conducting and non-conducting samples were evaluated. Densification of copper was modelled by implementing the master sintering curve (MSC) method into FEM model. Complex shaped compacts made out of WC-12Co were sintered, characterized and modelled.

The models constructed for this thesis can simulate evolutions in temperature, voltage, current and stress distributions amongst others. The simulations can be used as a design tool to mitigate thermal gradients and high stresses which can have undesirable effects on products. In cases such as sintering of functionally graded materials (FGM) large thermal gradients may be desirable and can be evaluated for different designs using FEM.

The constructed models were validated against experimental results correlating well. Simulated density evolution of copper using MSC correlated with experimental results. Compacts with complex geometries were sintered to full density from WC-12Co powder. However cracks were detected in one of the moulds. Simulations indicated high stress concentration in the crack locations. The compacts had uniform hardness and no differences in microstructures were detected. This thesis demonstrates the usefulness of FEM modelling when designing products for PECS production.

Keywords: PECS, Sintering, Powder Metallurgy, FEM, modelling, WC-12Co

AALTO-YLIOPISTO
KEMIAN TEKNIIKAN KORKEAKOULU

DIPLOMITYÖN
TIIVISTELMÄ

Tekijä: Mikko Ruskola

Työn nimi: PECS sintrauksen numeerinen mallinnus

Päivämäärä: 14.9.2014 Kieli: Englanti Sivumäärä:7+88

Materiaalitekniikan laitos

Professuuri: Materiaalitiede Koodi: MT-45

Valvoja: Prof. Simo-Pekka Hannula

Ohjaaja: DI M. Erkin Cura

Tämän diplomityön tarkoituksena oli PECS sintrauksen numeerinen mallinnus elementtimenetelmällä (FEM). Työtä varten rakennettiin elementtimallit, joissa on yhdistetty sähköiset- ja lämpöilmiöt sekä sähköiset-, lämpö- ja mekaanisetilmiöt. Mallit rakennettiin stationäärisinä sekä ajasta riippuvaisina, PID-ohjauksen kanssa ja sitä ilman. Mallien avulla arvioitiin sähköä johtavien ja eristävien näytteiden aiheuttamia eroja tuloksissa. Master sintering curve (MSC) menetelmää käytettiin kuparin tiheyden kehityksen arviointiin ja se implementoitiin FEM-malliin. Koostumukseltaan WC-12Co näytteitä sintrattiin monimutkaisiin muotoihin. Näytteet karakterisoitiin ja prosessi mallinnettiin.

Tätä työtä varten rakennetut mallit pystyvät simuloimaan muun muassa lämpötilan, jännitteen, virran ja mekaanisenjännityksen kehitystä. Simulaatioita voidaan käyttää suunnittelutyökaluina lämpötilaerojen ja rasitustilojen hallinnassa. Esimerkiksi funktionaalisia gradienttimateriaaleja (FGM) valmistettaessa voi olla tarkoituksenmukaista sintrata kappaleita suuria lämpötilaeroja hyväksi käyttäen. Lämpötilagradientti voidaan suunnitella FEM-menetelmällä.

Rakennettujen mallien tulokset vahvistettiin vertaamalla niitä kokeellisiin tuloksiin. Verratut tulokset korreloivat hyvin. MSC menetelmää käyttäen simuloitu kuparin tiheyden kehitys vastasi hyvin kokeellisesti mitattuja arvoja. WC-12Co näytteet sintrautuivat täyteen tiheyteen, mutta yhteen muottiin oli syntynyt säröjä. Monimutkainen geometria aiheutti simulaatiotulosten mukaan jännityskeskittymän säröjen sijaintiin. Näytteille suoritetut kovuusmittaukset eivät näyttäneet eroa näytteiden välillä eikä näytteiden eri osissa. Näytteiden mikrorakenteissa ei myöskään havaittu eroja. Tämän työn perusteella elementtimenetelmällä tehtävä mallinnus on hyödyllinen työkalu PECS:llä tehtävän tuotannon suunnittelussa.

Avainsanat: PECS, FEM, Sintraus, Mallinnus, jauhemetallurgia, WC-12Co

Preface

This Master's thesis was written at Aalto University School of Chemical Technology as a part of "PM Products with New Material and Processing Solutions" project. The participants of the project are Aalto University School of Chemical Technology, Carbodeon Ltd Oy, Metso Minerals Finland Oy, VTT Technical Research Centre of Finland and Wärtsilä Finland Oy.

I would like to give my greatest thanks to my instructor Erkin Cura, and Juho Lotta who have shared their experience and wealth of knowledge with me. Their advice has been invaluable. I would also like to thank my thesis supervisor, Professor Simo-Pekka Hannula, for giving me the chance to work on such an interesting subject matter.

This thesis reminded me on the importance of the people that surround you. Without their contributions, from advice on sample preparation to tossing ideas back and forth the entire job would have been far more arduous. I would like to give special thanks for Into Niilo-Rämä from the workshop, who helped the research significantly by quickly machining graphite parts, and Jussi Puutala from University of Oulu for his help in measuring thermal properties of graphite. I would also like to thank Tuomas Riipinen, Katri Honkanen and Henrika Granbohm as well as the entire crew at the MOP coffee table for their company and advice.

Espoo, 14.9.2014

Mikko Ruskola

Contents

Abbreviations

Abbreviations

CTE	Coefficient of Thermal Expansion
DC	Direct Current
ECAS	Electric Current Activated Sintering
EDS	Electric Discharge Sintering
FAST	Field Assisted Sintering
hBN	Hexagonal Boron Nitride
FE-SEM	Field Emission Scanning Electron Microscope
FEM	Finite Element Method
FEA	Finite Element Analysis
FGM	Functionally Graded Material
HP	Hot Pressing
HIP	Hot Isostatic Pressing
LPS	Liquid Phase Sintering
MSC	Master Sintering Curve
P^2C	Plasma Pressure Compaction
PAS	Plasma Activated Sintering
PDE	Partial Differential Equation
PDS	Pulse Discharge Sintering
PECS	Pulsed Electric Current Sintering
SPS	Spark Plasma Sintering
RS	Resistance Sintering
SEM	Scanning Electron Microscope
UHTC	Ultra-High-Temperature Ceramics

1 Introduction

Pulsed Electric Current Sintering (PECS) is a process which can be used to both synthesize and consolidate materials. It is a pressure assisted sintering technique similar to hot pressing. In PECS particulate materials are sintered by applying pulsed direct current and pressure whereas hot pressing (HP) uses radiant heat generated by heating elements. PECS is a form of resistance sintering (RS) which works by using the Joule heating mechanism to convert electricity into heat in the mould and in conductive powders. PECS differentiates itself from other types of resistance sintering methods by the usage of pulsed current.

The following chapters give background on sintering and explain the fundamentals of PECS, state of the art in PECS research and a short introduction to the basics of the Finite Element Method (FEM). The experimental part of this thesis contains measurements done using the PECS apparatus for conducting and non-conducting samples, and sintering of powders. In the next part, a FEM model was constructed and presented using the data acquired during the experiments. Densification of copper is simulated by the master sintering curve (MSC) approach employing FEM. Compacts with complex geometries were also sintered from WC-12Co. Lastly the experimental and simulation results are compared and analysed.

1.1 Background

PECS allows for sintering of multitude of different types of materials from metals to ceramics and organic composites to functionally graded materials (FGM). The primary benefits of PECS include fairly short process times and relatively low energy usage. While PECS has unique benefits over conventional sintering processes it also has its drawbacks. The drawbacks include thermal and stress gradients in the sample which can lead to heterogeneous microstructure and cracking, also the mechanical properties of the moulds set limitations on the process. The drawbacks can be mitigated using different tools and approaches.

FEM is a numerical analysis method often used in computational physics and it was chosen for this work due to its versatility. It uses a calculation mesh to divide the model into smaller elements and different algorithms for solving the Partial Differential Equations (PDE) associated with the mesh nodes.

1.2 Objectives

This thesis investigates the evolution of thermal and electric gradients, and stresses emerging as their result in PECS process by using FEM simulations in combination with practical experiments. Construction and validation of stationary and time dependent models for different geometries was carried out by incorporating experimental data and simulations. In the process both conducting and non-conducting samples were considered. While most of the earlier modelling efforts have concentrated on cylindrical samples this thesis also simulated more complex geometries to find and possibly solve problems associated with them.

2 Sintering

Sintering is a process where metal and/or ceramic powders are compacted by application of thermal energy. While sintering of materials has been known and used for thousands of years, most of the scientific knowledge and theory have only been developed since after the second world war [1]. A multitude of different sintering techniques have been developed. These include solid state sintering, liquid phase sintering (LPS), pressure-less sintering, pressure assisted sintering and novel methods such as microwave sintering. The novel sintering methods are in fact derivatives of former methods as is PECS. [2]

2.1 Conventional Sintering Techniques

2.1.1 Pressure-less Sintering

Pressure-less sintering methods are the oldest sintering techniques, while oldest they are still in use by the industry [2]. Pressure-less sintering can be defined as material transport caused by the driving force of decreasing surface energy, resisting the driving force is the grain boundary energy. However the grain boundary energy is significantly smaller than surface energy for most materials [3]. One of the benefits of pressure-less sintering is the ability to sinter more complex shapes than with pressure assisted methods, where significant machining of the parts may be required [4]. However without the addition of pressure the final density is commonly lower [1]. Pressure-less sintering is especially useful in cases where full density is not desired, examples of this are steel plants sintering fine iron particles to larger agglomerates allowing them to be used in blast furnaces [5].

2.1.2 Solid State Sintering

Solid state sintering can be performed with and without pressure, and is the most well understood of the sintering techniques. In solid state sintering the particles bond together in a temperature below the melting point of the particles. [2] Solid state sintering can be divided to initial, intermediate and final stages which overlap each other. Neck formation between the particles happens in the initial stage with little overall densification, the intermediate phase contributes majority of the densification, while in the final stage trapped pores are eliminated. [6]

Solid state sintering can be explained as a process of reducing surface energy of powder particles by decreasing their surface area, which causes the formation

of a unified body. The aforementioned reduction in surface energy is what allows sintering to take place below the melting point of the material. When the surface energy of solid-vapour interface has decreased to that below of solid-solid interface the grain size starts to coarsen. Since both sintering and grain growth operations reduce the surface energy, they also happen simultaneously in practice. [2, 6]

2.1.3 Liquid Phase Sintering

Liquid phase sintering is commonly used in industry due to the increased densification rates caused by the presence of the liquid phase. The liquid phase is usually formed by a melting alloying element or reaction between powders [1]. The liquid phase may be present in the process momentarily or during the entire high temperature part of the sintering cycle. The liquid phase eliminates pores by flowing between the particles, however the microstructure also coarsens rapidly and degrades some of the materials properties of the compact [6]. Figure 1 shows a schematic representation of microstructure evolution during LPS [7].

2.1.4 Pressure Assisted Sintering

Pressure assisted sintering techniques include hot pressing (HP), and hot isostatic pressing (HIP) and hot forging. Pressure assisted techniques are often used for powders which fail to achieve desired densities using pressure-less sintering. Adding pressure to the sintering process allows for lower sintering temperatures, reducing the grain growth [3]. An extreme example of pressure sintering is explosive compaction of powders which requires no additional heating [8]. Addition of pressure to the sintering process also adds mechanisms, these include plastic deformation and creep [1].

In hot pressing uni-axial pressure is applied to the heated powder or a green compact which is constrained by a die [3]. Hot forging, which is sometimes referred to as sinter forging, uses a green or partially sintered compact that is subjected to uni-axial pressure between two plates without the constraint of the die. The lack of a die means no pressure is applied in the lateral direction unlike in the case of hot pressing [9].

Hot isostatic pressing can be performed to both powders or predensified compacts. If powders are used they must be in an enclosed container. HIP uses hydrostatic pressure which is transmitted through gas, the pressure will collapse the powder container if one is used. Because the pressure is applied uniformly the densification is more homogeneous as compared to HP. Dies used in other pressure

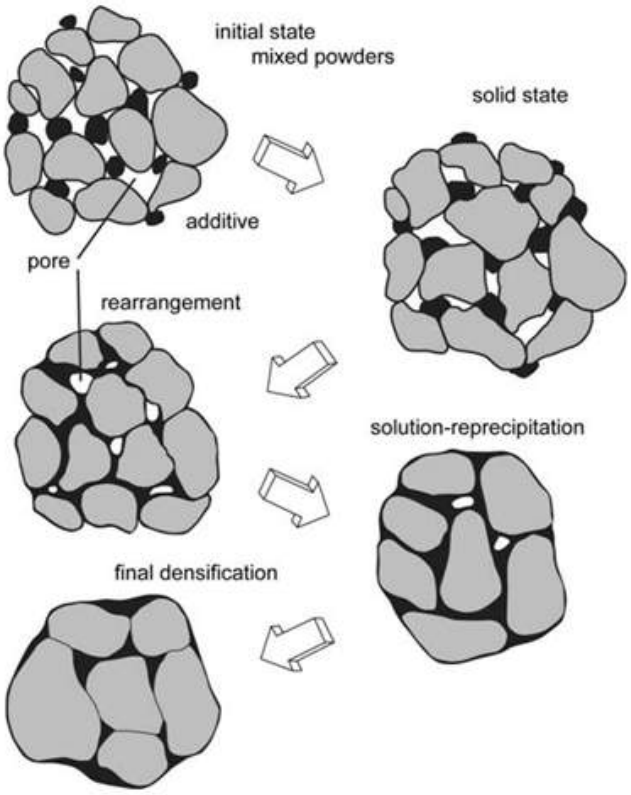

Figure 1: A schematic representation of microstructural changes taking place during LPS. The process starts similarly to solid state sintering, however when the temperature is high enough the melting of particles causes rearrangement and the liquid phase encourages coarsening of the microstructure [7].

assisted methods can not withstand the combination of heat and pressure that is possible with HIP. [3, 9]

The direction of applied pressure can have effect on the structure of the product, as is the case with uni-axial pressure the grains may align perpendicular to the direction of the applied force. The alignment of pores can have detrimental or desired effect on the mechanical properties of the product. [10]

2.2 Novel Sintering Techniques

Novel and new sintering methods are developed with faster process times, lower temperatures, improved materials properties or complex geometries in mind. Some of these novel sintering techniques are microwave sintering, reactive sintering, electric discharge sintering and resistance sintering.

2.2.1 Microwave sintering

Microwave sintering works by converting electromagnetic waves into heat in the material being sintered. Benefits of this sintering technique include high heating rates, fast process times and saving energy [1]. However due to the nature of the technique it is used on ceramics and polymers as metals tend to reflect the energy instead of heating up. Microwave heating in combination with conventional heating can produce an uniform temperature profile, this method can be used to avoid issues such as dis-uniformity and cracking due to thermal gradients [11].

2.2.2 Reactive Sintering

Reactive sintering uses a mixture of powders that have the ability to start a self propagating reaction if conditions for the reaction are met. The method can be used for rapid densifications, however an uncontrolled reaction may simply result in powder. To improve densification uni-axial pressure or hydrostatic pressure may be applied. [1, 9]

2.2.3 Resistance Sintering

Resistance Sintering (RS) exists in various forms, using the electrical resistance of the sintered materials to generate the heat required through Joule heating effect. An early example of resistance sintering was manufacturing of filaments for incandescent bulbs in 1906 [12] using direct current (DC). Various forms of resistance sintering have been developed since, including electric discharge sintering, and pulsed electric current sintering which will be discussed in detail in the following chapter.

2.2.4 Electric Discharge Sintering

Electric Discharge Sintering (EDS) uses capacitor banks to store energy which is released with both high voltage and current to the powder stored in an electrically insulated vessel. Density increases have been observed up to three discharges. EDS is a very rapid process, and the sintering times are typically under 0,01 s [1]. In addition to Joule heating the technique takes advantage of electromagnetic phenomena which causes an intense but quickly collapsing magnetic field to pull the material together that improves the densification [13].

3 Pulsed Electric Current Sintering

Pulsed Electric Current Sintering (PECS) is a technique where pulsed current and uni-axial pressure act simultaneously on a powder. The technique uses electric current to improve sintering kinetics making higher densities possible at lower temperatures. High heating rates are also typical to PECS due to the Joule heating effect. [1]

PECS is often called as Spark Plasma Sintering (SPS), even though presence of plasma during the process is still controversial. Other names used for the same process include Field Assisted Sintering (FAST), Electric Current Activated Sintering (ECAS), Pulse Discharge Sintering (PDS), Plasma Activated Sintering (PAS) and Plasma Pressure Compaction (P^2C) [14].

3.1 Background

Pulsed Electric Current Sintering is a process where powdered material or ready made pressed compacts are consolidated under the simultaneous influence of current generated heat, and uni-axial pressure. The heat in the process is a function of the Joule heating which is caused by a current flowing through the die (non-conductive compact) or both the die and the compact (conductive compact) [14]. The electric current improves sintering kinetics by making higher densities possible at lower temperatures [1]. Due to the mechanical properties of the used graphite parts in the process the applied pressure is generally under 100 MPa, although it is possible to use pressures up to 250 MPa with specially designed dies [15]. A schematic of a PECS apparatus can be seen in Figure 2.

While resistance sintering has existed since the early 20th century, the use of pulsed current in sintering was not introduced until 1966 by Inoue [16] in Japan. Sumitomo coal, also located in Japan, developed the first commercial PECS equipment in 1990 [17]. Interest in the PECS process has increased since late 1990's. This is demonstrated by the exponential increase in number of papers published on the subject shown in Figure 3. Japan has led the commercialization of PECS and thus most of the early research has been published by Japanese researchers though more recently China has taken the lead in most articles published on the subject yearly [14].

Research has shown that PECS has numerous advantages over the more conventional sintering processes. Some of the advantages are lower energy usage, faster heating rates [1], lower holding time and improved materials properties. The im-

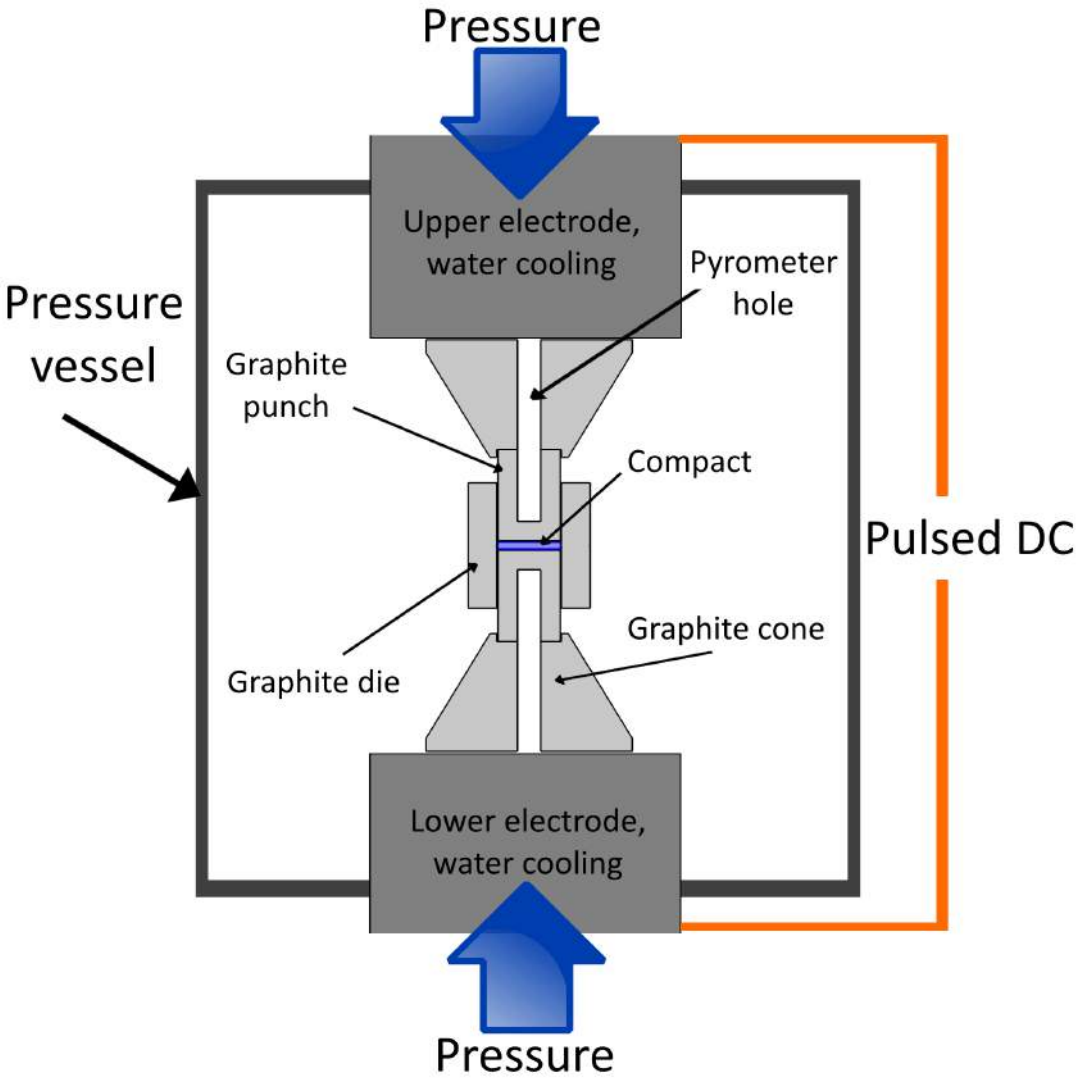

Figure 2: A schematic representation of the SPS apparatus.

provements in materials properties are caused by finer micro structure and less segregation of impurities at the grain boundaries in addition to high density. [14, 18]

While PECS has its advantages there exists disadvantages as well. The geometries of the manufactured parts are generally quite simple, the production of near net shape objects is problematic. The size of the SPS compacts so far has been limited to 400 mm in diameter at the high end. Another disadvantage may be the unsuitability or lack of durability of the graphite dies used in the process, for serial industrial production more durable dies may have to be constructed. Steel dies can be used at temperatures below 1000 °C [19].

The heating in PECS is a function of the geometry and both the thermal and

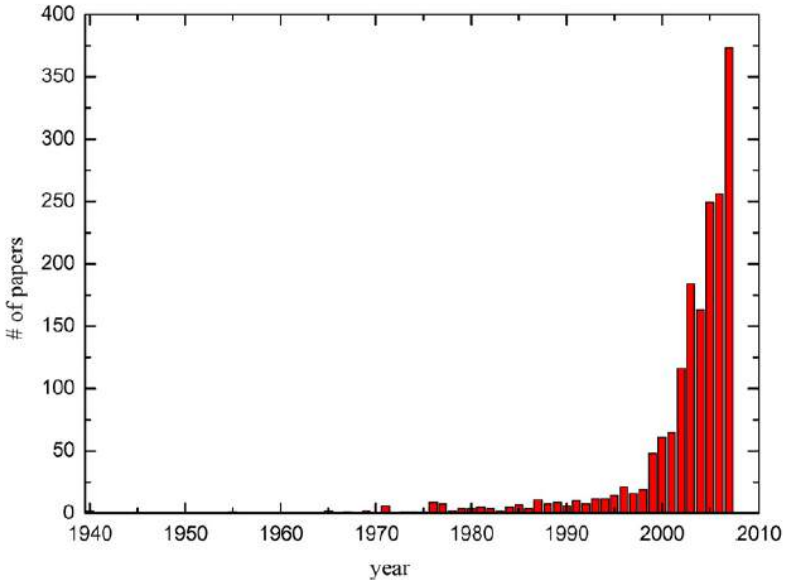

Figure 3: Increasing number of publications on PECS. [14]

electrical properties of materials used. Joule heating allows for very high heating rates, 1200 °C/min is the highest heating rate reported for commercial equipment, while 100-400 °C/min are more common. Similarly to other sintering techniques the products sintered by PECS are sensitive to changes in temperature and stress distributions, thus density of the product can vary, this can be mitigated by taking the geometry to account in the die design.[14, 18, 19] In conventional HP and HIP sintering the heating times are far longer because the heat is usually applied through radiation or by convection through the process gasses. In case of HP the sintering duration can be as long as tens of hours [1].

3.2 Effects of Sintering Parameters

Important parameters affecting PECS are sintering temperature, furnace atmosphere, electrical current, voltage, pressure, and holding time [14]. While pulsed current is known to have an effect on the product the exact reasons remain unknown [20, 21]. In addition the current density has been shown to affect the microstructure of the product [18].

The PECS process uses high currents, commonly in the kilo-ampere range, but low voltages, commonly below 10 V. The current is pulsed in patterns which consists of pulses and pauses between them. The patterns are denominated for example by 8:4 which can mean 8 current pulses and a pause duration of 4 pulses or pulsed current for duration of 8 ms and pause for duration of 4 ms, this depends on the

equipment in use. Pulse durations are often in the millisecond range. [14, 19]

Multiple studies on the effects of pulse patterns have been conducted. Xie et al. [21] found that when sintering Al powders the pulse frequency had no effect on the density, resistivity or tensile properties of the product. In another study Chen et al. [20] investigated pulsing of DC current and its effect on reactivity in PECS. Their experimental setup had a low resistivity p-type (100) silicon wafer sandwiched between molybdenum foils. The pulse durations were 3 ms and the pulse patterns used were 2:8, 8:2, 12:2, 7:7 (on:off) in temperature range 1070 – 1270 °C. The experiments produced no measurable change in product layer growth rate depending on the pulse pattern. Also the growth rate of the product layer did not depend on the current direction as shown in a later study [22]. They also noted that with their equipment (Sumitomo, Model 1050) the pulses themselves were not square waves and had varying peaks increasing with the off time, but that the RMS current stayed the same regardless of the pattern.

Results by Santanach et al. [23] on effects of different pulse patterns on α-alumina–hematite powders contrast the above mentioned results. While they also found that changing of the pulse pattern affected the current crest intensities, they found that this had a marked influence on the microstructure of the product. Figure 4 shows scanning electron microscope (SEM) micrographs of compacts sintered using three different pulse patterns but with other sintering parameters kept constant. They suggest that the microstructural differences may be partly caused by differences in local temperatures inside the sample caused by variations in the pulse patterns.

The sintering temperature is dependent on the current used and electrical properties of the graphite and the sintered material due to the Joule heating effect. The current also has an effect on mass transport. Direct or pulsed current has effect on increasing electro-migration, defect mobility and point defect generation [20]. Phase nucleation and formation rate of intermetallic product layers are increased when the current is increased [24].

Anselmi-Tamburini et al. [22] studied the effect current on solid-state reactivity in PECS by using molybdenum foil sandwiched between silicon wafers (100). The set-up was subjected to 30 MPa of compressive pressure. The sandwich construction allowed them to see if the current direction had any effect on the product layer, which it did not. Unlike the current direction the current itself increased product layer growth. Their experiments showed that the activation energy for product formation when current was applied was similar to that without current thus they proposed

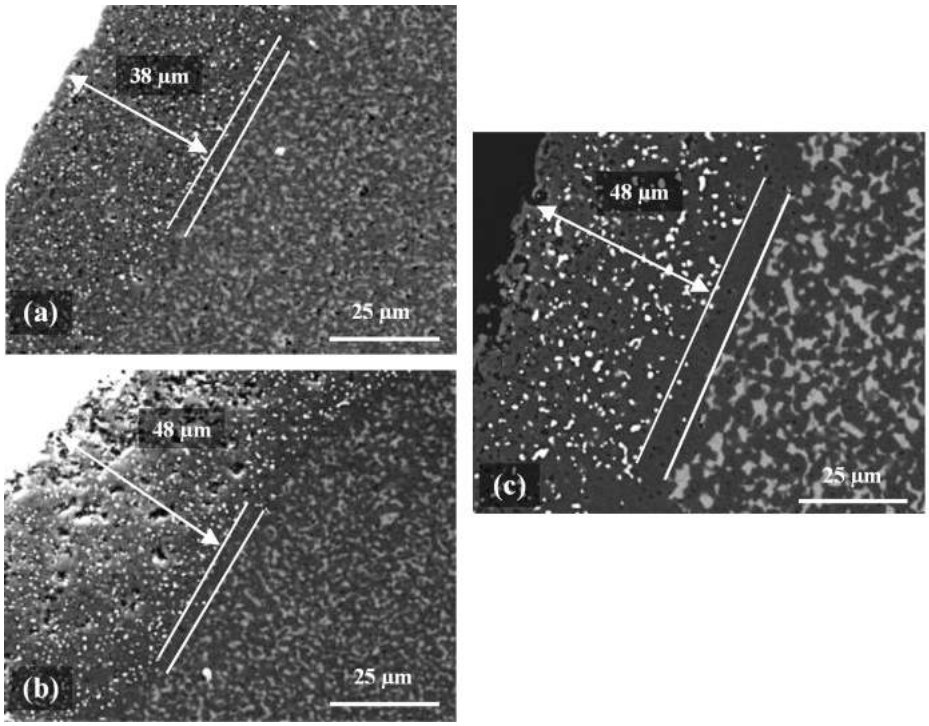

Figure 4: Effect of pulse patterns on sintered α-alumina–hematite compacts. The pulse duration was 3.3 ms and the patterns (on:off) used were following; (a) 12:2, (b) 2:2 and (c) 2:6. [23]

no change in reaction mechanism but that the current enhances mass transport.

The pressure used in the process affects the densification both intrinsically and extrinsically. The intrinsic effects of the pressure include an increase in the chemical potential, increased viscous flow, plastic flow and creep. The extrinsic effects of pressure include particle rearrangement and dispersion of agglomerates. [25]

Makino et al. [26] conducted a study on behaviour of ultra-fine α-alumina powders under varying pressure. Their results show that particulate size of the powder had an effect on densification under the influence of 30 MPa pressure while such an effect was not present under the influence of 100 MPa. Their study also showed increased grain growth suppression with increased pressure.

Quach et al. [27] investigated the the effect of pressure and grain growth in nanostructured fully stabilized zirconia sintered with PECS. Their experiments showed that the applied uniaxial pressure had a marked effect on densification when sintering was performed at lower temperatures but the effect of the pressure was decreased significantly at higher temperatures, the results are shown in Figure 5. Their results indicated that pressure had no effect on average grain size. Their results also demonstrated overall reduced grain growth, which is possibly the result of current

having an effect on grain boundary energy or how the dopants were segregated. In another study conducted by Chen et al. [28] on PECS of $Pb(Mg_{1/3}Nb_{2/3})O_3$-$PbTiO_3$ the results suggest the direct influence of thermo mechanical fatigue induced by the current on reduced grain growth.

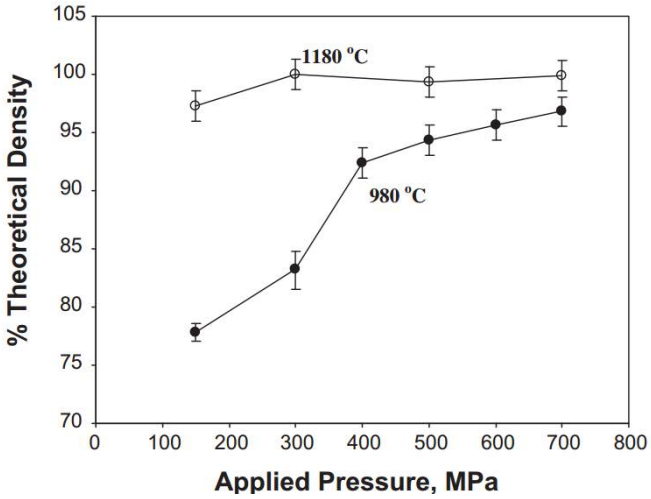

Figure 5: Effect of pressure on densification of c-YSZ samples sintered at two different temperatures with 5 minute dwell period. [27]

Effect of pressure was also studied by Santanach et al. [29] by applying 10, 30, 50 and 100 MPa of pressure at 1500 °C with 180 s dwell time to 140 nm α-Al_2O_3 powder. The results of this test showed grain size increasing with pressure going from 4.3 μm (10 MPa) to 7.5 μm (100 MPa) while the density stayed almost unchanged. Changing the temperature where the high pressure (100 MPa) was first applied increased the density with the starting point 600 °C giving 98.9% relative density and 1200 °C 99.7%, the dwell time used was 180 s. While the by and large independence of the final density from pressure agrees with results obtained by Quach et al. [27], contrasting them is the increased grain growth with increased pressure.

Experiments were performed by Olevsky et al. [30] on the impact of the typically high heating rates of PECS on densification. In their experiments they used aluminium powder with average particle size of 75 µm and composition Al-17Si-5Fe-3.1Cu-1.1Mg-0.6Zr (wt.%). The compacts were 30 mm in diameter and contained 25 g of the powder, the pressures used in the sintering ranged up to 121 MPa at 150 °C and above. Heating rates used in the experiment were 50, 100 and 200 °C/min with the temperature topping at 450 °C. They calculated the densification from by using the relative piston travel during the sintering process and relative densities of

the compacts. Their experiments showed that the densification increased with faster heating rates and that with higher heating rate the densification preferred higher temperatures compared to slower heating rates, the results can be seen in Figure 6. They explain the change in the densification rate at higher heating rates by changes in pore tip sharpness evolution. They also studied how the particle size affected densification with larger particles having higher shrinkage and bigger shift to higher temperature shrinkage. They suggested that in certain cases bigger particles might result in better densification at high heating rates, though they note that this did not apply to lower heating rates.

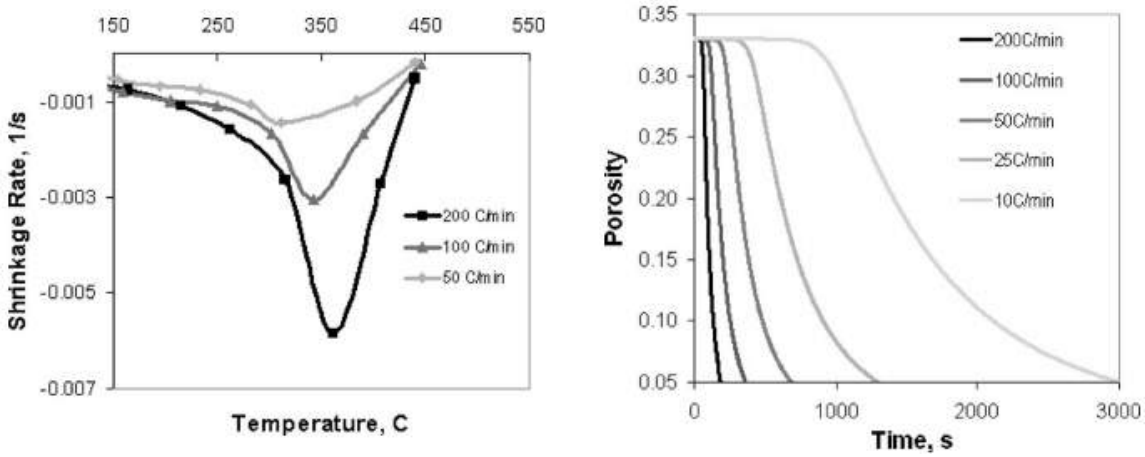

Figure 6: Effect of heating rates on densification. [30]

The relationship between grain growth and densification was investigated in a study on sintering of 140 nm α-Al_2O_3 powder using PECS by Santanach et al. [29]. They showed grain growth happening sans significant additional densification at dwell temperatures above 1200 °C while below 1100 °C showed densification sans significant grain growth, the dwell time was 300 s. Figure 7 shows the sharpness of transition from densification to grain growth during sintering depending on the dwell temperature. They also investigated the impact of dwell time and temperature on grain growth. 100 MPa of pressure was used at 1000 and 1100 °C with dwell times of 0, 60, 180, 300, 900 and 3600 s. At 1000 °C the grain size remained constant but the relative density increased up to 86.1%. Unlike at 1000 °C the dwell time did affect the grain size at 1100 °C in addition to the relative density with the results being 90.8% and 0.2 μm with 0 s dwell time and 99.8% and 0.5 μm with 3600 s dwell time.

Effectiveness of the PECS method is attributed to plasma which is generated by the pulsing current between powder particles. The plasma eliminates surface impu-

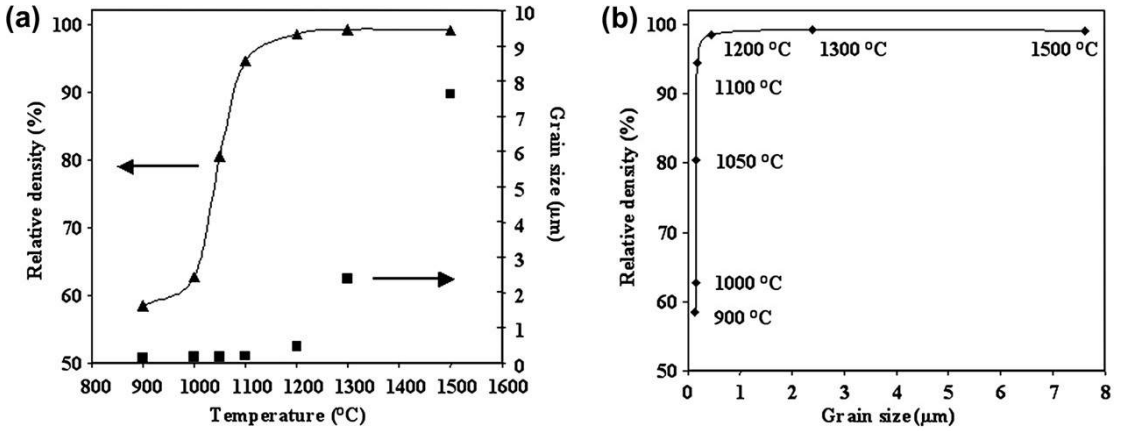

Figure 7: (a) Relative density and grain size shown as a function of temperature and (b) sintering path for 140 nm α -Al_2O_3 powder [29].

rities of the particles and increases neck formation between the particles according to Tokita [31]. However there exists a controversy on the existence of plasma in the process, with articles stating that while the concept is plausible its existence simply hasn't been proven experimentally [20, 32].

An attempt was made to detect plasma during PECS in a study by Hulbert et al. [32] using in situ atomic emission spectroscopy, ultra-fast in situ voltage measurements and direct visual observation. The study was conducted using a variety of powders. The results provided no data confirming presence of plasma.

Generation of plasma in non-conducting samples such as alumina is ruled out by lack of current flowing through the material [18]. Yanagisawa et al. [33] experimented with large spherical copper particles with average diameter of 550 μm and 500 ms single pulse duration under optical microscope. Their results show that sparks formed depending on pressure and current density with higher probability of sparking in cases of low pressure and high current density. Neck growth did not depend on presence of sparks and no difference was measured between necks grown from with or without sparking. Their results indicate that the neck growth is a function of current density.

3.3 State of the Art

Materials PECS has been used to fabricate include metals, ceramics, composites and functionally graded materials. Most of the products have been cylindrical in shape while some researches have had success with more complex shapes.

Jiang et al. [34] demonstrated manufacturing of a complex shaped 20 mm di-

ameter Al_2O_3-ZrO_2-$MgAl_2O_4$ composite using PECS. The strain rate used in the process was approximately 10^{-2}/s at sintering temperature of 1150 °C. The pressure during sintering was 105 MPa and dwell duration was 3 minutes. The resulting composite had a nanocrystalline structure and was fully dense. They estimated the total heating cost for the process as less than 1 kWh, which would make the process commercially attractive. The process was repeated with both pre-consolidated disk and powder with the powder giving the better results. Pictures of the product can be seen in Figure 8.

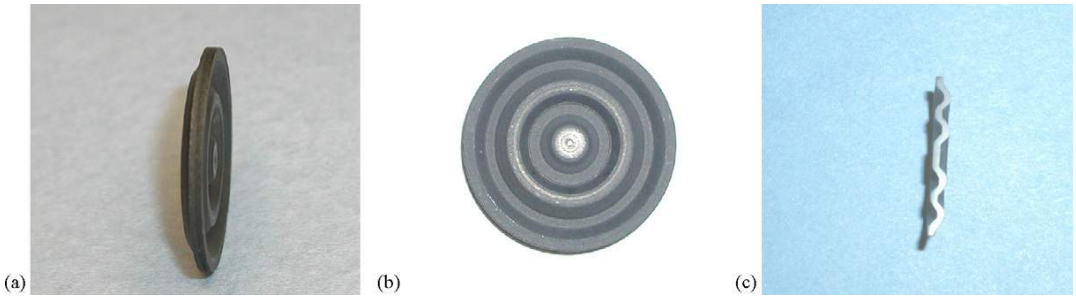

Figure 8: Complex shaped nanocrystalline Al_2O_3-ZrO_2-$MgAl_2O_4$ composite with views from (a) side, (b) top and (c) cross-section [34].

PECS also allows the production of high strength alloys. Sasaki et al. [35] studied microstructures and mechanical properties of bulk nanocrystalline Al-Fe alloys manufactured with mechanical alloying and PECS. Conventionally the strength of wrought aluminium alloys is improved with precipitation hardening with resulting strengths in the range of 600 MPa at the high end. With mechanical alloying duration of 150h they found that α -Al grains were of 26 nm in diameter and dissolved 3.3 of the 5 at.% Fe. The resulting compact had strength above 1000 MPa at ambient temperature with accompanying plastic strain of 15 %, and the strength of 500 MPa at 350 °C. The microstructure of the compact contained α -Al and Al_6Fe with diameter of 90 nm, a small amount of $Al_{13}Fe_4$ and some coarsened 0.5-1 µm α -Al grains. Figure 9 shows the impact of grain size refinement during mechanical alloying on the mechanical properties of compacts.

Functionally graded material composed of three layers with different ratios of Ti and TiB powders was sintered by Wei et al [36]. The used TiB contents were 15, 25 and 35 wt. %. Two different die geometries were used, one cylindrical and one with variable geometry to control the current density, and thus temperature for each layer. SEM micrograph of the cross-section shown in Figure 10 demonstrates the effect of variable geometry in die can have on the product, the results show both decreased porosity and better bonding between layers.

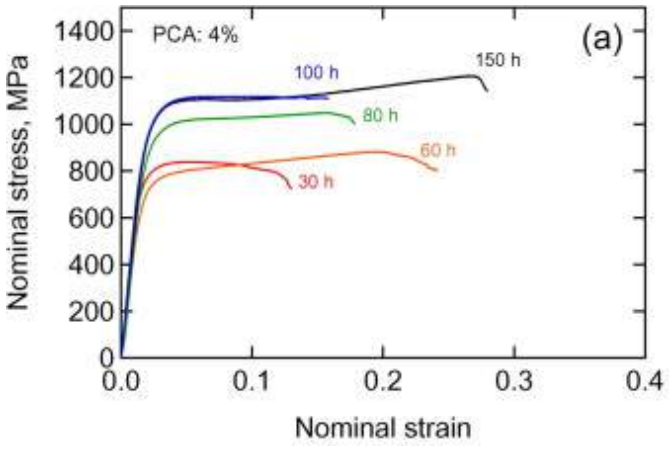

Figure 9: Stress–strain curves of an Al-5Fe alloy sintered using PECS with mechanical alloying durations from 30 to 150 h. [35]

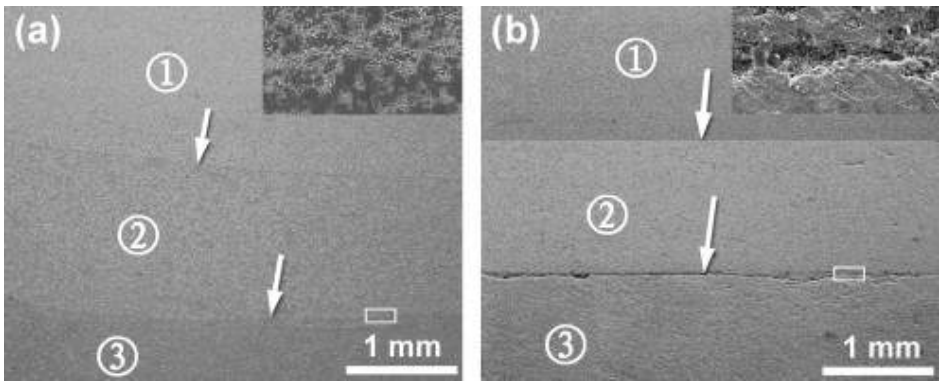

Figure 10: SEM micrographs of FGMs produced by PECS. TiB contents in the layers are (1) 15, (2) 25 and (3) 35 wt. %. Sample (a) was sintered using die with variable geometry while sample (b) was sintered using a cylindrical hollow die. [36]

Conducting graphite/silicon nitride (Si_3N_4) composites were sintered using PECS. Ramirez et al. [37] synthesized the graphene using in situ reduction of graphene oxide during the PECS process. The resulting composites had large electrical conductivity, 100 and 700 S/m for 4 and 7 vol. % of reduced graphene oxide respectively. Other benefits of using a combination of PECS and in situ reduction include grain size refinement of (Si_3N_4 matrix, avoiding of curved graphene sheet and homogenous distribution.

Ultra-high-temperature ceramics (UHTC) such as boron carbides are attractive materials due to their high melting points, refractoriness and hardness. However the properties which make them attractive also traditionally made them hard to

process and sinter [38]. Hulbert et al. [39] sintered boron carbide–aluminum FGM and titanium diboride–boron carbide composites using PECS. The sintering of B_4C was performed using 53 MPa of pressure with maximum temperature of 1660 °C and a 12:2 pulse pattern, after which aluminium was melt infiltrated into the porous compact. The functional grading was achieved by positioning the die off-centre. Figure 11 shows the large gradient in hardness with aluminium infiltration providing a modest increase. The titanium diboride composite was sintered at 1700 °C with pressure reaching up to 100 MPa, up to 5 minute dwell time and 12:2 pulse pattern. Reported densities reached above 99 %. They reported lower hardness results than rule of mixtures would indicate however the fracture toughness was approximate twice that of monolithic boron carbide.

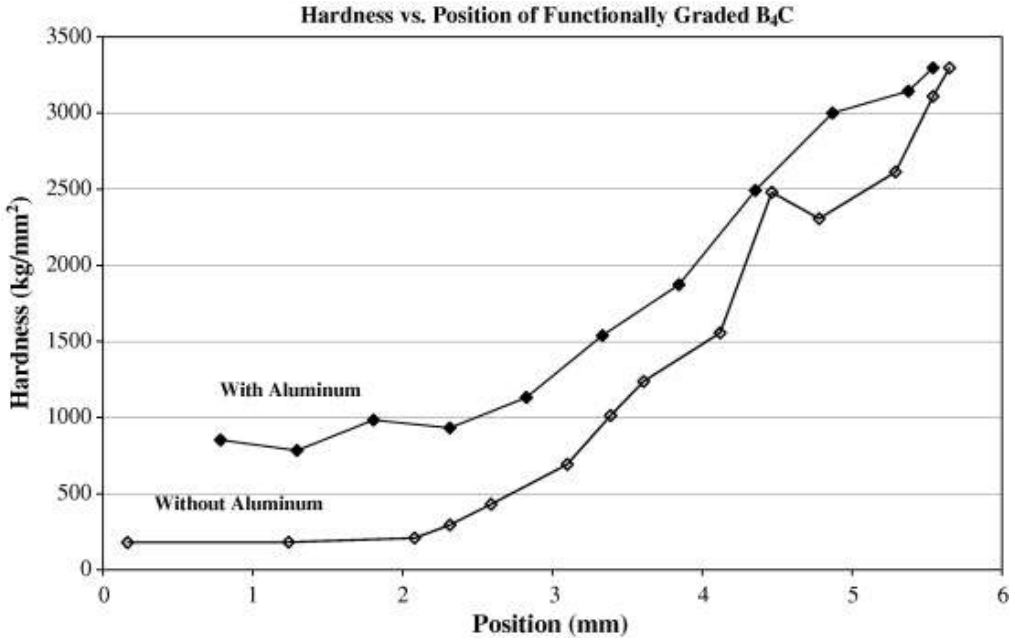

Figure 11: Vickers hardness measurement results (2.5 kgf) of the B_4C-Al cermet FGM with and without aluminium [39].

Cemented carbides such as tungsten carbide (WC) made with metal binders (Co, Fe and Ni) are commonly used in cutting tools. However the metal binders can make the use of these tools undesirable in corrosive conditions. Sintering of pure WC is considered difficult using conventional methods [40]. Omori [41] sintered WC powders with varying cobalt contents (0 to 10 wt. %) using PECS. Sintering of the pure powder required temperature above 1900 °C. Figure 12 shows the increasing fracture toughness as a function of cobalt content indicating significant increase when binder is used.

Transparent ceramics have been produced by PECS. Kim et al. [42] sintered

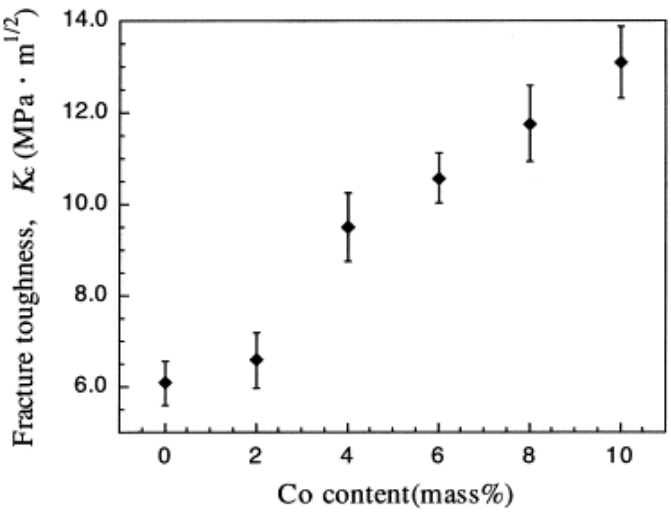

Figure 12: Fracture toughness of WC measured as function of Co content [41].

transparent alumina using low heating rates (8 °C/min) and 80 MPa of pressure at 1150 °C. The resulting compact had average grain size of 0.27 μm and porosity of 0.03 %. They measured the transparency for 640 nm wavelength at 47 % in-line transmission. Figure 13 shows a comparison of alumina sintered at heating rates of 100 and 8 °C/min, indicating large difference in transparency. In-line transmission for the sample sintered at 100 °C/min was measured at 0.2 %. They also reported average grain size approximately doubling with the higher heating rate.

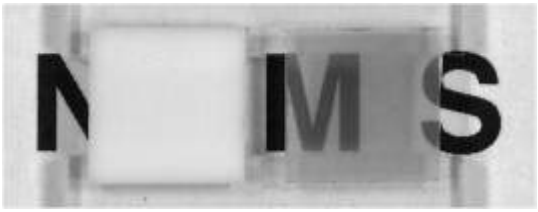

Figure 13: Equally thick alumina samples sintered at 100 and 8 °C/min [42].

PECS has been used to produce compacts with both transparency and magnetic properties, magneto-optical materials can have applications for example in information storage and optical fibre sensors. Mahmed et al. [43] sintered iron oxide–silica core-shell powders. The size of Fe_3O_4 particles inside the amorphous silica shells was smaller than 20 nm. The sintering was performed at 1050 °C, with 30 minute dwell time and 50 MPa of applied pressure. Figure 14 shows compacts with varying Fe_3O_4 contents, indicating that the compacts turn translucent between 0.09 and 0.18 mol %. Transmittance was also measured and reported for wavelengths ranging from UV to visual range, Figure 15 shows a comparison between the samples.

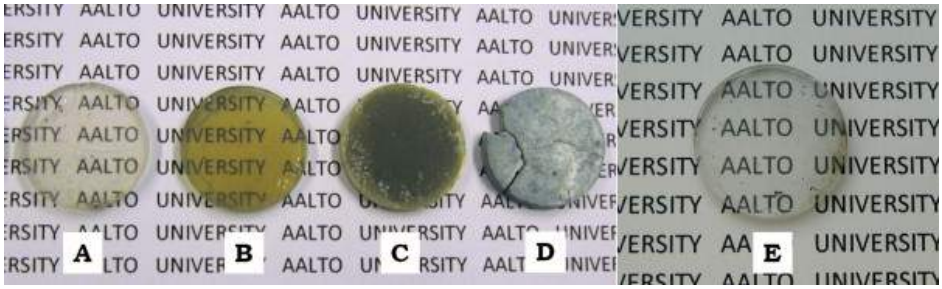

Figure 14: Iron oxide–silica compacts, Fe_3O_4 contents as mol % (a) 0.02, (b) 0.09, (c) 0.18, (d) 0.31 and (e) 0 (reference) [43].

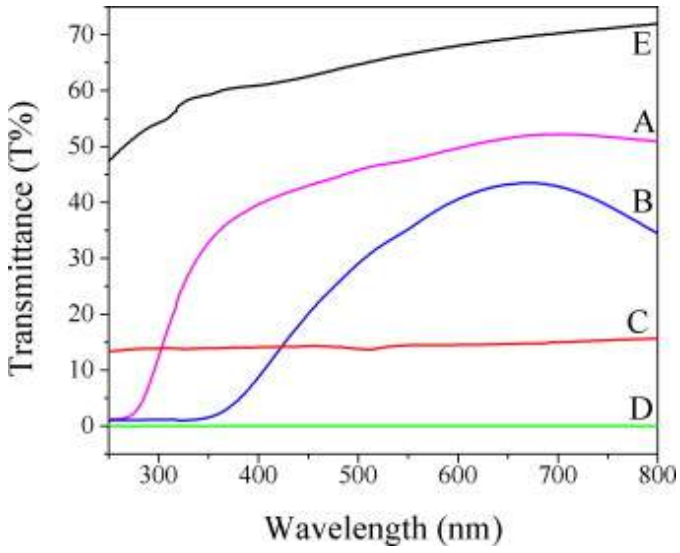

Figure 15: Transmittance of iron oxide–silica compacts, Fe_3O_4 contents as mol % (a) 0.02, (b) 0.09, (c) 0.18, (d) 0.31 and (e) 0 (reference) [43].

4 Numerical Simulation of Pulsed Electric Current Sintering

Simulating PECS requires coupling of multiple phenomena. The phenomena include at least heat transfer and electricity however mechanical stress is sometimes also included. Physics can be added as required by the research increasing the complexity and difficulty of building an accurate simulation. [14] While there are numerous numerical methods that can be used in simulations such as finite difference method, the finite element method is perhaps the most versatile and universally known. FEM can be used to solve numerical problems in complex geometries with a variety of different physics phenomena. [44]

4.1 Finite Element Method

Finite Element Method (FEM) was originally developed for problems associated with structural mechanics and elasticity, however, it was found that FEM could be applied to a much broader set of problems in engineering and physics. FEM is a great mathematical tool for calculating numerical solutions using computers. [44]

In order to fully take advantage of FEM the user needs background knowledge in matrix and vector algebra, numerical methods and partial differential equations in addition to understanding of the physics being modelled. In FEM an object can be described through large number of coordinates called nodes with properties and discretized equations attached to them. The nodes are connected to each other thus creating finite elements. Depending on whether the domain is one, two or three dimensional the inter-element boundaries are the nodes themselves, connecting lines between nodes or planes created by a set of connecting lines respectively. The nodes can have either boundary conditions assigned to them or have varying degrees of freedom. [45]

When a system is described by boundary conditions and equations, the equations can be combined into a solution matrix and calculated using numerical methods such as numerical linear algebra, Euler's method or Runge-Kutta method. The practical application of FEM is sometimes called Finite Element Analysis (FEA), which is usually done by using computer software, which divides the object into a mesh using mesh generation algorithms and contains algorithms for solving the equations numerically. In FEA the mesh density can be adjusted according to the location, thus regions of interest can be calculated to higher detail. [46]

4.2 Literature review of FEM on PECS

Many of the modelling related articles applied FEM on thermal distributions and current densities [30, 36, 47–55], some articles took into account the effects of thermal expansion and pressure in their simulations [30, 36, 51–55] and even fewer combined these with modelling of the densification [30, 52, 53, 55] of the material. Thermal and electrical contact resistances were also handled in variety of different ways, some of the models simply omitted them [47, 53] and others omitted them only at graphite-graphite interfaces [54]. Distinction has been also made between properties of horizontally and vertically placed graphite foil [56]. The heat losses during the process have been also dealt by different approaches as well. Some simply set a convection coefficient on the ends of the graphite electrodes [49], others set the ends of the electrodes to constant temperature [52], while a simplified water cooling circuit was also modelled [54]. Effect of increased furnace temperature on radiated heat was also studied [50].

An investigation into FEM of PECS concentrating on the temperature and current distributions was performed by Anselmi-Tamburini et al. [47]. The materials used in their axisymmetric, time dependent model and experimental validation were alumina and copper. They analysed the measured pulse pattern with Fourier transform and noted that most of the power used in heating is at zero frequency allowing the use of DC in simulation as an approximation. Additionally it was stated that skin effect will not be present due to the small diameter of the die (50 mm) compared to the theoretically calculated skin depth (90 mm). The model was however idealized by assuming no contact resistances because of the pressure applied during sintering. Their modelling results demonstrate the typical difference in current densities when using conducting and non-conducting samples as shown in Figure 16.

Modelling of bulk nanocrystalline tungsten sintered using PECS was considered by McWilliams et al. [48] because of the reduced grain growth compared to conventional sintering techniques. Their model coupled thermal and electrical phenomena, however the model ignored the density evolution of the powder itself and considered tungsten as fully solid. The simulation results show that the punches had the highest temperature which agrees with their highest current density, the temperature maximum could be lowered by shortening the punches without significantly affecting temperature of the sample itself as seen in Figure 17. The shorter punches allowed for lessened power consumption because conductivity of graphite decreases at temperatures above 1200 °C. However when sintering materials in lower temperatures the relationship between power consumption and punch length is reversed

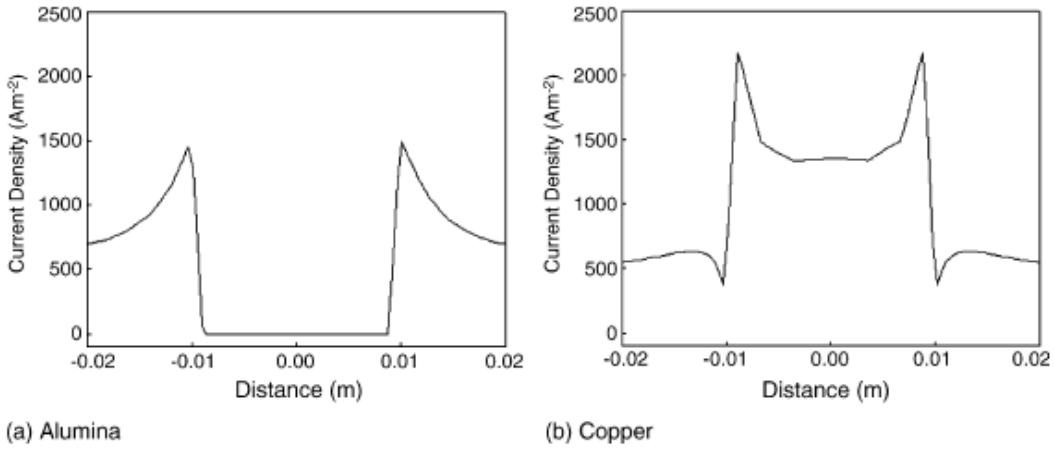

Figure 16: Simulated current densities shown for (a) alumina and (b) copper samples inside graphite dies as functions of radial distance [47].

and higher temperatures in the punches may be desirable as the conductivity of graphite increases with temperature up to 1200 °C. Simulations performed on a 5 mm tall and 25.4 mm diameter sample indicate that when heating the sample to 2000 °C with heating rates of 14 °C and 140 °C the temperature gradient in radial direction increased by 40 °C with the increased heating rate. The thermal gradients could be decreased by increasing the height and/or diameter of the die at a cost of increased power consumption. While using insulation around the die to decrease thermal gradients was also discussed no modelling results on this were presented.

A detailed study of modelling of temperature distribution in PECS was undertaken by Vanmeensel et al. [49]. The results of the model were verified with in-situ electrical and temperature measurements [56]. Contact resistances in the system were found by comparing results from different geometries by increasing complexity, they also determined electrical and thermal conductivities of graphite foil and integrated the contact resistances into those. The research also compared conductive (TiN) and non-conductive (ZrO_2) fully dense samples in addition to an all graphite (FE 779) contact free monoblock body with the results being similar to those reported by Anselmi-Tamburini et al. in Figure 16. The findings indicated that the temperature gradient in the radial direction in the compact depended on the electrical conductivity of the material and the gradient was bigger when TiN was used in comparison to ZrO_2 as seen in Figure 18. The electrically insulating properties of ZrO_2 forced the current to flow around the sample increasing the Joule heating in the die leading to more homogeneous temperature inside the sample. Additionally

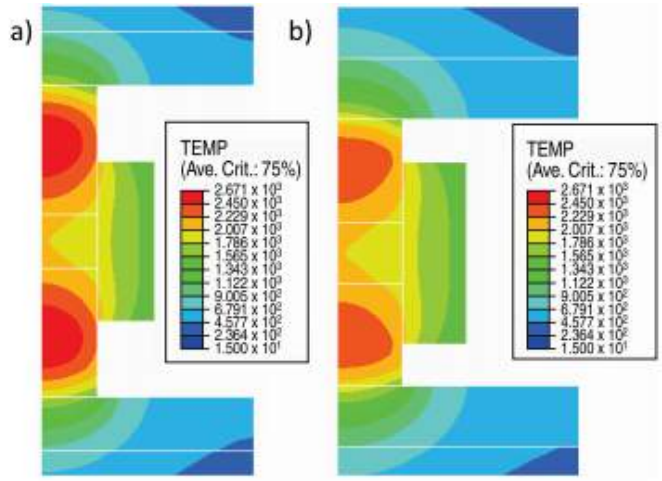

Figure 17: Use of (a) longer punches produces higher maximum temperature compared to (b) shorter punches with little effect in the simulated temperatures inside the samples [48].

they determined the convection coefficient of the system experimentally using the experimentally measured cooling curve of the graphite dummy, with the resulting coefficient being 880 W/(m °C).

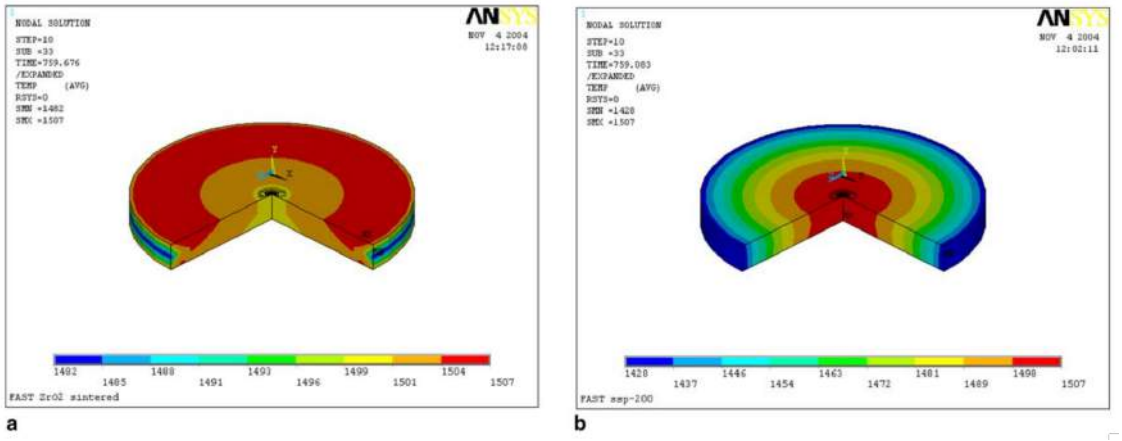

Figure 18: Simulated comparison of thermal gradients when sintering (a) non-conductive (ZrO_2) and (b) conductive (TiN) samples [49].

Unlike most models of PECS, Pavia et al. [50] also took into account the increased chamber temperature during prolonged sintering and compared it to results obtained with a model using ambient temperature for the chamber. They measured and modelled current, voltage and temperature for systems with no sample, a pre-compacted alumina sample and a pre-compacted manganese sample respectively which had diameters of 36 mm and thickness's of 6 mm. The samples were

heated at the rate of 100 °C/min until the temperature reached 900 °C as monitored by thermocouple inserted into the die at the same height as the centre of the sample. After which the sample was held at the temperature for 5 minutes. The pressure applied during sintering was 100 MPa to minimize contact resistances in the system allowing them to ignore them in their model. In the case of the model with static chamber temperature there was a decrease in the sample temperature during the dwell period when compared to experimental measurements. However when experimentally measured chamber temperature was added to the model they found that the decrease disappeared indicating that the chamber temperature did have a marked effect on the simulation by decreasing heat loss through radiation. A comparison between temperatures measured experimentally and calculated the different models is shown in Figure 19.

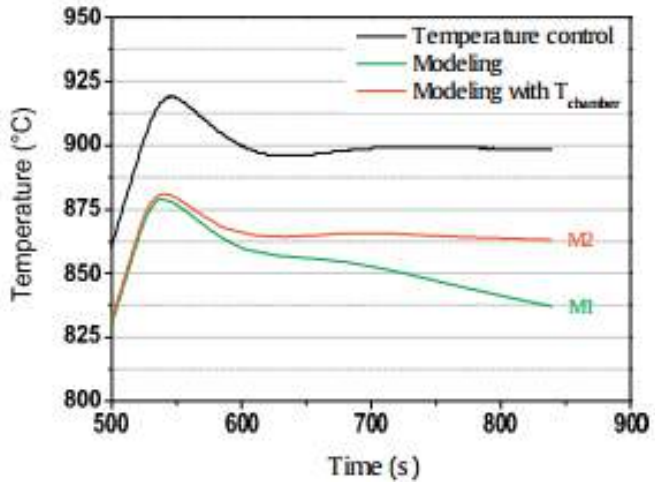

Figure 19: Comparison of (black) experimentally measured, simulated with (green) constant chamber temperature and with (red) correct chamber temperature temperature profiles [50].

Wei et al. [36] studied the temperature and stress distributions of Ti and TiB functionally graded materials during PECS using simulations and experimental validation. FMGs are composites, where their structure and composition are varied according to position. Their model coupled electrical, mechanical and thermal phenomena. The study also took into account the contact resistances at interfaces, but neglected the thermal radiation due to usage of graphite felt that surrounded the die. The sample consisted of 5 layers of Ti-TiB with Ti content of 45, 55, 65, 75 and 85 wt.%. In the model the samples were subjected to compressive pressure of 89 MPa while the heating rate was 180 °C/min and the heating was ended when the temperature reached 1127 °C at the surface of the die on the level of the centre

of the sample. Due to how Joule heating works the temperature increases with the current density and current density decreases when the area of the dies cross-section increases. Therefore by changing the die radius as a function of position in the axial direction the temperature profile can be controlled for materials with different properties, the die set-up is shown in Figure 20. The simulations gave the largest temperature gradient of 90 °C from top to bottom of the lateral surface of the sample during dwell time, while the gradient in radial direction inside the sample didn't exceed 14 °C. When the heating rate was decreased to 100 °C/min the temperature gradient on the lateral surface decreased to 54 °C. In stress simulation they found that the maximum stress and stress gradients in the sintered body were found at the end of the heating process and both increased with heating rate, the maximum stress with 180 °C/min heating rate was 115 MPa and the gradient 35 MPa. For validation of their simulation Wei et al. performed sintering experiment using 1127 °C as the sintering temperature, 50 MPa applied pressure and 180 °C/min heating rate. The experimental validation produced results similar to their simulation. The simulation and experiments showed that the temperature distribution in the sample can be managed by varying the die geometry according to material, while the stress distribution indicated an increased possibility of inhomogeneity of microstructure and cracks. By decreasing the heating rate the stress and temperature gradients could be decreased. Figure 10 has a comparison of microstructures obtained from samples sintered with and without a die with variable geometry.

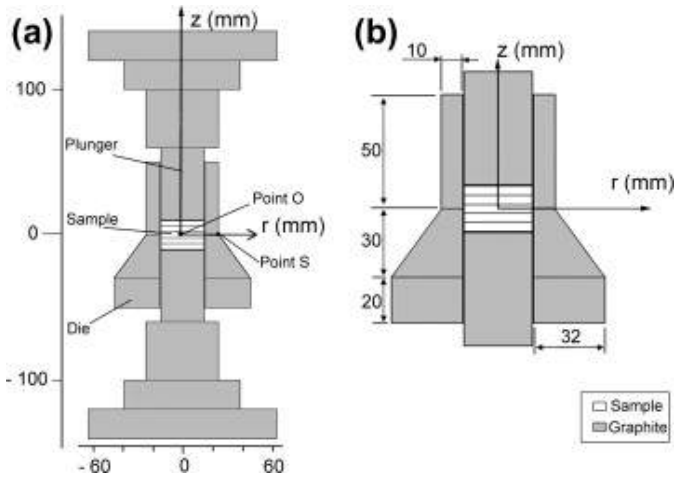

Figure 20: (a) Schematic of the parts and (b) dimensions of the die using variable geometry [36].

Simulations on electrical, temperature and stress fields for PECS of alumina were

conducted by Allen and Walter [51]. Their model is simplified by the usage of solid alumina as the sample instead of powder. The simulation includes the use of a proportional integral derivative (PID) controlled that is used to control the heating rate through voltage adjustment. Specifically their model includes Joule heating, thermal convection, thermal conduction, thermal radiation, mechanical stress and both thermal and electrical contact resistances. The practical experiments were temperature controlled using a pyrometer located in the upper punch, the sample was heated in stages to temperatures 400, 1000 and 1500 °C with dwell times applied after each heating stage, afterwards the cooling was also controlled for down to 1000 °C after which the power was shut down. The applied force was also varied according to time from 5 to 31 kN. The model showed that the temperature gradient inside the sample in the radial direction was highest during the dwell period, approximately 160 °C at maximum. Simulated thermal gradients of the alumina sample are shown in Figure 21. The large temperature gradient was partially explained by the comparably low thermal conductivity of alumina. Simulation of stress distribution during dwell time at the same locations found a gradient of 35 MPa with the compressive stress being highest at the centre of the sample, resulting in possible inhomogeneity in the final microstructure. While their model demonstrated significant temperature and stress gradients in the sample, no suggestions were made on how to mitigate them.

Temperature, current and strain distributions during PECS were modelled and simulated by Cincotti et al. [54]. The work only considered an already dense graphite compact thus making it best applicable to the latter stages of the sintering process. In building of the model they increased the complexity of the axisymmetric model one step at a time by adding different physics, interfaces or materials such as graphite foil at each step. The contact resistances taken into account in the model were between the stainless steel electrodes and the graphite parts as the graphite-graphite contact resistances were considered negligible due to the pressure applied during the process. Due to the lack of axisymmetry in the cooling circuit inside the metal electrodes, they used a simplified geometry but assumed heat transfer to be the same. They also used a typical convection coefficient value from literature instead of measuring it. In the model they also used magnetic induction in their calculations, which required the use of a modified version of Maxwell's equation. They developed a Fourier series to match the experimentally measured voltage and current readings for modelling purposes, and the results were in a good agreement. The model assumed no friction between interfaces and considered the metallic electrodes as elastic elements subject to pressure and temperature changes in addition

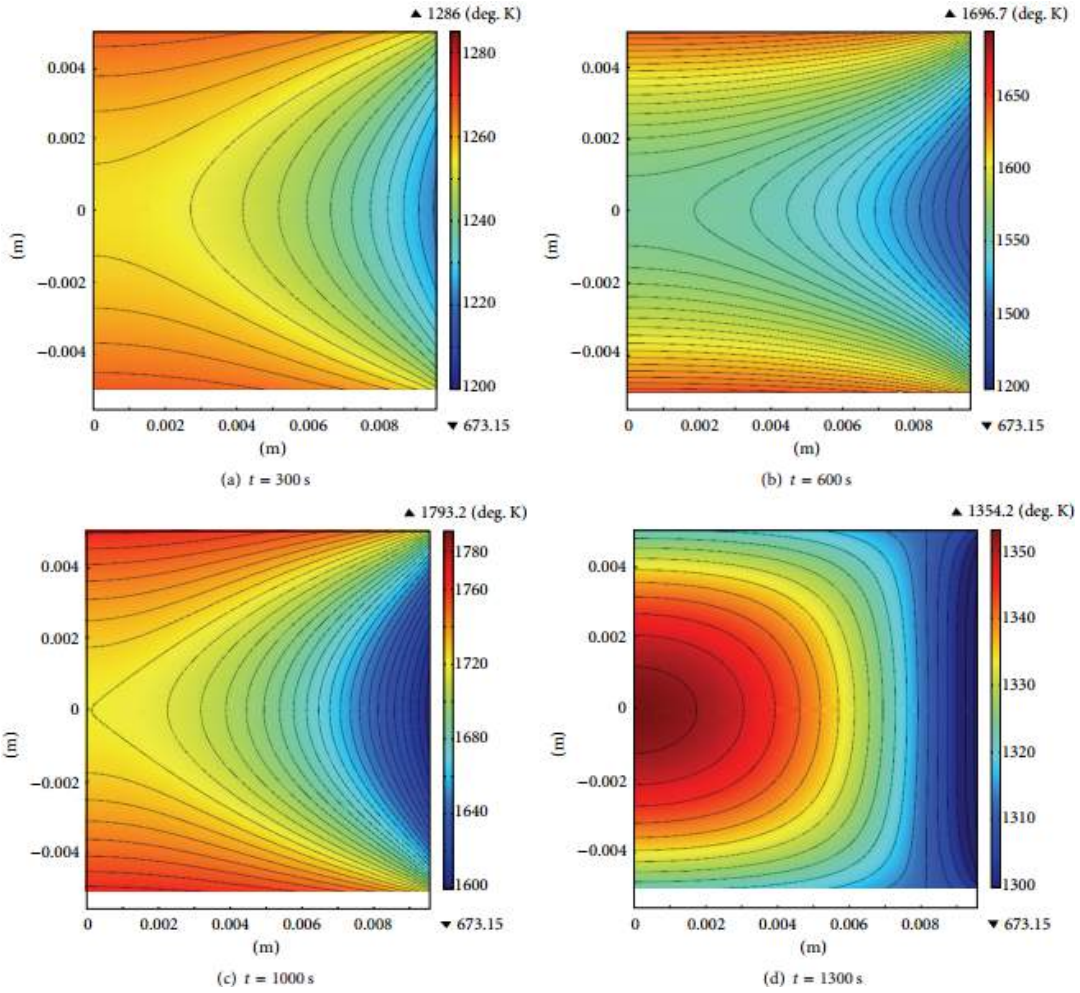

Figure 21: Simulated temperature profiles of alumina samples during PECS at various stages of heating, and in the midst of cooling [51].

to the graphite parts. The modelling and experimental work showed that the inductance depends heavily on the cross sectional area of the sample, being negligible when the cross sectional area is small and increasing with its size. Validation of the model was performed by running experiments with different parameters and geometry rather than using the same model used during development stage. The validation procedure showed that the simulated temperature, voltage and displacement produced results that matched well with the experimental, however there was both temperature overshoot and undershoot depending on the used current.

An effort to develop a fully coupled thermal–electric–sintering model which takes into account densification of the powder was taken on by McWilliams and Zavaliangos [57]. The modelling was done by developing and coupling two models simplified 2D-models, first thermal–electric model calculated the thermal profile which was

then used by the thermal-displacement model to simulate densification. To form a complete the iteration loop the thermal-displacement simulation was then used to update the mesh used in the thermal–electric model. The results indicate that during sintering of electrically conductive powders low density areas of the powder can densify faster than the high density areas due to the increased Joule heat generation caused by higher resistivity. However the model does not take into account the entire PECS process and only simulates density evolution of the powders disregarding external pressure and heat transfer from and to the surroundings of the sample.

Stress and temperature distributions were studied by Wang et al. [52] using both FEM and experiments to validate the simulation results. Their PID controlled time dependent model coupled thermal, electrical and mechanical phenomena and integrated powder densification by using moving mesh technique. The convective cooling was simplified by assuming the graphite surfaces in contact with the electrodes were at constant 27 °C. The study was conducted on alumina using different sample sizes (diameter 12, 20 36 and 50 mm and height 4 mm), heating rates (50, 100 and 200 °C/min), applied pressures (50 and 100 MPa with the maximum temperature measured at the die surface being 1300 °C). The densification was modelled by treating the alumina powder as an isotropic solid with properties that evolved during the sintering process. According to the simulation results heating rate of 50 °C/min was desirable for achieving smaller thermal gradients for samples up to 36 mm, with the 50 mm diameter sample having smallest thermal gradient with heating rate of 200 °C/min as shown in Figure 22. The models also showed that the temperature gradient didn't increase with die size with the highest gradient found during heating of the 20 mm diameter samples. While increasing the applied pressure didn't have a significant effect during dwell period it did have an effect during heating by decreasing the temperature gradients slightly. In experimental analysis the coarser microstructure in the centre of the samples agreed with the temperature profile given by the model of the sample during the process. Their validation also found coarser microstructure in the larger samples contrary to their expectation, increased radial and angular stresses were offered as a possible explanation for this increased grain growth.

Wolff et al. [53] proposed an improved model for simulating densification of porous materials for PECS process using lead. The physics coupling used in the study was an improvement on one developed by McWilliams and Zavanglios [57] presented earlier in the chapter. The improved coupling took into account the heat generated by plastic deformation and the mechanics of porous materials while ne-

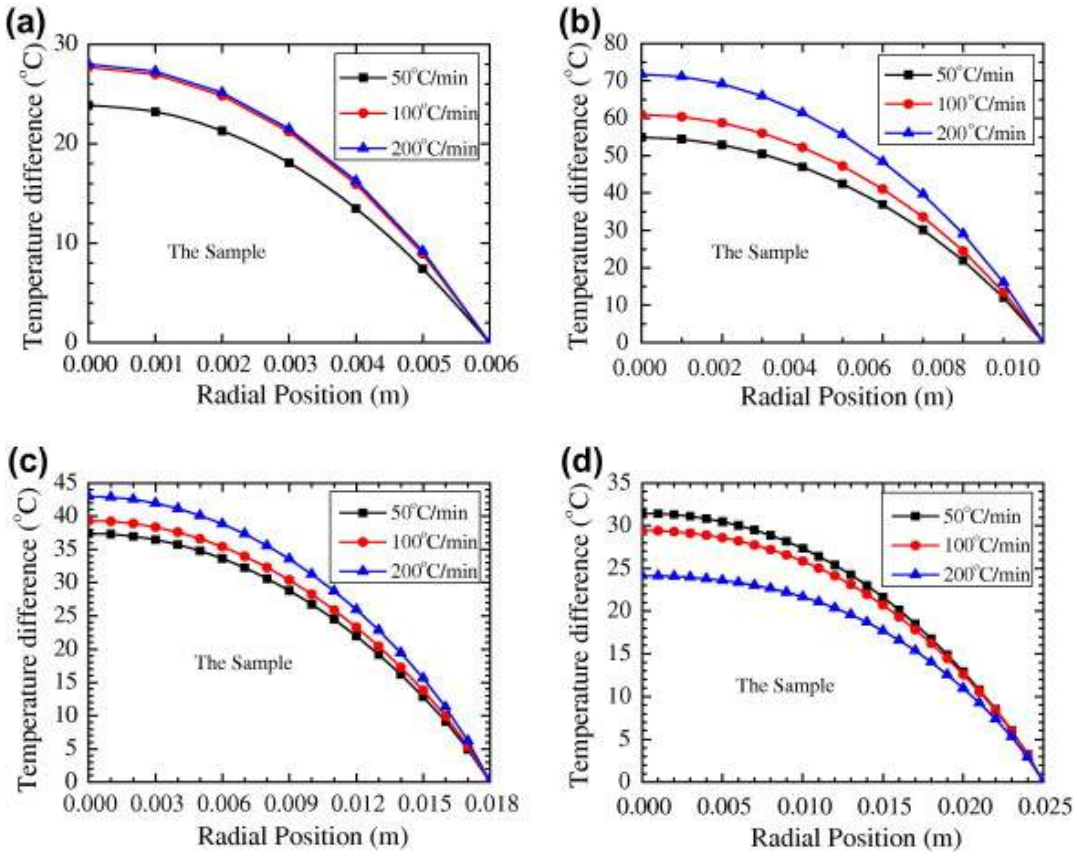

Figure 22: Temperature gradients from centres of samples to their radial surfacs. Simulations were performed for (a) 12, (b) 20, (c) 36, and (d) 200 °C/min.[52]

glecting the presence of thermal or electrical contact resistances. The simulated sample was 100 mm in diameter, 20 mm in thickness and had a starting relative density of 0.7, the simulated pressure was 2.825 MPa. In simulation with 100 mm diameter sample with 20 mm of packed powder with starting relative density of 0.7 under 2.825 MPa of axial stress the temperature gradient in radial direction reached 50 °C when the temperature at the centre of the sample reached the sintering temperature of 150 °C. There was no noticeable difference in simulated axial pressures when the centre of the sample reached 150 °C, however there was a difference in them during heating process which in combination with the temperature gradient caused non uniform density in the compact with the centre having relative density of 0.88 and the lateral surface of 0.82 as shown in Figure 23.

An investigation on the scalability of PECS was conducted by Olevsky et al. [55] using FEM simulations. Their model combined thermal, electrical and mechanical phenomena with four different sizes of tooling. Their model also included powder consolidation allowing for simulation of porosity, shrinkage and grain growth de-

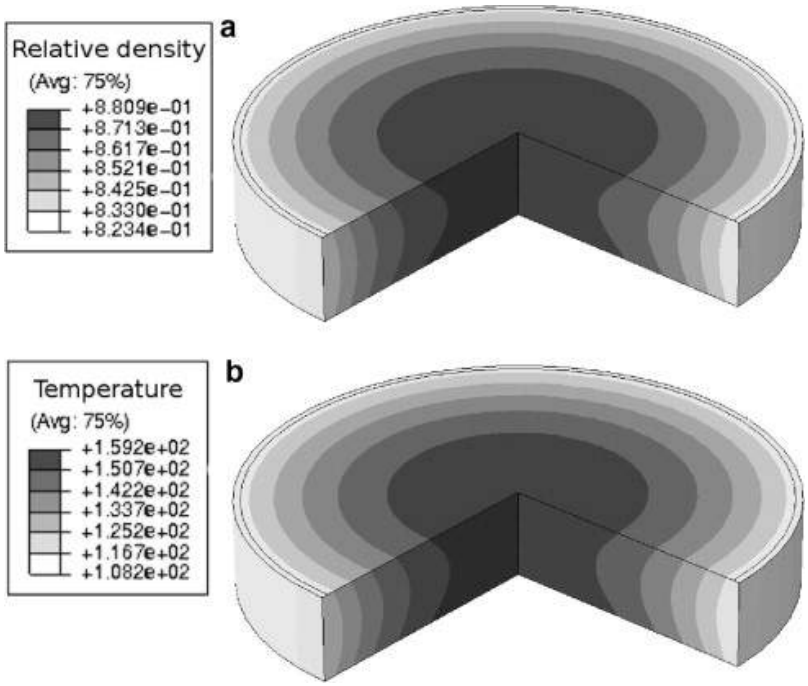

Figure 23: Simulated (a) density and (b) temperature gradients in lead at the end of PECS cycle [53].

pending on location. The alumina sample diameters were 15, 40, 48 and 56 mm and heights 3, 7.9, 9.5 and 11.1 mm accordingly. The experimental data corresponded well to the simulation results for larger geometries with some deviation depending on heating rates. However when smaller geometries were simulated the temperature overshooting was significant for period of 200 s regardless of the used heating rate. The results indicated that as the tooling dimensions increase so do the temperature and pressure gradients from the centre of the sample to the outer surfaces. The gradients are also magnified by increased heating rates and decreased by lower heating rates. They also noted that when the samples experienced significant densification early in the process the decreased porosity didn't inhibit as much grain growth leading to coarsened microstructure. Figure 24 shows a comparison of evolutions in temperature and relative density at the centre of the modelled 56 and 15 mm diameter samples. Based on the results lower heating rates were desirable for homogeneity in microstructure and that the model used is good for qualitative estimates.

A PECS model based on continuum theory of sintering has been developed. It is used to understand how the porous body evolves during the sintering process. The mass flux mechanisms used in the model that contribute to densification are grain-boundary diffusion and dislocation creep. The grains themselves are modelled

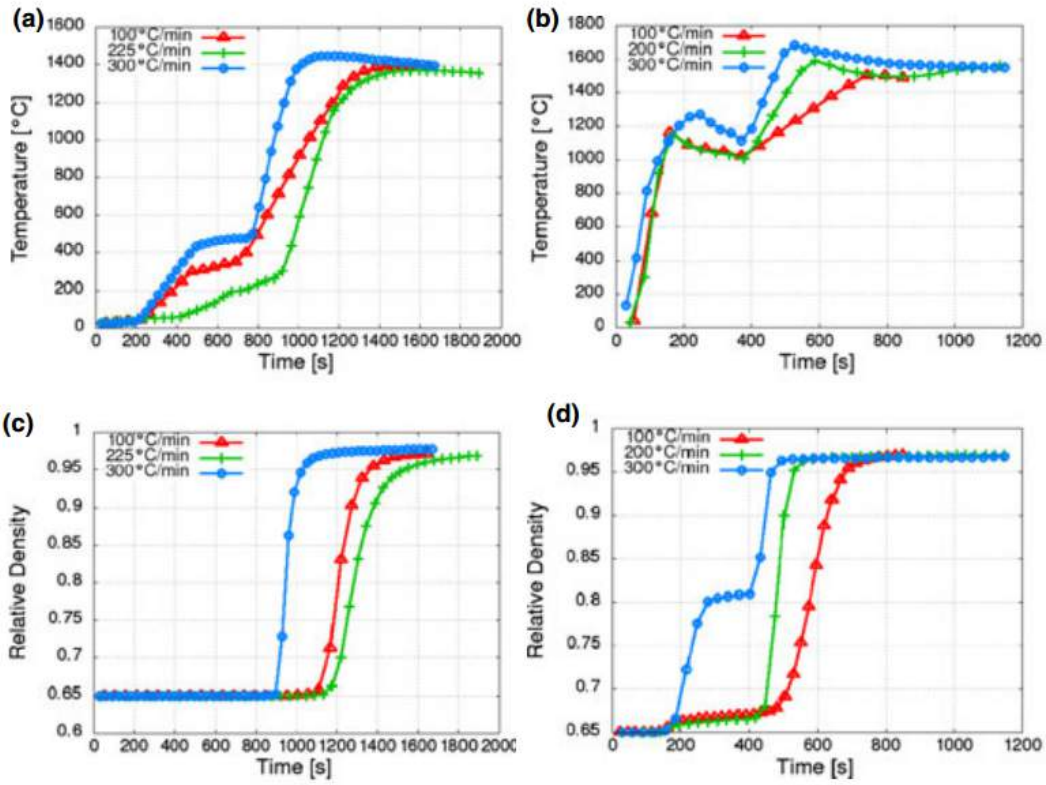

Figure 24: Evolutions of temperature and relative density for (a,c) 56 and (b,d) 15 mm diameter samples [55].

as tightly packed rectangles with elliptical pores existing in their corners. The model indicated that high heating rates and short holding times would give the smallest grain size, the pore tip sharpness increases at higher temperatures with higher heating rates contributing thus the densification peak is shifted to higher temperature. Experimental results presented chapter 3.2 seem to confirm the viability of their model. [30]

5 Experimental Procedures

This chapter introduces the procedures used in following experiments. Thermal and electrical conductivity of ISO-63 graphite were determined, as was the electrical conductivity of graphite foil. Measurements were carried out during PECS experiments that utilized the graphite products to both determine and validate their properties used in modelling. Solid α-alumina and copper samples were investigated for their behaviour during PECS. Densification data from PECS of copper powder was acquired for building a master sintering curve. Complex shaped compacts were sintered out of WC-12Co powder. PECS experiments were performed using FCT HP D25-2 furnace shown in Figure 25.

Figure 25: FCT HP D25-2 PECS furnace installed at Aalto University.

5.1 Determination of thermal and electrical properties

5.1.1 Thermal Conductivity of ISO-63 Grade Graphite

Thermal conductivities of materials are temperature dependent, however the information on materials properties provided by the ISO-63 graphite supplier only included materials properties for ambient temperature [58]. The properties are shown in Table 1.

Table 1: Materials properties of ISO-63 graphite at ambient temperature as given by the supplier. [58]

ISO-63 Graphite	
Density	1840 kg/m^3
Resistivity	1650 $\mu\Omega$cm
CTE	5.5×10^{-6}/K
Thermal conductivity	70 W/mK
Modulus of Elasticity	14 GPa
Flexural strength	76 MPa
Compressive strength	180 MPa
Tensile strength	53 MPa

Thermal conductivity can be calculated from thermal diffusivity of the material when its specific heat is also known. Laser Flash measurement (Anter FlasLine 5000™) was used in determining the thermal diffusivity for the ISO-63 graphite. The experiment was conducted in temperatures of 100, 300, 500, 700, and 900 °C. Values for specific heats vary little between different graphite varieties, thus it was decided to use values from literature for POCO graphite [59].

In a laser flash measurement one side of the sample is subjected to a laser pulse, the effect of which is measured on the opposing side of the sample as function of time. The thermal diffusivity is calculated from the results using the following equation [56],

$$\alpha = 0.1388\frac{L^2}{t_{0.5}} \tag{1}$$

Where L denotes thickness of the sample and $t_{0.5}$ the time required for the sample to heat up to 50 % of its maximum temperature. Using results from equation 1 the thermal conductivity can be calculated with equation 2,

$$k = \rho c_p/\alpha \tag{2}$$

where ρ is the density, c_p is the specific heat and α is the thermal diffusivity. Schematic of equipment used in the Laser Flash measurements is shown in Figure 26 [56].

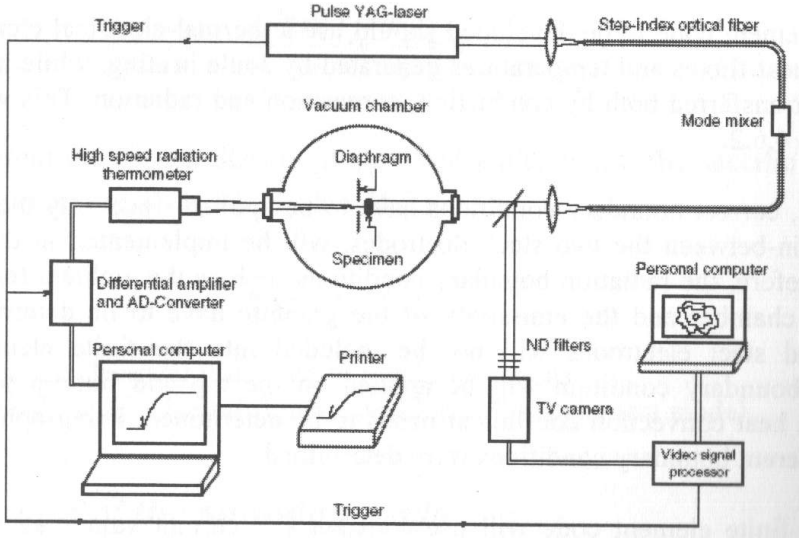

Figure 26: Schematic of Laser Flash measurement equipment [56].

5.1.2 Electrical Properties of ISO-63 Grade Graphite

Electrical properties of ISO-63 graphite were determined by performing temperature controlled PECS experiments using a solid graphite rod with a diameter of 25 mm and length of 155 mm. Temperature was measured and controlled by a thermocouple. The compressive force exerted by the electrodes was set to 6 kN equalling to 12.2 MPa in this and every experiment where the smallest diameter of the graphite parts was 25 mm unless otherwise noted. The graphite rod was heated to 200 °C, after the temperature had stabilized the difference in voltage was measured from two points which were located at 20 mm distance above and below the centre of the sample by using molybdenum wires inserted into the sample and connected to an oscilloscope (Fluke 120 Series ScopeMeter). Figure 27 shows the placement of the thermocouple and voltage measurement points. The potential measurement was repeated every 100 °C until 900 °C was reached. The maximum temperature of 975 °C for the measurements was set by thermal limitations of the thermocouple. Heating rate used during the experiment was 50 °C/min, the same used in every experiment unless otherwise noted. The PECS furnace offers current measurement by the way of an integrated measurement system that uses Hall effect to calculate the RMS current during the process, continuous 1 ms pulsed current was used in all experiments. Thus the current was determined from the process log file for the stabilized temperatures.

Resistance of the graphite rod is calculated by the formula given in equation 3,

$$R = V_{RMS}/I_{RMS} \tag{3}$$

where the RMS voltage V_{RMS} is given by the ScopeMeter output and the RMS current I_{RMS} is given by the FCT HP D25-2 process log. The resistivity ρ is calculated according to the formula shown in equation 4, where A is the cross sectional area of the rod and l the distance between the measurement points in axial direction. Using the calculated resistivity conductivity of the graphite can be obtained from equation 5.

$$\rho = R \times (A/l) \tag{4}$$

$$\sigma = 1/\rho \tag{5}$$

5.1.3 Conductivity of Graphite Foil and Contact Resistances

The electrical conductivity of graphite foil was determined as a function of temperature by placing one layer of foil between two 77.5 mm tall 25 mm diameter graphite rods and repeating the voltage measurements as described in chapter 5.1.2. Using the difference between the measured voltages the conductivity of graphite foil was calculated using equations 3, 4 and 5.

Finding the conductivity of vertically placed graphite foil was done by measuring voltage differences between locations on the punch and die shown in Figure 31 in temperatures corresponding to other voltage measurement experiments. The conductivity was then determined using modelling. Voltages were also measured across graphite–graphite -interfaces on both geometries to determine the magnitude of electrical contact resistances on these interfaces.

5.1.4 Graphite Felt

Graphite felt is often used as thermal insulation in PECS. Effect of graphite felt use wrapped around the die was measured. Figure 30 shows the locations where temperature and voltage measurements were taken. The locations 30 mm above and below the centre were used for voltage measurements with the rest used for temperature measurements. The experimentally recorded temperature, voltage and current data

were compared to simulated results for the same geometry using materials properties supplied by the manufacturer to validate their use in the model.

5.1.5 Presence of Volatiles in Graphite

The presence of volatiles in the supplied graphite was determined using the setup shown in figure 31. Unused graphite parts were heated in the PECS furnace using heating rate of 50 °C/min to 975 °C in 100 °C steps from 500 °C, with the temperature being stabilized between each step. The PECS furnace heats the system using high current until it reaches 450 °C, where the pyrometer controlled heating takes over, this applies to all pyrometer controlled experiments.

Voltage measurements were taken from the punch and the die for each stabilized temperature. The experiment was repeated three times using the same graphite parts and measured voltages were compared. A decrease in measured voltage from experiment to experiment would indicate presence of volatiles. A stable voltage across the experiments would indicate that no volatiles were removed during the experiments.

5.2 Determining Modelling Parameters

5.2.1 Convective Cooling

Convective cooling coefficients for the PECS processes were determined by fitting simulated results to experimentally measured temperatures from multiple points. Temperatures were measured from the 25 mm graphite rod and the graphite monoblock. Figures 27 and 29 correspond to the experimental setup, the temperatures were measured in the marked locations near the top and bottom of the parts as well as near the centre. In the case of monoblock the temperature measured near the centre used a pyrometer instead of thermocouple.

The temperature profiles were measured between temperatures of 200 and 900 °C with 100 °C intervals and at 975 °C. The temperature profiles were also measured during cooling phase as a function of time. Both ways of measuring the temperature profile were used in determining the convective cooling coefficient.

5.2.2 Comparison of Pyrometer and Thermocouple

A comparison between results given by the pyrometer and thermocouple was performed. The thermocouples used in the measurements could be used up to maximum temperature of 1000 °C, while the pyrometer provided results from 450 °C upwards.

A 25 mm graphite rod with pyrometer holes drilled in both ends as seen in Figure 28 was used to determine the difference between the measured temperatures. The figure shows locations for both the pyrometer measurement surface and the thermocouple measurement point.

5.2.3 Validation Using Fully Dense α-alumina and Copper

Samples of α-alumina and copper were heated using pyrometer control to maximum temperatures of 975 and 850 °C respectively. During the heating process temperature and voltage measurements were taken at stabilised temperatures every 100 °C starting from 500 °C with the maximum temperatures also included in the measurements. Both samples had diameter of 25 mm, however the heights were different. Height of the α-alumina sample was 4,8 mm while the height of the copper sample was 2,65 mm. Figure 32 shows locations for temperature and voltage measurements, voltage was measured from the punches, while temperature was measured using the pyrometer and thermocouples. Temperature, voltage and current data was recorded for validation of the model.

5.3 Sintering Experiments

5.3.1 Densification of Copper

Copper powder (< 75 μm, > 99 % purity, Sigma Aldrich) was sintered into three different 25 mm diameter compacts and a single 80 mm diameter compact. Compressive forces used in the processes were 12 kN for the 25 mm compacts and 122 kN for the 80 mm compact.

The 25 mm compacts were sintered using heating rates of 50, 75 and 100 °C/min. The sintering temperature was 650 °C and dwell time was 5 minutes. Schematic shown in Figure 32 corresponds to the experimental set-up with the sample changed to copper powder. The sintering processes were controlled using thermocouple temperature measurements taken from the die as shown in the figure. The amount of copper powder sintered was 22 g for each compact. Thickness of the copper was measured before and after sintering by measuring the distance between the opposing ends of the punches and calculating the difference.

The 80 mm diameter copper compact was sintered with heating rate of 50 °C/min controlled by thermocouple temperature measured from die up to 450 °C after which the process was controlled by pyrometer to the sintering temperature of 600 °C where a dwell time of 5 minutes was applied. 150 g of copper powder was used for the

compact. Figure 33 displays schematic of the parts used in the process as well as the points used in temperature measurements.

5.3.2 Complex Geometries

Two compacts with different complex geometries were sintered. Figure 34 shows schematics for the 36 mm diameter geometries. The material used in compactions was 68 g of WC-12Co powder (planetary milled 2h and 4h, ZCCC/S-80 0,2/0,8 μm). The compressive force used in the compactions was 50 kN. The processes were controlled by temperature measured by pyrometer and a degassing holds were applied at 525 °C for 90 s. Heating rate of 100 °C/min was used to reach the sintering temperature of 1180 °C where a three minute dwell time was used.

5.4 Materials Characterisation

5.4.1 Sample preparation

The surfaces of the 25 mm diameter copper compacts and cut samples from the 80 mm diameter copper compact were ground with SiC paper down to P1200 for density measurements. The WC-12Co compacts were only partially ground due to their geometry preventing it. Pictures of the samples are shown in Figures 59 and 61.

Cross-sections of WC-12Co samples were cut, mounted in epoxy and ground with SiC-papers up to P1200 after which they were polished using diamond paste (6, 3 and 1 μm). The samples were then subjected to a final polishing step by colloidal silica (0,6 μm). The samples were etched using the Murakami etchant and sputtered with gold for scanning electron microscope (SEM) use. For hardness tests the samples were polished again using diamond paste. The copper powder studied in SEM was placed on a double sided carbon tape attached to the SEM sample holder.

5.4.2 Density Measurements

Densities of the compacts were measured using Archimedes' method. The samples were weighed using Sartorious Analytical Balance CPA224S. Following equation was used to calculate the densities from the measured results,

$$D = \frac{m_a D_l}{m_l - m_a} \tag{6}$$

where m_a is the weight of the compact in air, m_l in liquid, and D_l the density of the liquid. Relative densities of the compacts were calculated by dividing the result with the maximum density of the material.

5.4.3 Hardness Measurements

Hardness measurements for the WC-12Co compacts were performed using Innovatest Nexus 4303 Vickers hardness tester. The measurements were done using 4kgf force across the cross sections

5.4.4 Scanning Electron Microscopy

Morphology of the copper powder and microstructures of the WC-12Co compacts were studied using SEM. The characterisation was done using Hitachi S-4700 field emission scanning electron microscope (FE-SEM).

6 Model Development

Finite element modelling of PECS was performed using Comsol Multiphysics software. In order to perform a simulation the software requires a geometry, all geometries simulated in this thesis are axially symmetrical allowing for simplified 2D drawings to be converted by the software into accurate 3D forms. Further input data and boundary conditions need to be determined in relation to the geometry, amongst others the properties of the materials being simulated and electrical current used belong to this group. Next the physics are selected, the software is delivered with multiple different physics packages aimed at simulating different scenarios. Every simulation in this thesis uses one of the following packages; heat transfer in solids, Joule heating, or Joule heating and thermal expansion.

The first models were built and simulations performed to either confirm experimentally measured results or materials properties found in literature. Next a new model was built using the selected properties and compared to new experimental results measured using a different geometry to validate the accuracy of the model. Modelling the sintering behaviour of powders under PECS was outside the scope of this thesis due to the complexity of the problem, however densification of copper powder was modelled using the master sintering curve method. Finally sintering of compacts with complex geometries from WC-12Co powder was simulated.

6.1 Physics in the Models

Joule heating, sometimes called ohmic heating or resistive heating is a process where current passing through a conductor generates heat. Because the amount of heat generated is relative to current squared an effective joule heating system will use high currents and low voltages, as is the case with PECS, in cases where it is desirable to avoid as much load loss as possible such as electrical networks high voltage combined with low current is used.

In the case of direct current the formula for Joule heating is

$$P = IV, \tag{7}$$

where P equals the amount of electrical energy converted to thermal energy, I is the current travelling through the conductor and V is the amount that the voltage drops across the conductor.

In case of alternating current and pulsed current the formula for instantaneous power is

$$P(t) = I(t)V(t), \tag{8}$$

however in this work average power is more practical to use, as the physics used in the models will produce the same results in either case.

$$P_{avg} = I_{RMS} \times V_{RMS}, \tag{9}$$

It is assumed that the resistor is ideal and there is no need to take reactance into account. The equation 9 can also be written into form

$$Q_j = I_{rms}^2 \times R. \tag{10}$$

Heat is also transported by thermal conduction

$$Q_{cond} = kA\frac{dT}{dx} \tag{11}$$

where k is the thermal conductivity of the material, A is the area normal, and dT is the thermal gradient to direction x.

Heat is also lost by radiation, to simplify the problem of simulating the entire reactor vessel the heat loss is assumed to be by the way of surface to ambient radiation.

$$Q_r = \varepsilon\,\sigma\,A(T_4 - T_{amb}^4) \tag{12}$$

where epsilon is emissivity of the material and sigma is the Stefan-Boltzman constant, A the surface area, T_{amb} is the ambient temperature and T is the surface temperature.

Heat is also lost through the electrodes because they are internally water cooled. This heat loss is simulated as convective heat flux at the interfaces between the electrodes and the graphite parts. Convective cooling has the following equation

$$Q_{conv} = hA(T - T_{ext}), \tag{13}$$

where h is the convective cooling coefficient, A is the contact area between the electrodes and the graphite parts, T is the temperature of the graphite at the interface and T_{ext} is the electrode temperature.

The physics in the model from mechanical point of view only includes thermal expansion, applied force, stress, and strain. These are also used to calculate displacement of each individual node. The model assumes everything fully linearly

elastic, it is up to the user to detect when the simulated results exceed elasticity of the materials being simulated. Stress is calculated from

$$\sigma = \frac{F}{A} = \epsilon E, \tag{14}$$

where F is the applied force, A is the area the force is applied on, ϵ is the strain and E is the Young's modulus. Strain is calculated using

$$\epsilon = \frac{dl}{l_0} = \frac{\sigma}{E}, \tag{15}$$

where dl is the change in length and l_0 is the original length. The formula of thermal expansion is

$$dl = \alpha \Delta T l_0, \tag{16}$$

where α is the CTE and ΔT the temperature difference.

6.2 A Coupled Thermal–Electric Model of a Graphite Rod

A model of a solid ISO-63 graphite rod was built to determine thermal and electrical properties of the graphite system. The simulated rod had a diameter of 25 mm and length of 155 mm. The physics used in this model were from the Comsol Joule heating package. Phenomena simulated included surface to ambient radiation, convective cooling and Joule heating. Figure 27 shows the geometry used in the model as both 2D drawing and its meshed 3D form. The blue rectangles, which mark simulated voltage measurement points, correspond to points where the experimental voltage measurements were taken, while the red rectangles do the same function for temperature measurements. Top of the sample was set as the terminal while the bottom was designated as the ground, surface to ambient radiation was set to affect the radial surface of the rod. Emissivity for graphite in all models was set at 0.8 in accordance with literature [48, 50, 51, 56].

Since the cooling circuit is not modelled its effect are approximated using simulated convective cooling at the interfaces where the graphite meets the stainless steel rams. The stainless steel rams have 10 mm diameter holes in the centre, these holes are also taken into account in the model to correctly simulate the area used for cooling. The cooling circuit works by circulating water between the electrodes and a cooling tower at a constant rate while the cooling tower keeps the water close to the ambient temperature, thus keeping the heat transport capacity of the system

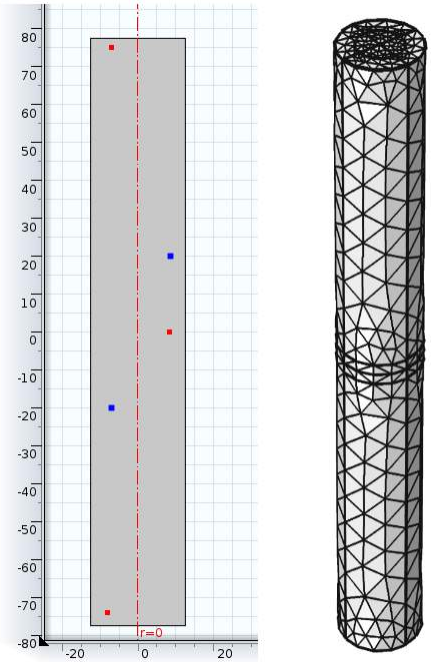

Figure 27: Geometry of the 25 mm rod used in simulations.

close to constant.

This simplification of the cooling circuit in modelling to a simple interface directly on the graphite has to be taken into account in every geometry. In case of smaller parts such as this graphite rod the effective convective cooling coefficient is very high. The high coefficient is caused by the stainless steel electrodes efficiently conducting the relatively small amount of heat generated the to the circulating water. However with larger parts more heat needs to be conducted away by the cooling circuit thus the effective convective cooling coefficient is smaller.

At this point all the materials properties and parameters required for the calculation of simulation results are known either through experiments or from literature with the exception of the convective cooling coefficient. To determine the coefficient the experimentally measured temperature profile was matched to the simulated temperatures by adjusting the coefficient until the temperatures were in agreement.

Knowledge gained from this model was used to build all further models as it confirmed the functionality of the model with the materials properties up to 900 °C in the case of thermal conductivity and 950 °C in the case of electrical conductivity. When higher temperatures are simulated the conductivity values are approximated using data from other grades of graphite as a guide, reliability of these approximations is likely degrade further away from the measured values.

6.3 A Coupled Thermal–Electric Model of a Graphite Rod With Pyrometer Hole

This model is similar in geometry and physics to the previous one with the exception of 10 mm diameter 70 mm deep holes drilled from both ends of the rod for temperature measurements using the pyrometer included in the PECS equipment. Figure 28 shows the geometry used in the model as both 2D drawing and its meshed 3D form. The purple rectangles show locations corresponding to holes drilled to the physical counterpart for the purpose of measuring either temperature or voltage. The red line denotes the surface which corresponds to the one measured using the pyrometer. Heat transfer due to radiation was ignored on the surface of the pyrometer hole, it was assumed that majority of the heat would be radiated back to the graphite with little loss.

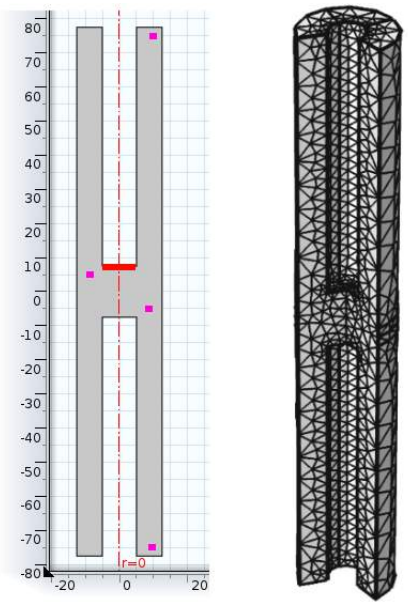

Figure 28: Geometry of 25 mm rod with pyrometer hole used in simulations.

6.4 Previous Models Implemented as a Graphite Monoblock

The graphite monoblock is a solid piece of graphite in a shape approximately to that of the entire graphite assembly used during PECS compactions. Its purpose was to help investigation of contact resistances and function as the reference with no interfaces. Further the model used was to computationally confirm or reject the findings of previous experiments and models. Another purpose was to also find

the new effective convective cooling coefficient due to moving to a wholly different geometry and significantly larger object. In this model the physics packages used were both Joule heating and heat transfer in solids, the first used in the heating phase and the latter used to simulated the cooling segment. Figure 29 shows the geometry used in the model as both 2D drawing and its meshed 3D form. The purple rectangles show locations corresponding to holes drilled to the physical counterpart for the purpose of measuring either temperature or voltage. The red line denotes the surface which corresponds to the one measured using the pyrometer.

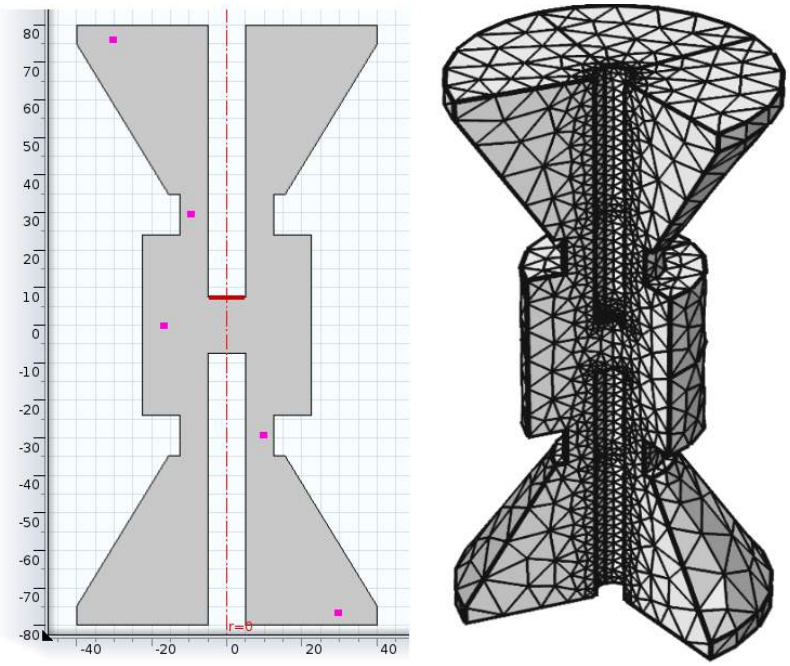

Figure 29: Geometry of the solid graphite monoblock.

The materials properties and parameters for this model are same as the ones used for the models of the rods with the exception of the to be determined convective cooling coefficient. The model uses a parametric sweep function to model the effects of multiple currents in a single simulation, the currents were selected from the PECS process logs corresponding to variety of stable dwell temperatures. The temperature profile of the simulation is matched to one measured experimentally to determine to convective cooling coefficient.

Cooling of the monoblock was modelled by taking results gained from the simulation of the heating phase using Joule heating physics and inserting them as initial values to a new simulation that uses the heat transfer in solids physics package. Modelling of the cooling phase required only the application of ambient to surface

radiation boundary condition on the outer surface and convective cooling on the ends of the monoblock.

Graphite felt is often used in PECS to limit heat loss from the surface to ambient radiation and thus lessen the power requirements and thermal gradients. An attempt was made to model the behaviour of the felt. In practice the felt will not have a good contact with the surface of the graphite die it is wrapped around, however in this simulation the contact is assumed to be solid due to the low thermal and electrical conductivity of the felt.

Figure 30 shows the geometry used in the model as both 2D drawing and its meshed 3D form. Placement of the measurement points is same as in the model without the use of the felt providing easy comparison between the experimental and simulated results. Table 2 shows the materials properties for the graphite felt as provided by the manufacturer [60], however the value for specific heat was taken from a similar competing product [61] and the emissivity was set to 0,99 due to the high specific surface area of the felt.

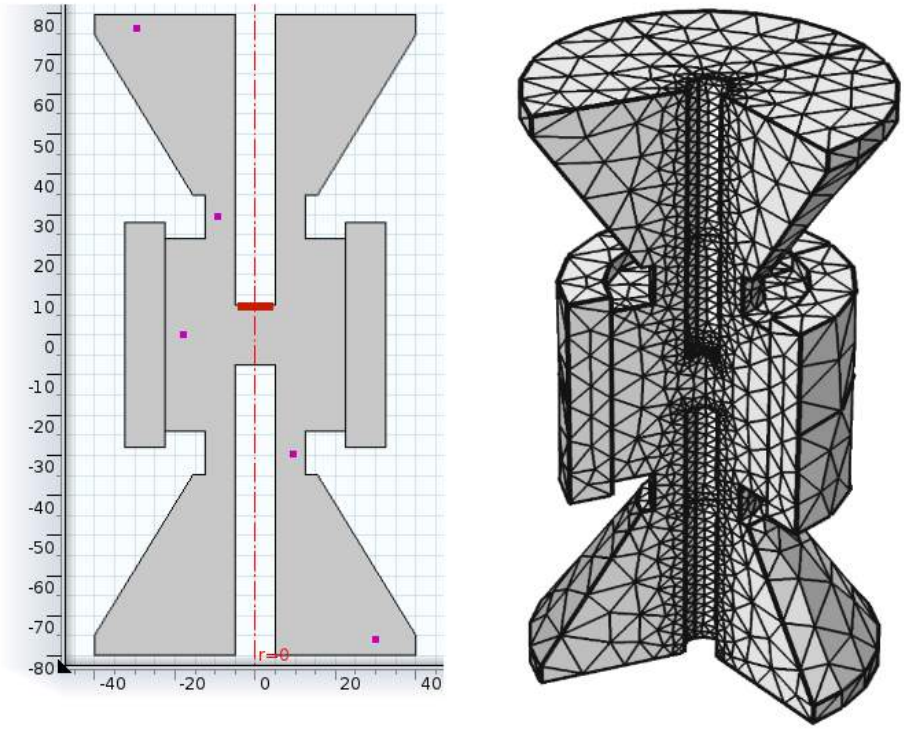

Figure 30: Geometry of the solid graphite monoblock with graphite felt wrapped around it.

Table 2: Materials properties of graphite felt.

Graphite felt		
Electrical conductivity	400 S/m	
Specific heat	0,7-5,6 $Jg^{-1}K^{-1}$	(20 - 1900 °C)
Density	110 kg/m^3	
Thermal conductivity	0,05-0,12 $W/m^{-1}K^{-1}$	(25 - 1000 °C)
Emissivity	0,99	

6.5 Modelling Graphite Part Assembly with Graphite Foil

The assembled graphite parts have approximately the same geometry as the previously used monoblock with the addition of Gr–Gr -interfaces between the parts and the option to place graphite foil either between or around the punches. The model was used to confirm validity of the modelling parameters by comparing experimental and computational results. Another purpose for the model was to find the electrical conductivity of vertically placed graphite foil. Literature indicates that the electrical conductivity of vertically placed graphite foil is linearly dependent on the conductivity of the horizontal foil [56]. In this model the physics package used was Joule heating and thermal expansion. The physics package allows the addition of mechanical forces to the model, as such boundary loads are added to the top and bottom of the geometries to simulate the effect of the compressive force exerted by the electrodes. Mechanical properties of the graphite used in the simulations are shown in Table 1. Other than the measured conductivity properties of the material foil were supplied by the manufacturer [62] or found in literature [56].

Figure 31 shows the geometries used in the model as 2D drawings. The geometries consist of two cones placed end to end with graphite punches surrounded by the die in the middle. The difference between the geometries is the increased inner and outer diameter of the die by 0,4 mm due to the thickness of the graphite foil. The purple rectangles show locations corresponding to holes drilled to the physical counterpart for the purpose of measuring either temperature or voltage. The red line denotes the surface from which the temperature was measured by pyrometer.

While the previous simulations of the heating process have been stationary, the possibility of time dependent calculation was added to this model using PID controller. The ideal version of the function for PID controller used in the model is shown in equation 17 [63].

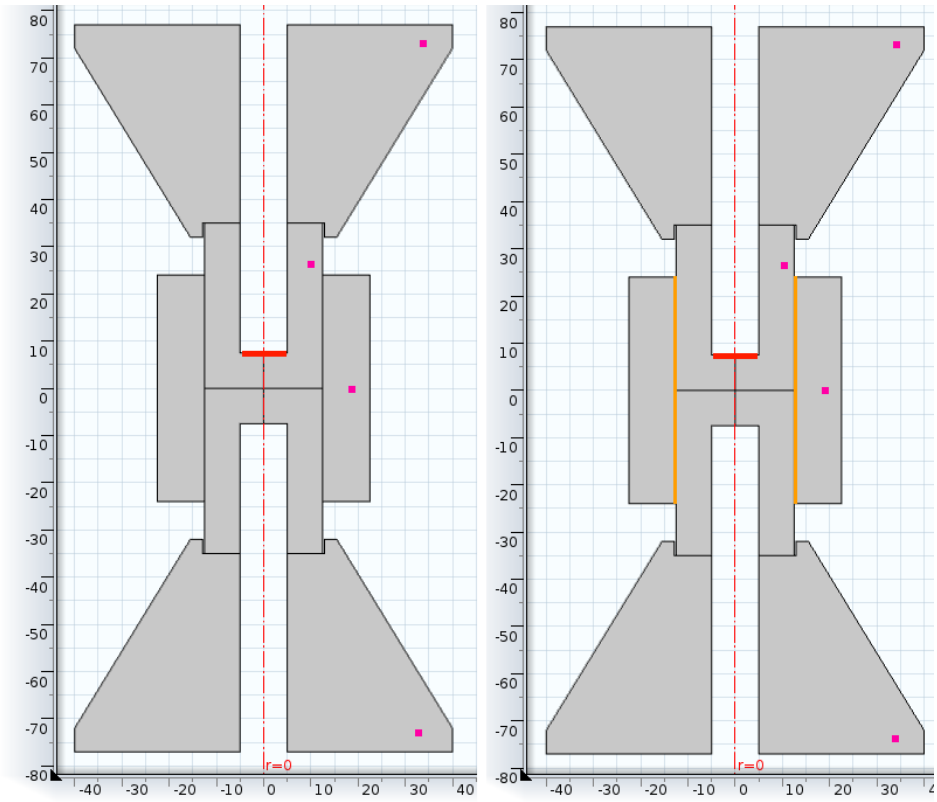

Figure 31: Assembly of graphite parts with and without vertically placed graphite foil.

$$u(t) = k_p e(t) + k_i \int_0^t e(\tau)d\tau + k_d \frac{de}{dt} \tag{17}$$

where u(t) is the control signal, e is the control signal, k_p is the proportional gain, k_i the integral gain and k_d the derivative gain. In this model the output of the function is the current controlled by set heating rate and dwell temperature.

6.6 Models of Graphite Assemblies With Copper and α-alumina Samples

These models differ from the previous one only by the presence of either a solid copper or α-alumina samples surrounded by graphite foil between the punches. Materials database of the software provided the materials properties used in the models. The models were used to simulate the behaviour of both conductive and non-conductive samples during PECS and compare the modelling results to experimental data.

Figure 32 shows the geometry used in the α-alumina model as both 2D drawing and its meshed 3D form. The purple rectangles show locations corresponding to holes drilled to the physical counterpart for the purpose of measuring either temperature or voltage. The red line denotes the surface which corresponds to the one measured using the pyrometer. Graphite foils are highlighted in orange. Geometry of the model for copper differs only in sample thickness, while the α-alumina sample was 4,8 mm thick the copper sample had thickness of 2,65 mm.

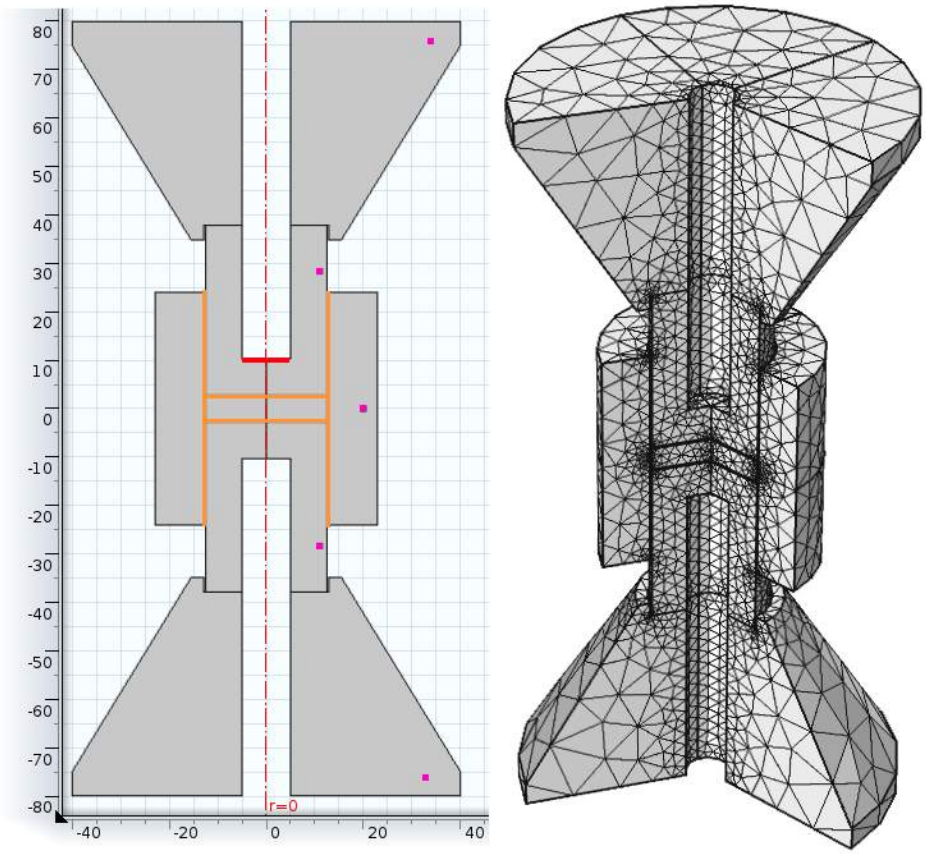

Figure 32: Assembly of graphite parts, with graphite foil and an α-alumina sample.

6.7 Densification of Copper Using the Master Sintering Curve

A method for predicting relative density of the sintered compact has been developed called the Master Sintering Curve [64]. In actuality the MSC produces a surface due equation 18 being a function of both time and temperature. The application of the MSC requires solving activation energy Q_a for the equation 18 along with the parameters for equation 19 found using results from the densification experiments [65]. The surface allows the user to choose their heating rate and process time to

reach the desired density. There exists some limitations to the MSC, the further one selects the heating rate apart from the ones used to build the curve the higher the resulting error, also the activation energy determined for the MSC will work only in single phase. The modelling software cannot use the function provided in equation 19 as is, but requires it to be partially derived in respects of both time and temperature.

$$\Theta(t,(T(t)) = \int_0^t \frac{1}{T} \exp\left(-\frac{Q_a}{RT}\right)dt = \frac{t}{T} \exp\left(-\frac{Q_a}{RT}\right) \tag{18}$$

$$R.D. = A_2 + \frac{A_1 - A_2}{1 + \exp\left(\frac{\log(\Theta) - x_0}{dx}\right)} \tag{19}$$

This model uses all the same parameters and boundary conditions as the previous one with the exception of the materials properties of copper being multiplied by the relative density as calculated by the MSC. The results of the model are compared to densification data from an experiment that was not used in creation of the MSC.

6.8 Modelling Sintering of an 80 mm Copper Disk

A new geometry was built for modelling PECS of 80 mm diameter copper disk. Physics and boundary conditions apply as in previous models. With larger diameter copper compact a more significant thermal gradient leading to density gradient was expected from experimental and modelled here. Figure 33 shows the modelled geometry in 2D and 3D. The spots used for pyrometer and thermocouple measurements are marked on the figure in red.

6.9 Modelling PECS with Complex Geometries

Two PECS compactions were simulated where WC-12Co powder was compacted into two complex shapes. Physics and boundary conditions used in the model are same as the previous models with the addition of increased pressure of 50 MPa applied by the electrodes and new materials properties for the WC-12Co powder and hexagonal boron nitride (hBN) coating.

The shapes are shown as 2D representations in Figure 34, where graphite foils are marked in orange and the pyrometer measurement surface in red. The blue on the upper surface of the samples in the figure denotes the presence of hBN sprayed on the surface in place of the graphite foil. The height of the step and the rounded top in the models is 3 mm while the diameter of the samples is 36 mm.

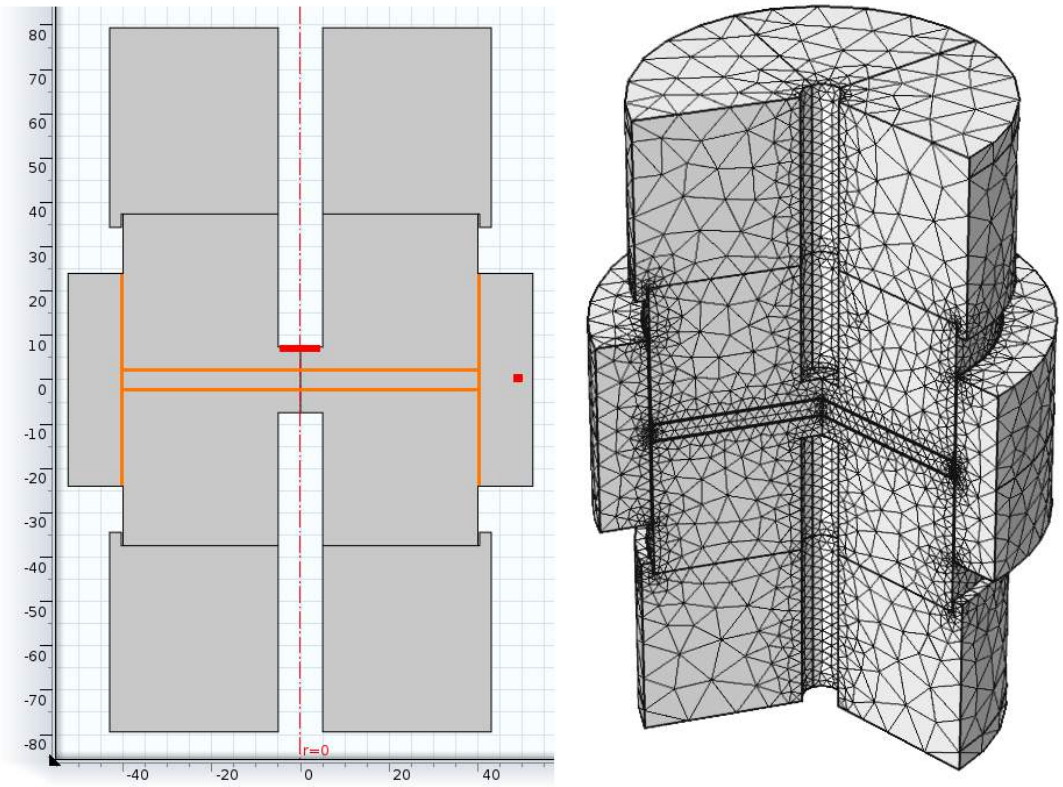

Figure 33: Model of an 80 mm copper disk enclosed by graphite parts.

The hBN coating was modelled as 100 μm thick electrically insulating and thermally resistive layer. hBN was modelled as electrically insulating due to its lack of free electrons [66]. The thermal conductivity that was used for the thermally resistive layer of hBN and is shown in Table 3 [67].

Table 3: Thermal Conductivity of hBN.

Temperature (°C)	Thermal Conductivity ($Wm^{-1}K^{-1}$)
20	65
400	50
700	30
1000	15

The materials properties used for WC-12Co were found both in literature [68], and in the case of coefficient of thermal expansion ($\alpha = 5,6 \times 10^{-6} K^{-1}$) in the Comsol materials database. The materials properties found in literature are shown in Figure 35.

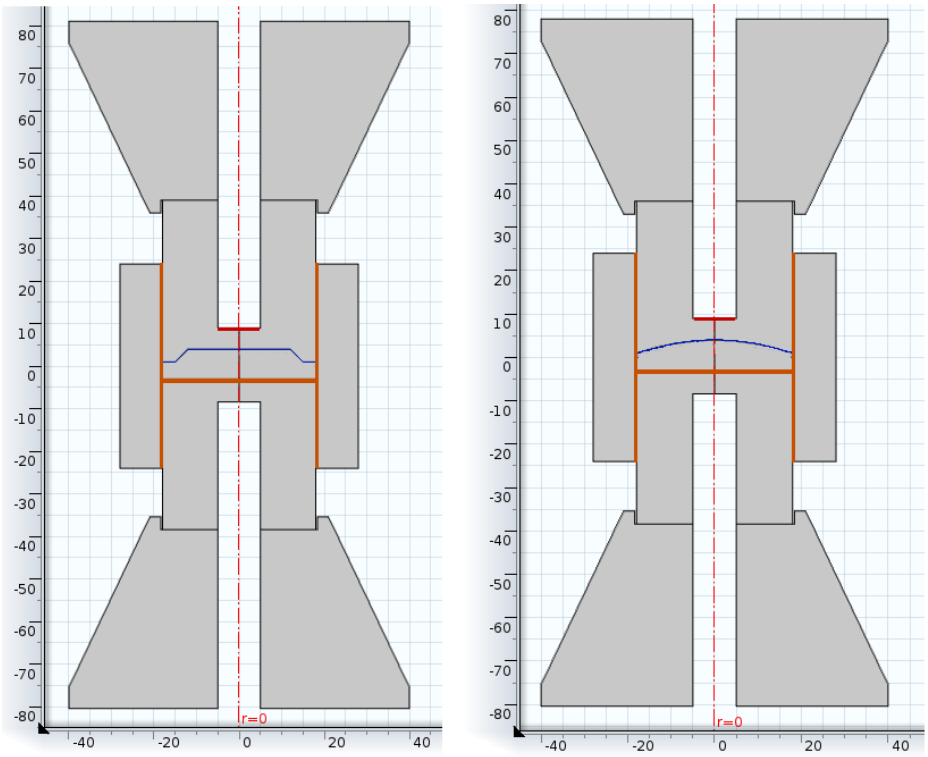

Figure 34: 2D geometries of the complex shapes being modelled.

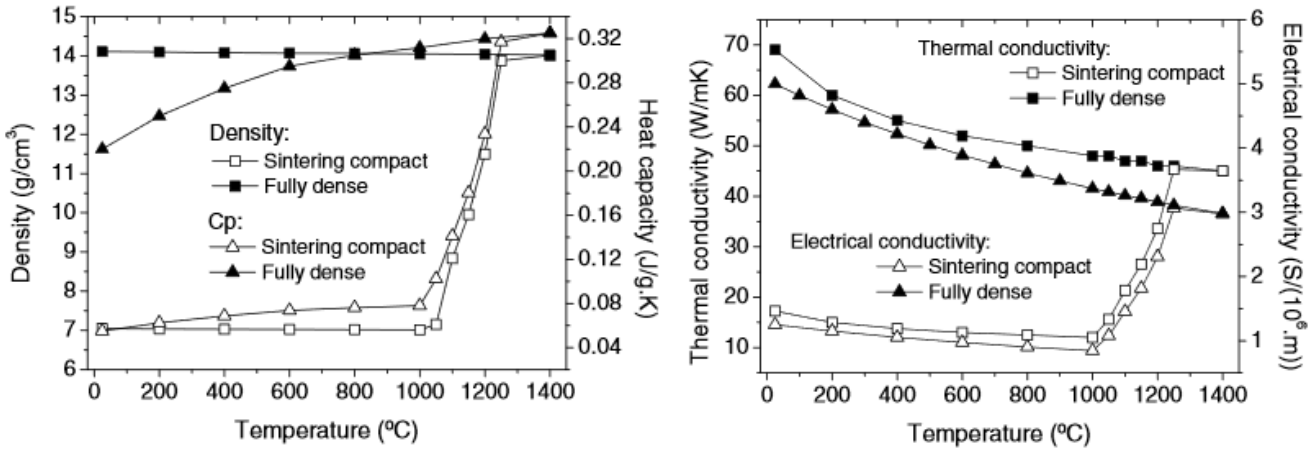

Figure 35: Physical properties of WC-12Co [68].

7 Results

This chapter presents the results from both experiments and simulations. The results include thermal and electrical properties of the graphite parts, determining the effects of cooling during sintering, simulated PECS processes using fully dense conductive and non-conductive samples and compactions of copper. Further the results gained from sintering of compacts with complex geometries are presented and compared to simulations.

7.1 Materials Properties and Model Construction

Figure 36 shows the resistivity and conductivity of the ISO-63 graphite measured as function of temperature. The temperature was measured using a thermocouple and later experiments showed a difference between the thermocouple and pyrometer temperature readings. The thermocouples used gave higher temperature readings than the pyrometer and the difference increased with temperature. Table 4 shows the measured resistivity and conductivity values as well as their adjusted temperatures. The pyrometer only measures temperatures above 500 °C, thus the thermocouple temperature measurements below this temperature are assumed to be accurate. The ambient temperature values were taken from Table 1 and confirmed to be accurate by a four point probe measurement.

The measured resistivity and conductivity for the graphite is used in all models. Figure 37 shows a simulated 25 mm diameter rod reach 675 °C using 560 A of current. When the temperature adjustment is taken into account the result matches well with experimentally measured 700 °C. The figure also shows the simulated temperature difference between the surface that the pyrometer measures and the position from which the thermocouple measures. This simulated temperature difference was taken into account when calculating the adjusted temperatures.

Table 4: Electrical properties of ISO-63 graphite as a function of temperature.

Resistivity & Conductivity of ISO-63 graphite											
Temperature	25	200	300	400	500	600	700	800	900	975	°C
Temperature (adj.)	25	200	300	400	483	578	675	769	866	937	°C
Resistivity (10^{-5})	1,65	1,43	1,28	1,17	1,09	1,03	0,99	0,98	0,97	0,96	Ω*m
Conductivity (10^{3})	61	70	78	86	92	97	100	102	103	105	S/m

During the experiments it was also noticed that the graphite parts may contain volatiles which affect the electrical measurements. This was confirmed by using new

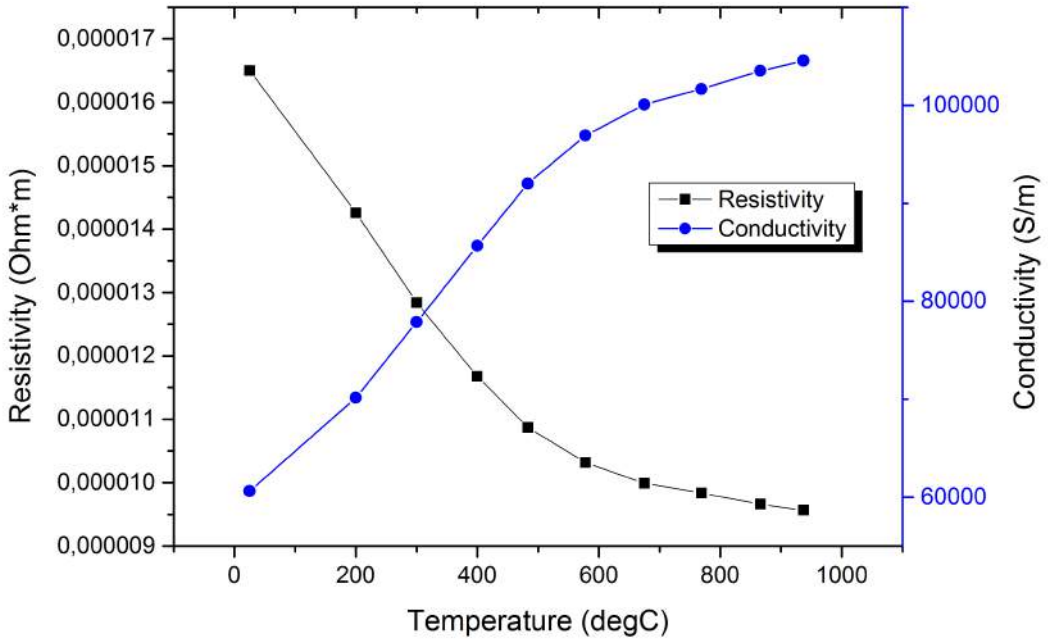

Figure 36: Resistivity and conductivity of the ISO-63 graphite as functions of temperature.

graphite parts and measuring the potential difference between two points in repeated experiments. Table 5 shows the measured voltage difference decreasing significantly from first to third experiment. From the third repeat the effect of volatiles on the results was no longer detected. The knowledge about the effect of volatiles was used in design of the experiments to avoid erroneous results by heating the graphite multiple times before measurements were taken.

Table 5: Effect of volatiles on measured voltage difference in ISO-63 graphite.

Effect of volatiles on voltage measurements							
Temperature	500	600	700	800	900	975	°C
Voltage (run #1)	399	435	469	498	530	558	mV_{RMS}
Voltage (run #3)	309	343	376	416	453	486	mV_{RMS}

Thermal conductivity of the graphite was calculated from thermal diffusivity measured using the Laser Flash method and specific heat. The specific heat values used were chosen from literature. The calculations were done using equation 2. Table 6 shows the temperature dependent thermal properties for the graphite, which are further illustrated in Figure 38. These thermal properties are used in every model and simulation for the graphite.

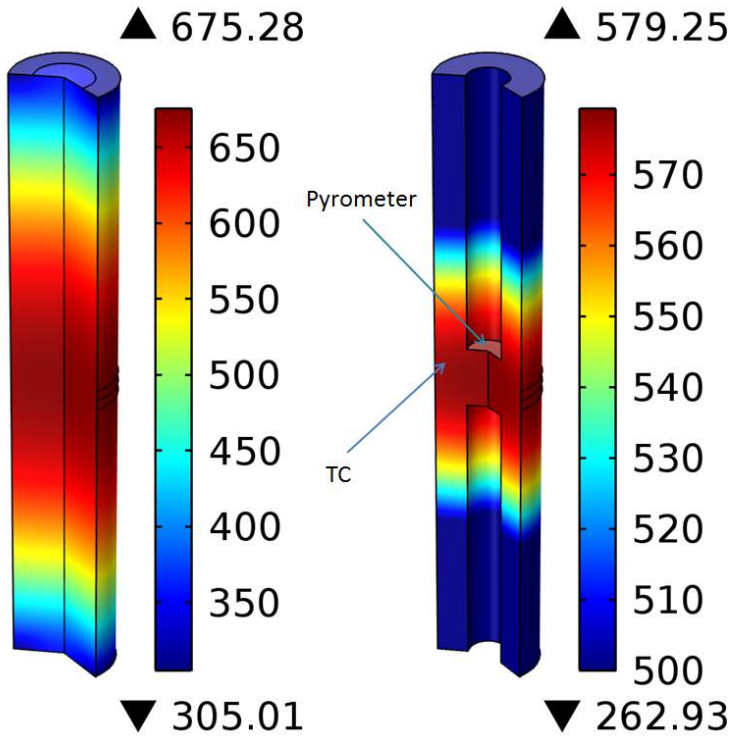

Figure 37: Simulated 25 mm graphite rods with and without pyrometer hole.

Table 6: Thermal properties of iso-63 graphite

Specific heat, thermal conductivity and diffusivity						
Temperature	100	300	500	700	900	°C
Thermal diffusivity	5,32E-05	3,28E-05	2,47E-05	2,03E-05	1,71E-05	m^2/s
Specific heat	934	1391	1626	1761	1850	J/(kg °C)
Thermal conductivity	91,3	83,8	73,8	65,4	58,1	W/(m °C)

With the required materials properties for graphite known the next step was to validate their use in models by experiments and simulations. A monolithic graphite block in the shape and dimensions matching the graphite parts used in compactions was run through the PECS process and simulation using same process parameters. Convective cooling for the monoblock and other simulations using similar geometry was determined by performing the monoblock simulation multiple times using different values for the convective cooling. Because the convective cooling coefficient is the only unknown variable the correct value for it was found by comparing the simulated and experimental temperatures during dwell times and using the value that resulted in best match. Cooling phase of the process was also simulated and

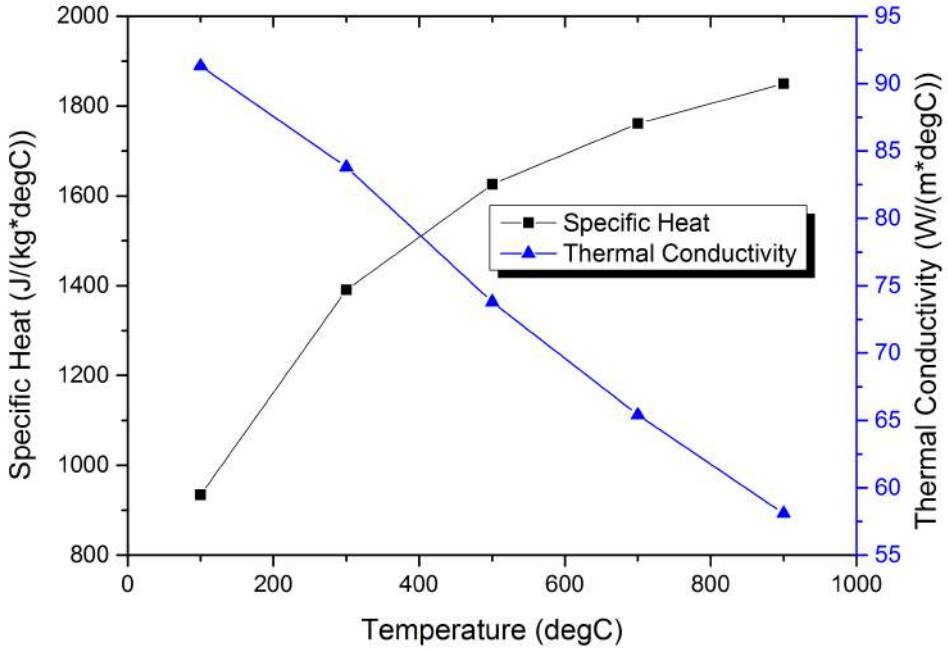

Figure 38: Thermal conductivity of ISO-63 graphite and specific heat used to determine it.

the temperatures matched well with experimentally measured in the start of the cooling and diverging more as more time had passed. An attempt was also made to determine the convective cooling coefficient from the process data during the cooling segment after the heating had been turned off. However the result proved to be less accurate compared to one measured for multiple stable temperatures.

Table 7: Determining the convective cooling coefficient by attempting different values provided a well matching result

Measured & simulated temperatures at known currents						
Current, A	960	1100	1240	1390	1550	1650
T, °C (pyro)	500	600	700	800	900	975
T_{sim}, °C (pyro)	492	589	690	798	902	974
T, °C (electrode)	168	201	233	265	298	323
T_{sim}, °C (electrode)	169	200	231	263	296	320

The temperatures compared were the surface that the pyrometer measures from and a 5 mm deep hole drilled in the lateral surface 3 mm away from the electrode. Table 7 shows the measured and simulated temperatures for known currents. Based on these results the convective cooling coefficient for the monoblock was determined to be the simulated 1000 W/m^2K. Figure 39 shows a comparison between simulated and experimentally measured cooling curve using the determined convective cooling

coefficient. The temperatures for both curves were measured from the pyrometer surface. The cooling curves show great similarities between the experimental and simulated, however the convective cooling coefficient obtained by simulation is larger and more accurate during the heating phase.

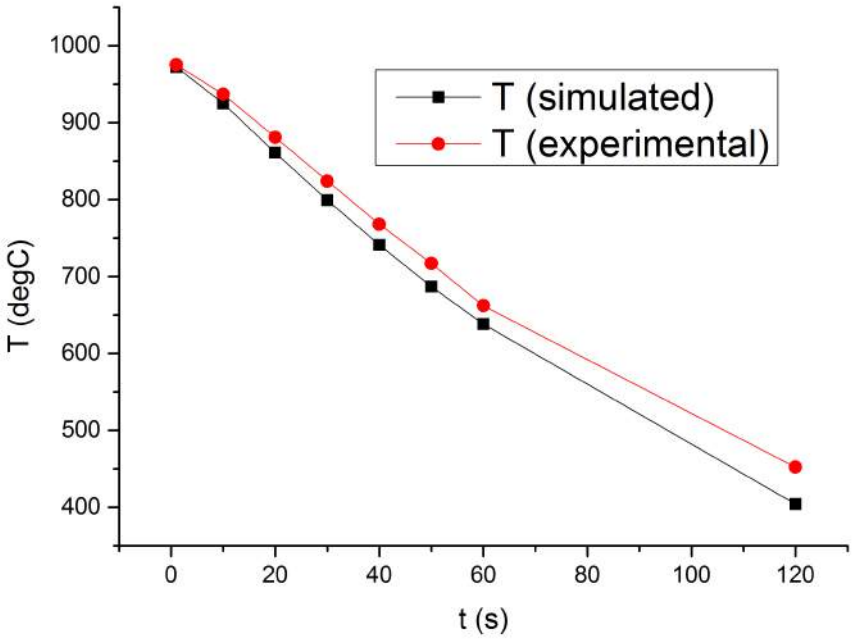

Figure 39: Simulated and experimentally determined cooling curves for the monoblock.

A comparison between experimentally measured and simulated voltages was also carried out. In experimental part the voltage difference was measured from 5 mm deep holes on the lateral surface of the monoblock 3 mm distance from the electrodes on both top and bottom. Figure 40 shows the voltages as function of current. The experimental and simulated data show good agreement and validates the experiments to find the resistivity and conductivity of the graphite.

In further experiments multiple graphite parts and graphite foil were used, creating graphite–graphite and graphite–foil -interfaces. The interfaces have electrical contact resistances characteristic to them, the magnitude of which was experimentally measured. In addition electrical properties of the graphite foil were determined. Three experiments were compared, first with the 155 mm long 25 mm diameter graphite rod schematic of which is shown in Figure 27, the second with two 77.5 mm graphite rods placed end to end creating a graphite–graphite -interface and the third with the same 77.5 mm graphite rods this time with graphite foil between

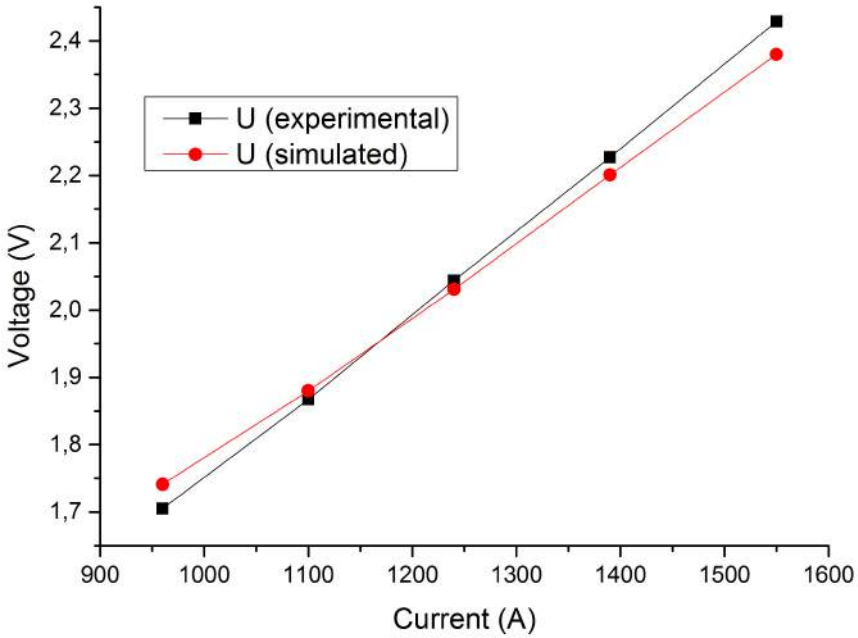

Figure 40: Simulated and experimentally measured voltages for the monoblock.

them. The voltages were measured over a distance of 40 mm. Figure 41 shows that the difference between voltages measured over the solid graphite and the foil interface stays nearly constant independent of temperature. However the behaviour of the graphite–graphite -interface is odd, and the experiment was repeated with similar results. There is no voltage difference compared to solid graphite beyond margin of error measured at 200 °C, while the difference is significant at 975 °C. Explanations for this result include possibility of the graphite rods slipping against each other or deformation at higher temperature distorting the interface. For purpose of this thesis it is assumed that no contact resistance exists at graphite–graphite -interfaces.

Resistivity of the graphite foil was calculated from the difference between the measured voltages in the solid graphite experiment and the foil interface experiment using equation 4. Any contact resistances at the interface were assumed to be due to the foil and thus included in the properties of the foil. The electrical properties of the graphite foil are dependent on its orientation to the current, a foil placed in the direction of current has multiple times higher conductivity [56]. Table 8 shows the temperature dependent resistivity and conductivity of the graphite foil.

Determining the electrical conductivity for vertically placed graphite foil was performed by experimenting with and modelling two set-ups one with and one without the vertically placed graphite foil. The modelled set-ups are shown in Figure

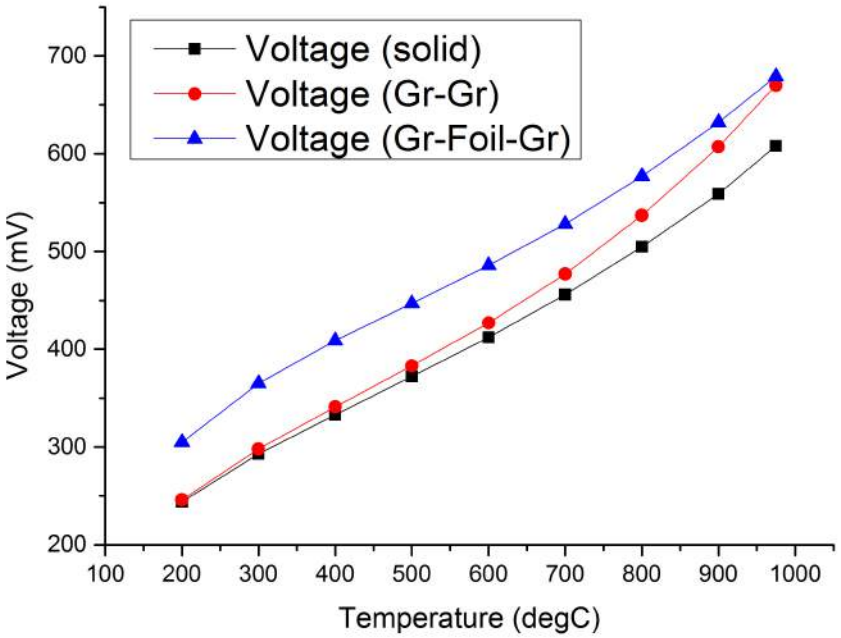

Figure 41: Comparison of voltages measured over no interface, Gr–Gr -interface and Gr–Foil–Gr -interface.

Table 8: Determining the resistivity and conductivity of horizontally placed graphite foil

Resistivity & conductivity at different temperatures										
Temperature	200	300	400	500	600	700	800	900	975	°C
Resistivity_h	0,45	0,37	0,31	0,25	0,24	0,20	0,16	0,14	0,13	mΩm
Conductivity	2244	2668	3240	3984	4217	4984	6314	7053	7539	S/m

31. The differing die geometries affect the comparability of the results slightly. In both experiments the voltage difference was measured between 3 mm deep hole 3 mm above the die in the punch and a 5 mm deep hole in the middle of the die lengthwise. The validation results are shown in Figure 42. The measured and simulated voltages for the geometry without foil are in agreement with each other validating the earlier assumption made on contact resistances in graphite–graphite -interfaces. The results also show good match between the experimentally measured and simulated voltages over the vertically placed graphite foil using a factor of five in multiplying the conductivity shown in Table 8.

Models simulating PECS of α-alumina and copper were built and tested against matching experimental scenarios and the results were compared. Figure 43 compares

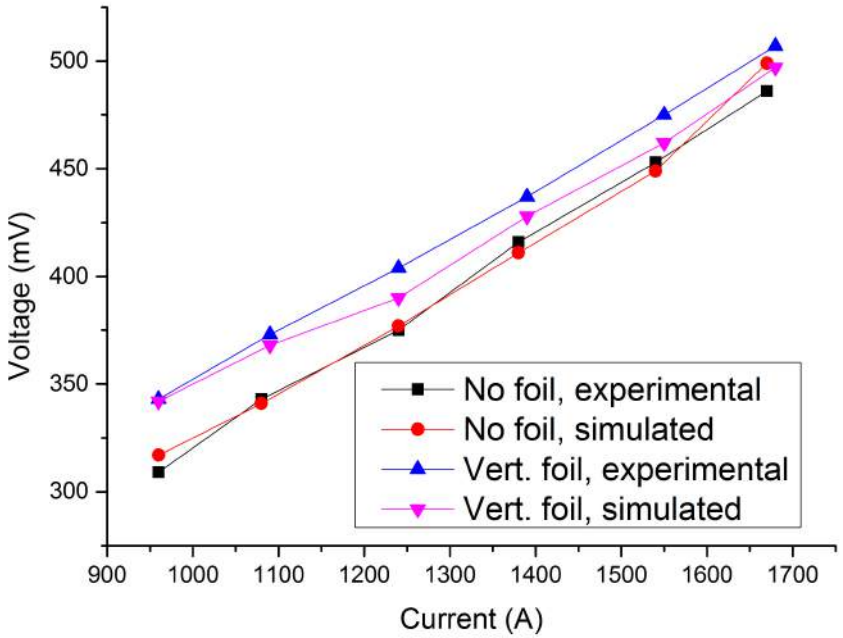

Figure 42: Voltage measurements in both experiment and simulation validate the measured electrical properties for Gr–Gr -interfaces and graphite.

the simulated and measured temperatures for α-alumina read by the pyrometer, and the voltage difference simulated and measured from both punches. The results for both the temperature and potential difference show little difference from simulation to experimental, the difference in temperature readings decreases from 22 to 1 °C and the difference in voltages does not exceed 22 mV. Figure 44 shows the voltage and temperature comparisons for the copper model and experiment. These results show consistent temperatures between the model and experiment, however the potential difference results diverge with increasing current. The divergence may have been caused by direct contact between the copper and the graphite punch allowed by thermal expansion.

The models of α-alumina and copper also show the typical behaviour of conductive and non-conductive samples in PECS process where part of the current flows through the conductive sample compared the non-conductive sample where the current flows around it. Figure 45 shows the modelled current densities from the centre of the sample outwards. The simulated samples are also surrounded by graphite foil which affects the current density distribution in Cu, without graphite foil above and below the sample more current would flow through it. Neither sample heats up from heat generated inside the sample material by Joule heating, one due to very low resistance while the other due to very high resistance. However the current

densities differ in the surrounding graphite, an example of this is the larger amount of Joule Heating in the die surrounding the α-alumina sample compared to a die with copper sample inside, the opposite is also true and the areas of punches near the samples generate more heat when copper sample is used.

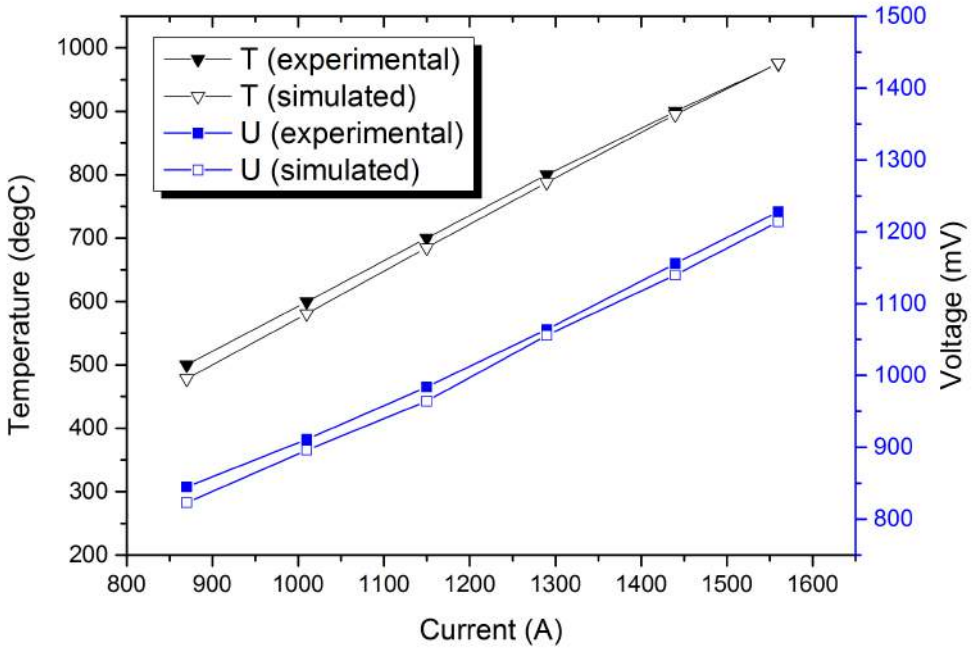

Figure 43: Temperatures and potential differences measured in simulated and experimental PECS processes on α-alumina.

Thermal gradients for α-alumina model were simulated on both horizontal and vertical cross-sections. Figure 46a shows that in this case the thermal gradient between the pyrometer measuring surface and centre of the sample is less than 1 °C. Hotspots in the figure are shown surrounding the pyrometer hole. Figure 46b shows larger gradient inside the sample, from centre to edge the temperature difference is 4 °C.

PID controlled models were used in simulation of temperature evolution mimicking the experiments, Figure 47 shows both (a) α-alumina and (b) copper compacts being heated at 50 °C/min until reaching dwell with temperatures registered from the pyrometer, centre of the sample and radial surface of the sample. In case of the α-alumina the temperature gradient between centre of the sample and edge has increased significantly from 4 to 10 °C, while the gradient from pyrometer to the centre has increased by only one degree compared to results shown in Figure 46. The increase of radial gradient is caused by the surface to ambient radiation increasing

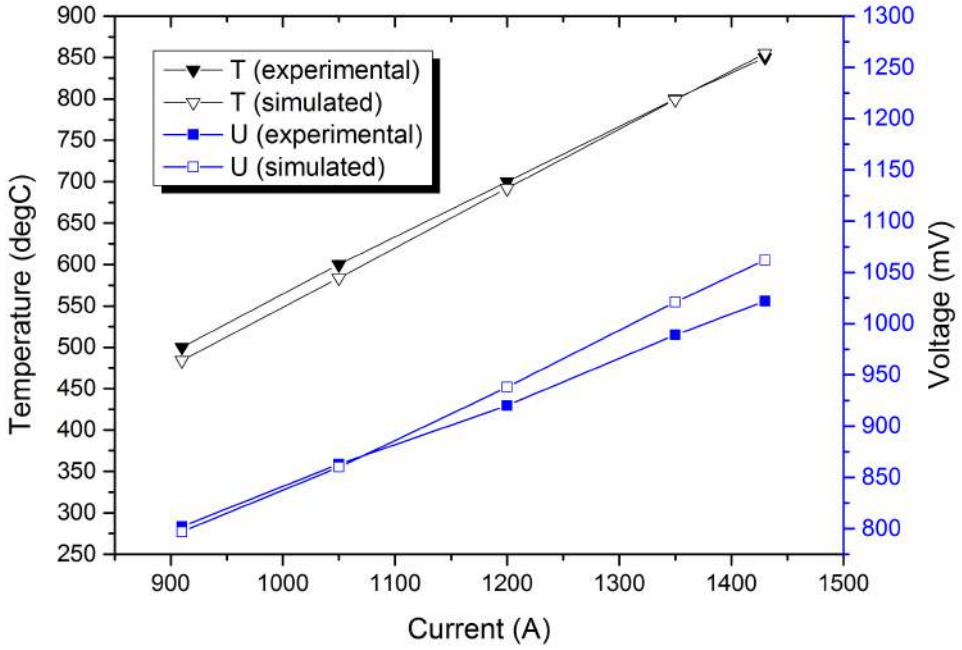

Figure 44: Temperatures and potential differences measured in simulated and experimental PECS processes on copper.

exponentially with temperature. The copper compact shows smaller gradients than alumina, even when compared to results in Figure 46 which are simulated at higher temperatures, this can be attributed to the good conductive properties of copper.

The thermal gradients in radial direction caused by heat loss by surface to ambient radiation can be mitigated by surrounding the die with an insulating layer of graphite felt. The effect of the graphite felt use was simulated and measured while the felt was wrapped around the monoblock and the results were compared to those obtained without the use of felt. Figure 48 shows the similarity of the temperature evolutions in the experiments and corresponding simulations. In case of felt the temperature difference difference between the experimental and simulation shows decrease with increasing temperature, with the difference being less than one degree at 975 °C. The use of felt also decreased the amount of current required for heating, at 975 °C the difference amounted to 300 A.

Figure 49 shows simulated temperature gradients from the centre of the monoblock to 12.5 mm in radial direction with and without the use of graphite felt. Temperature gradients to radial direction were small when measured at 500 to 600 °C regardless of felt use. Without the use of felt the temperature gradient increases exponentially

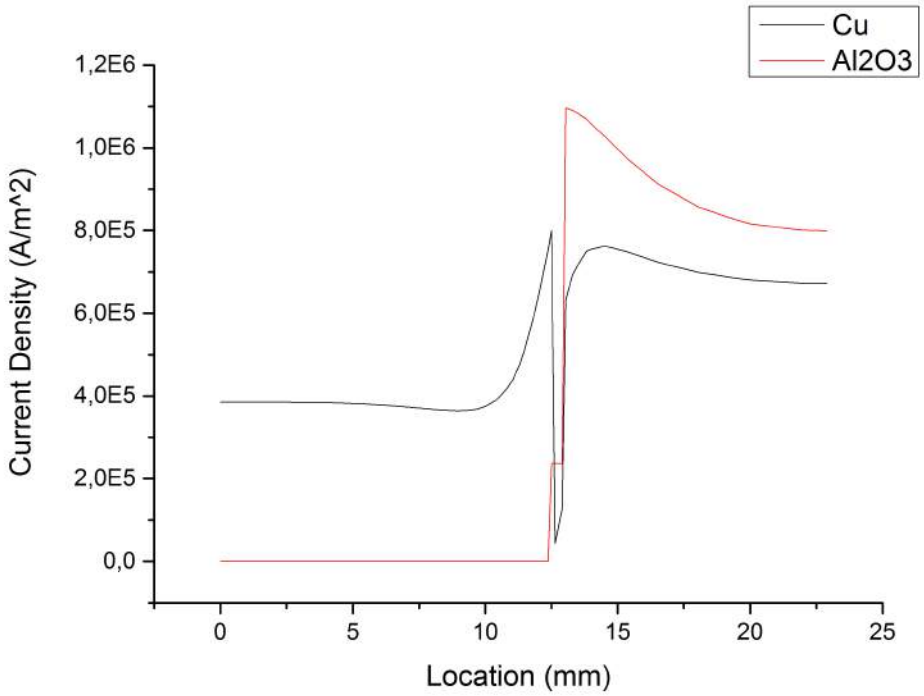

Figure 45: Current densities simulated from the middle of the copper and α-alumina samples to outer surface of the die.

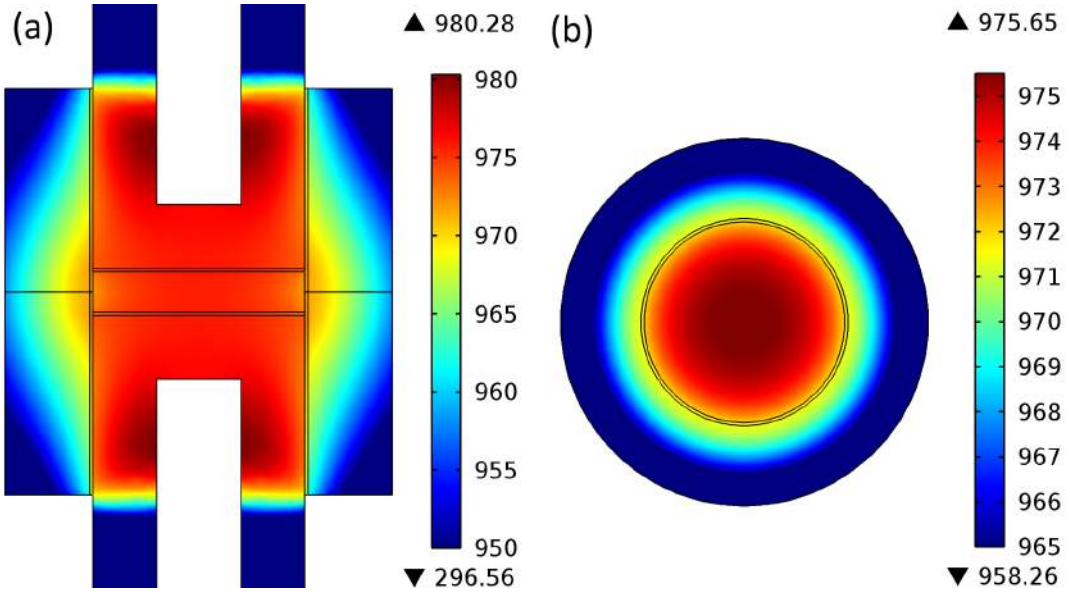

Figure 46: Temperature gradients simulated for α-alumina, the figure includes (a) vertical cross-section, (b) horizontal cross-section of the sample and surroundings.

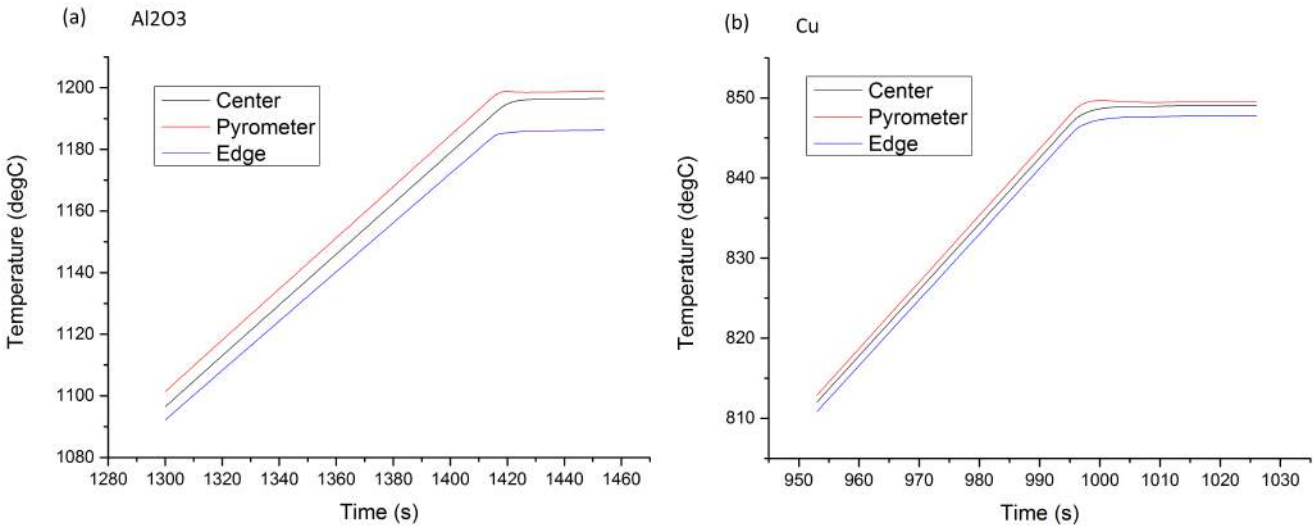

Figure 47: Temperatures measured at the centre and edge of the samples and pyrometer for (a) α-alumina and (b) copper.

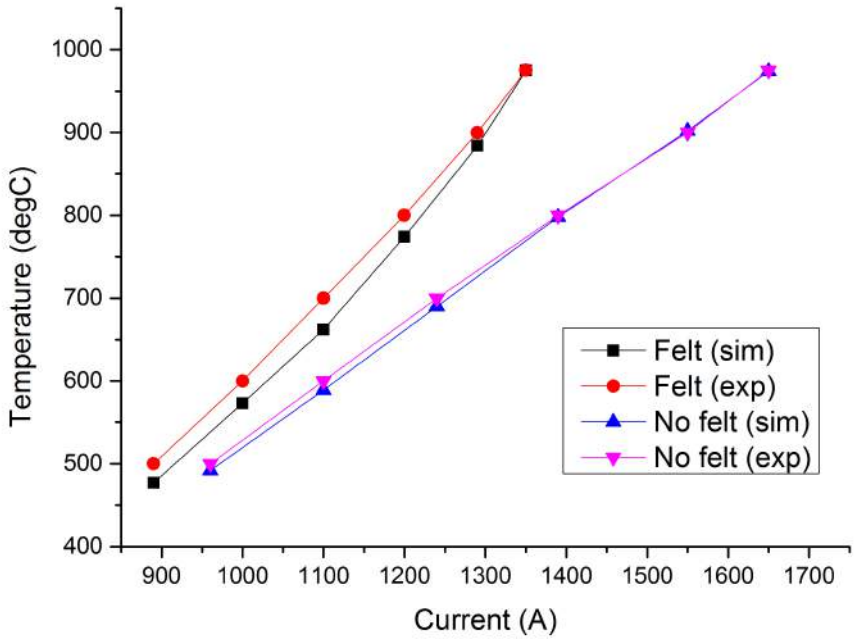

Figure 48: Simulated and measured temperatures as a function of current with and without the use of graphite felt.

with the pyrometer temperature reaching over 6 °C at 975 °C. Use of graphite felt around the monoblock decreased the simulated temperature gradient to less than 0.8 °C at the same temperature.

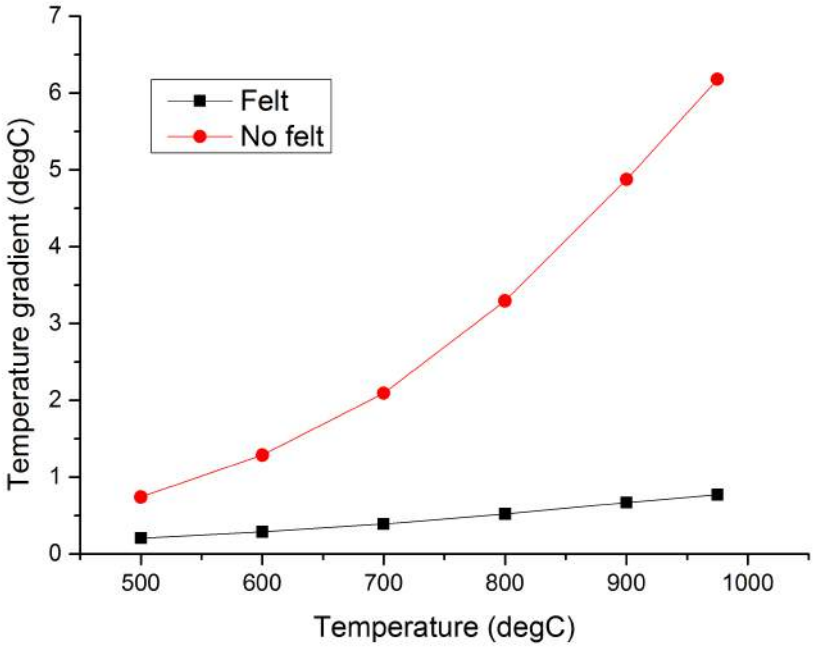

Figure 49: Simulated heating of monoblock with and without felt use. Temperature gradients as a function of radial position from the centre of the sample to 12.5mm to the radial direction.

7.2 Densification of Copper Powder

7.2.1 Construction of Master Sintering Curve and its FEM implementation

Densification of copper was investigated using 75 μm copper powder. The evolution of relative densities in the copper compacts was measured as a function of temperature and time using the piston position value from PECS process logs and final densities of the compacts. To prevent thermal expansion of the ISO-63 graphite and deformation of the graphite foil from affecting the results the experiments were repeated sans powder and the resulting piston movement subtracted from the powder experiment results. Final densities and relative densities of the copper compacts are presented in Table 9, while Figure 50 shows the evolution of the relative densities at heating rates of 50 and 100 °C/min.

Trial and error method was used to find out the correct activation energy for the function $\Theta(t, T(t))$ (equation 18). Results for $\log(\Theta(t, T(t)))$ were calculated with variety activation energies for heating rates 50 and 100 °C. The measured relative densities were plotted as functions of $\log(\Theta)$. A Boltzmann sigmoidal curve

Table 9: Measured final densities of the Cu compacts measured by Archimedes' method.

Heating rate	Density	Relative Density	T_{max}
50 °C/min	8,678 g/cm^3	96,85 %	
75 °C/min	8,675 g/cm^3	96,82 %	650 °C
100 °C/min	8,676 g/cm^3	96,84 %	

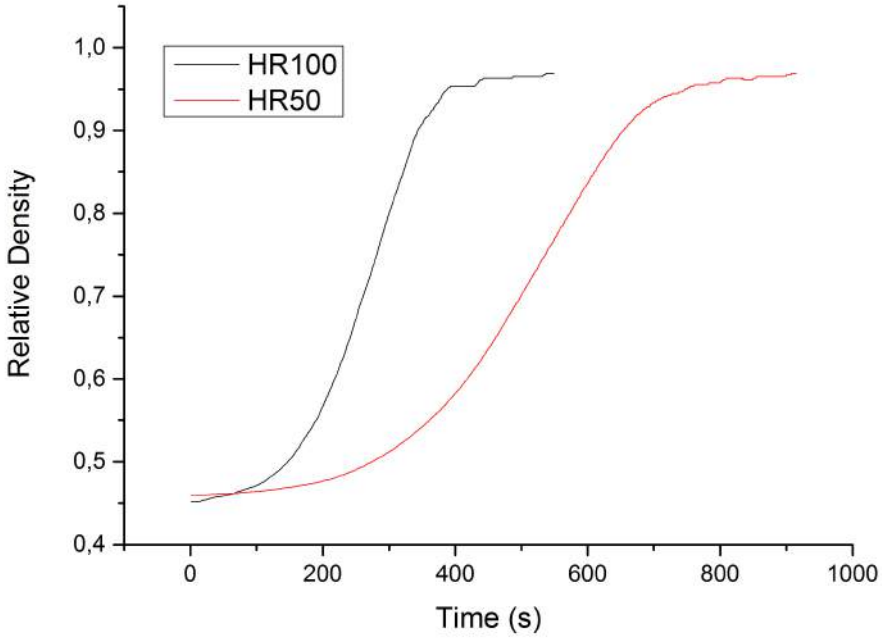

Figure 50: Evolution of relative density of copper compacts during PECS. The evolution of relative density was calculated from piston movement in the furnace.

was fitted to the plots, the activation energy which produced the plot with smallest residual mean square was selected. Further the fitting results give numerical constants required for the use of equation 19. Figure 51 shows the relative density as function log(Θ)using activation energy Q_a of 198 kJ/mol and Figure 52 shows the residual mean squares as function of activation energy, the lowest value for mean square corresponding to 198 kJ/mol.

The constants given by the sigmoidal fitting and other parameters required by equation 19 are shown in Table 10. Parameters A_1, A_2, x_0, and dx are the fitting constants, while R is the gas constant. Using the parameters from the table in equation 19 in combination with time and temperature results in an instantaneous relative density for copper. Figure 53 shows that the equation forms a surface through which a sintering path can be chosen for a desired final density. The shape of the surface

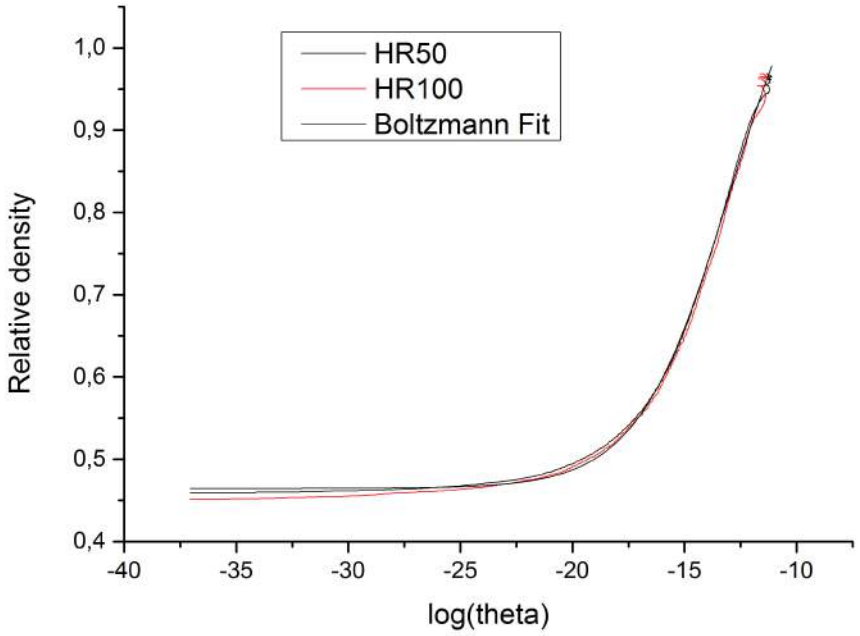

Figure 51: Log(Θ) plotted against the relative density evolution of the Cu compacts.

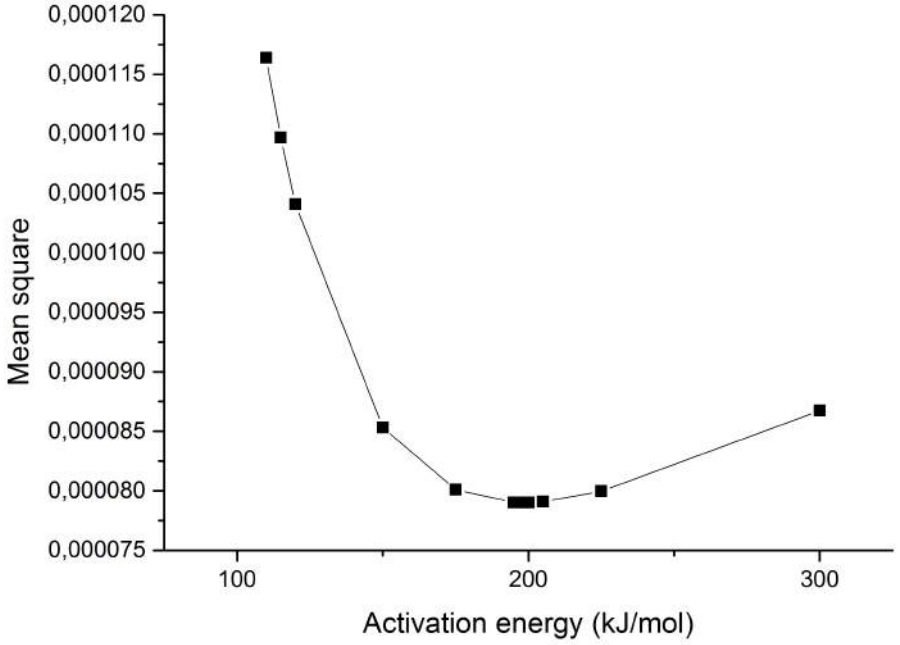

Figure 52: Residual mean squares of log(Θ)-R.D. fittings at various activation energies.

indicates that density of the compact can be increased by increasing either time or the maximum temperature with the functions temperature dependence being higher than the time dependency. An attempt made to sinter same copper powder at maximum temperature of 800 °with heating rate of 100 °C/min, however the end result was melting of the material.

Table 10: Parameters for equation 19.

Parameter	Value	Unit
Q_a	198	kJ/mol
R	8,3145	$J/mol^{-1}K^{-1}$
A_1	0,46475	
A_2	1,18162	
x_0	-12,99069	
dx	2,03863	

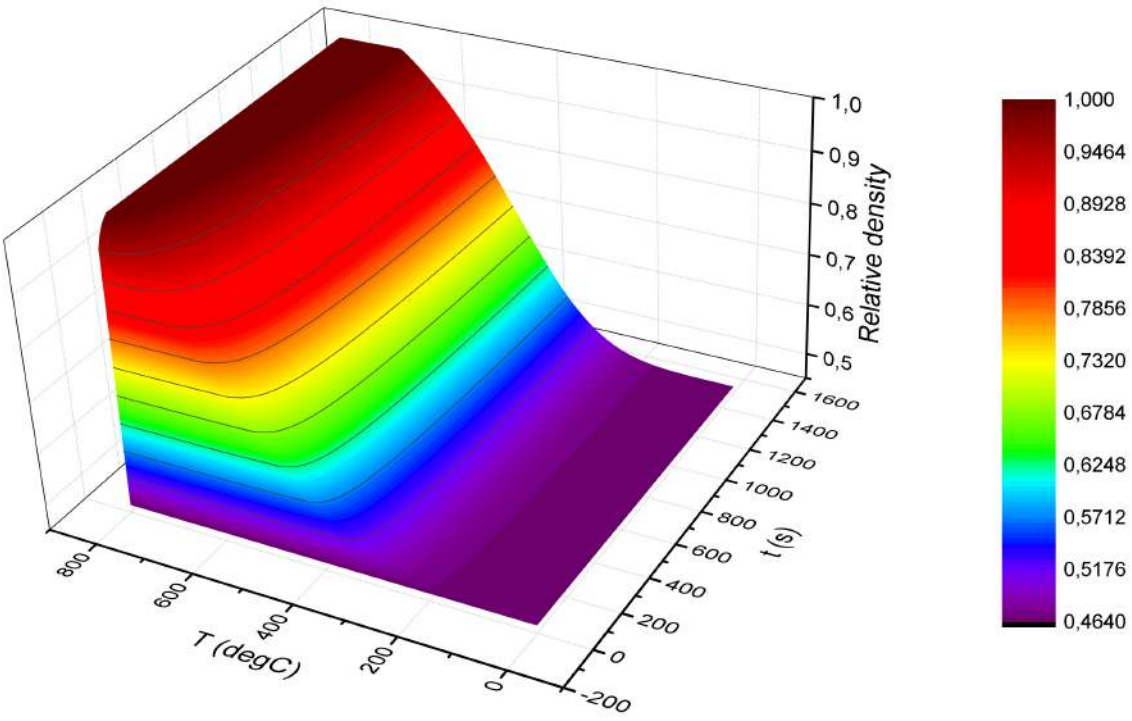

Figure 53: A densification surface formed by equation 19 with t from 0 to 1500 s and T from 0 to 800 °C.

The copper compact sintered from the same powder stock at 75 °C/min was used in validation of the master sintering curve. Figure 54a shows the evolution of

experimentally measured relative density and master sintering curve as functions of temperature, only a small differences are present between the curves. Figure 54b shows the speed of densification as calculated from experimental results and MSC plotted against time. The experimentally measured densification rate was calculated as average of a 10 second span due to large fluctuations in process log data, the plot of the averaged densification rate differs little from one calculated with the MSC. Fluctuations close to the ends of both figures were caused by unstable temperature during the dwell time of the compaction.

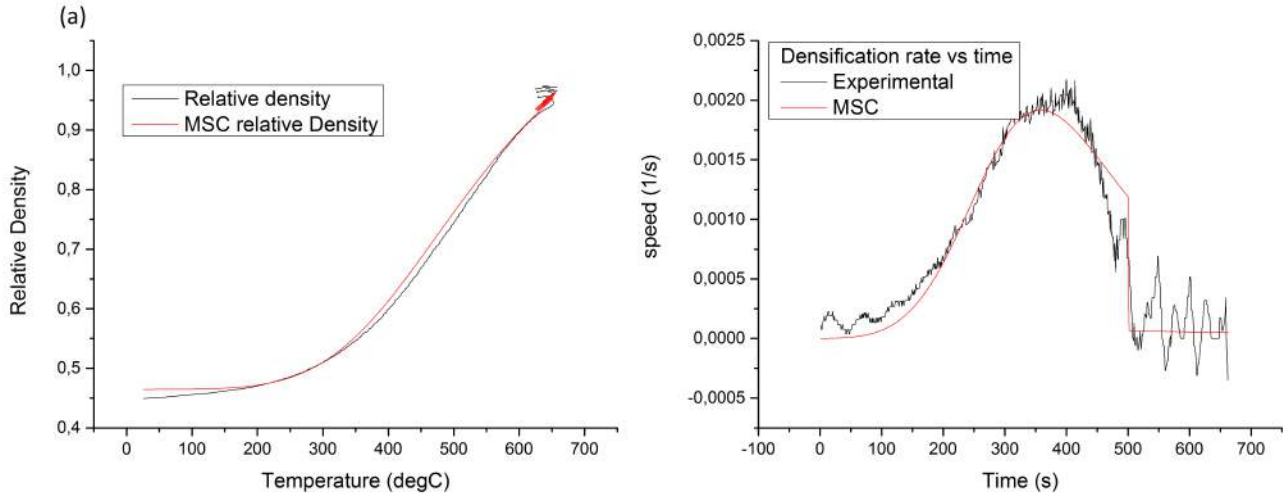

Figure 54: (a) Experimental densification and one calculated using MSC as functions of temperature, and (b) experimentally measured densification rate and densification rate calculated using MSC as functions of time.

The MSC created for copper was added to the COMSOL model. Figure 55 shows (a) the simulated evolution of density at the centre the sample as function of time and (b) the density gradient present at the end of the dwell period. The simulated density gradient was less than 0.1 % inside the copper sample. Low final density present in the figures is explained by thermal expansion, consequently it is prudent to use relative density values for comparisons across different temperatures.

7.2.2 PECS of an 80 mm Diameter Copper Compact

A large copper disk with diameter of 80,15 mm and weight of 147,24 g was sintered with the aim of measuring density changes between the centre and the edge of the sample. Figure 56 shows a drawing of the copper compact, included are the relative densities measured using samples cut from their respective locations as indicated on

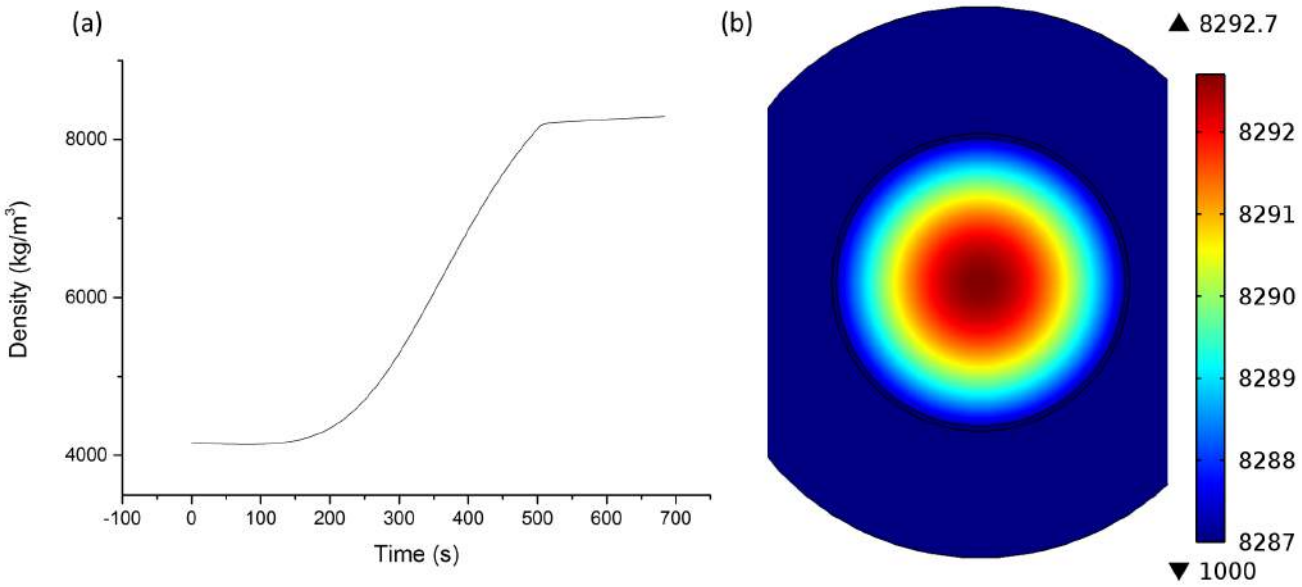

Figure 55: (a) evolution of density at the centre of the Cu sample as a function of time and (b) simulated cross-section of the Cu sample displaying density gradient at the end of the dwell period.

the figure. The large differences in the relative densities in different locations on the sample are explained by uneven packing of the powder in the mould leading to the uneven thickness of the compact. The thickness decreased from approximately 3,5 mm around location 3 to approximately 3,1 mm around location 6. It is likely that the powder did not redistribute under load during the sintering process and pressure varied significantly from location to location. The simulated density gradient from centre to the edges does not exceed 0,6 % and is significantly smaller than measured. Relative density as calculated using MSC was 0,926 at the centre of the compact. Due to the large amount of powder required for the compact no attempt was made to repeat the experiment.

The simulation also took into account compressive force from the electrodes and the thermal expansion experienced by the copper and graphite parts. The simulation works on strains in elastic area, however thermal expansion can cause the strains to significantly exceed the elastic strain limits. Simulating plastic deformation is out of scope of this work thus the stresses shown by the simulation should be used in qualitative manner. Figure 57 shows the simulated stress exceeding 500 MPa inside the compact while the graphite die experienced stresses up to 135 MPa. According to the simulation the stresses exceeded the yield strength of the copper, thus plastic deformation should happen and prevent the stresses from increasing. However the

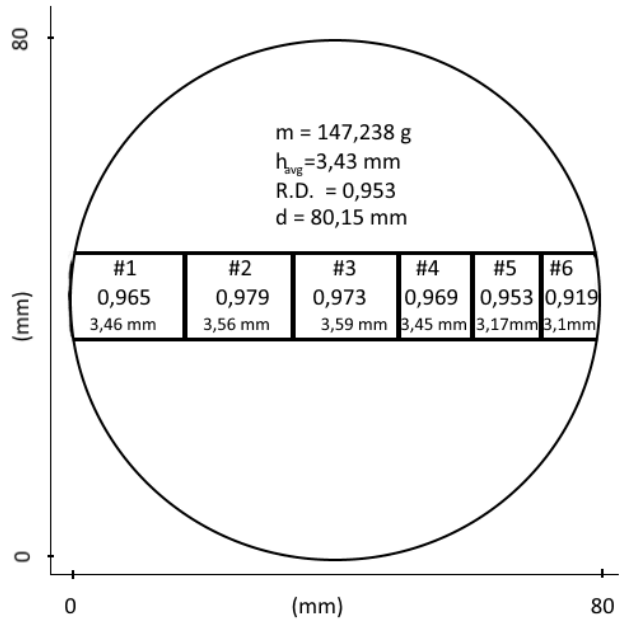

Figure 56: A schematic drawing of the compact with relative densities and heights associated to different positions included.

simulation is not capable of this and the resulting stresses are exceedingly large. Should a material with higher yield strength and CTE compared to the properties of ISO-63 graphite be sintered the stresses caused by thermal expansion may cause the die to crack.

7.2.3 Morphology of Copper Powder

The copper powder was examined by SEM, Figure 58 shows that the morphology of the particles is not uniform, with significant portion of the particles showing large surface area due to their string-like structure. The morphology of the powder may partially explain the final porosity of the compacts and why the powder did not redistribute more evenly during the PECS of the 80 mm diameter compact.

7.3 Processing of Compacts with Complex Shapes

Two different geometries were sintered out of WC-12Co, one with dome shaped (sample #1) top and one with and angled protrusion on the top (sample #2) . Densities of both compacts were measured, the results shown in Table 11 indicate that both compacts reached full densities and the small variations are explained by possible heterogeneity of the powder. Immediately after removing the sample #2 from

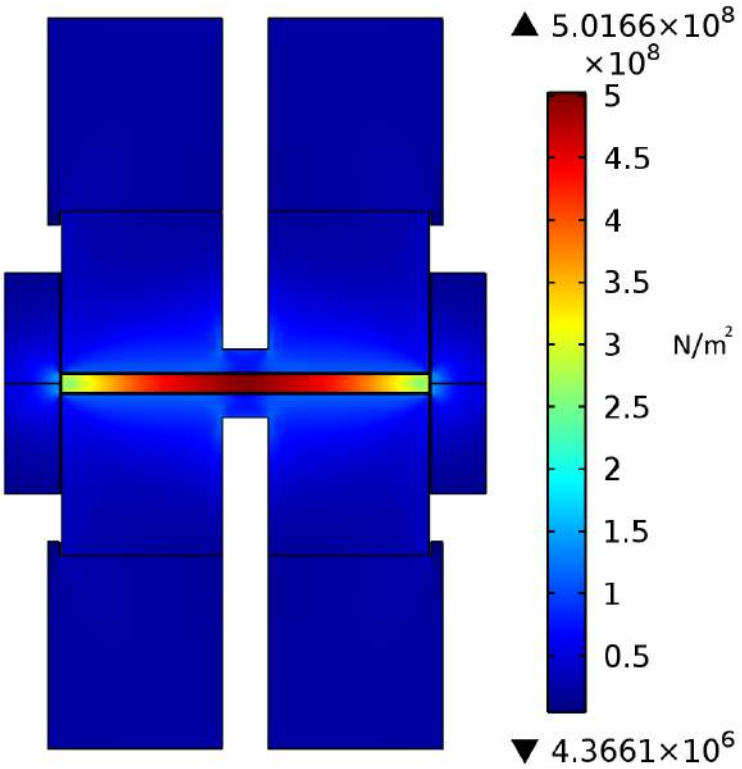

Figure 57: Simulated stress distribution during PECS of 80 mm copper disk.

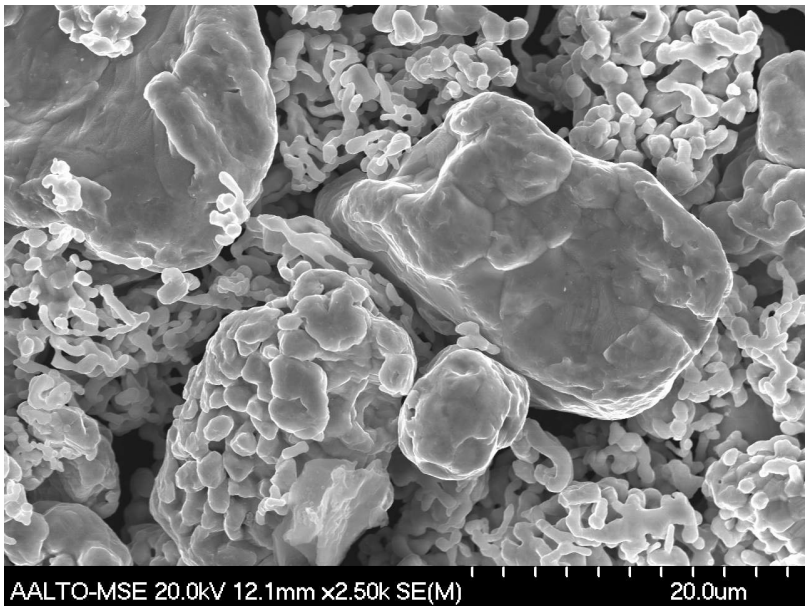

Figure 58: A SEM micrograph of the copper powder used in sintering of the copper compacts.

the PECS apparatus it became apparent that the punch with the depression had cracked along the bottom corner of the depression in multiple places, the direction of the cracks indicate that the force that caused the cracks was directed outwards in radial direction. Photograph of the punch and sample can be seen in Figure 59.

Table 11: The densities and relative densities of complex shaped sintered WC-12Co compacts.

Sample	Density (g/cm^3)	R.D.
Theoretical	14,330	1
Rounded (#1)	14,314	0,999
Edged (#2)	14,332	1,000

Figure 59: A Cracked punch and the WC-12Co compact which caused the crack.

Stress during the process was simulated in an attempt to understand the cause of the cracks. Using the value for thermal expansion of WC-12Co supplied by the materials database of the modelling software indicated that the crack location had increased stress, however the stress did not exceed 60 MPa which is safely within the tolerance of the graphite. Further investigation of literature found larger values for the CTE of the WC-12Co, largest of these was 11.7 $\times 10^{-6}$/ °C, almost twice of the

value used by the materials database. Using the high value for CTE in simulation produced stress values that significantly exceeded the elastic bounds of the materials, and even an arbitrarily chosen 20 % increase from the original CTE value produced high enough stress to crack the graphite. A comparison between stress surrounding the compact using both the (a) database value and the (b) value from literature is shown in Figure 60. While neither simulation result is likely to be accurate they show the locations of high stresses in the graphite and indicate potential points of failure.

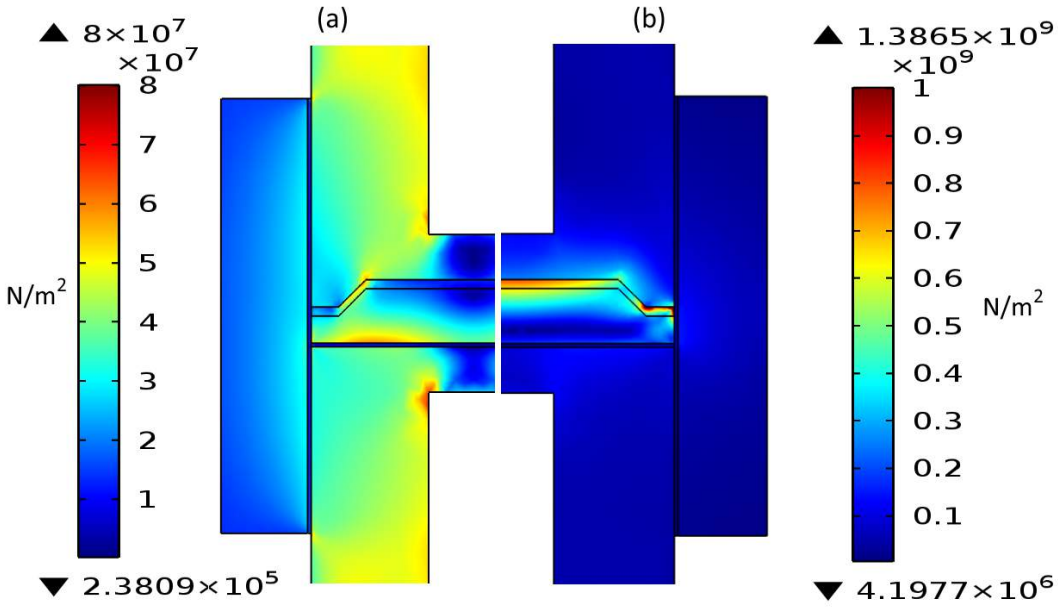

Figure 60: Simulation of the stress during sintering of sample #2 using CTE (a) supplied by comsol and (b) from literature.

While the punch in the case of sample #2 survived the sintering process unharmed, the lip around the bowl shape sheared off during detaching of the compact because of the strong adhesion between the WC-12Co, sprayed on BN and the graphite. Figure 61 shows the punch and compact after sintering.

The fact that the punch did not crack due to thermal expansion is borne out by simulations, the results show that the dome shape distributes the stress more evenly. Figure 62 (a) using the Comsol supplied value for CTE indicates that the bowl shaped punch doesn't exceed 40 MPa in stress near the compact and while (b) using the value chosen from literature indicates that the stress is relatively equally distributed and that there exists excessive stress in the compact, peaking at the upper corner.

Table 12 lists the results of hardness measurements performed on the compacts.

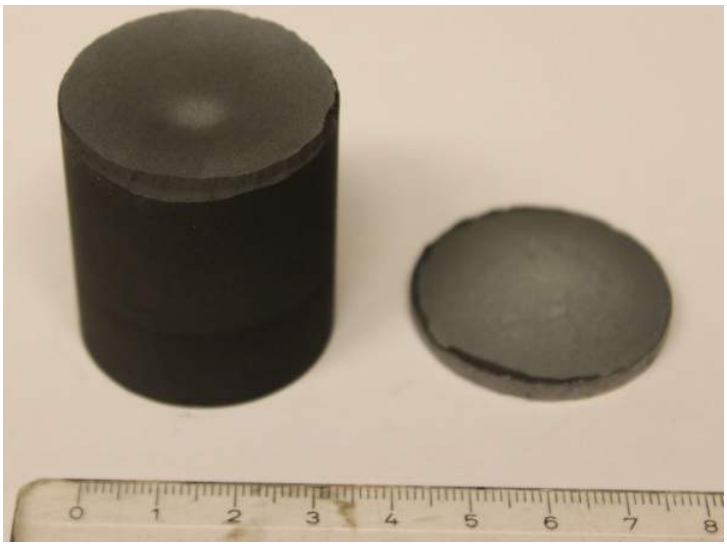

Figure 61: Punch and compact after sintering of the dome topped sample.

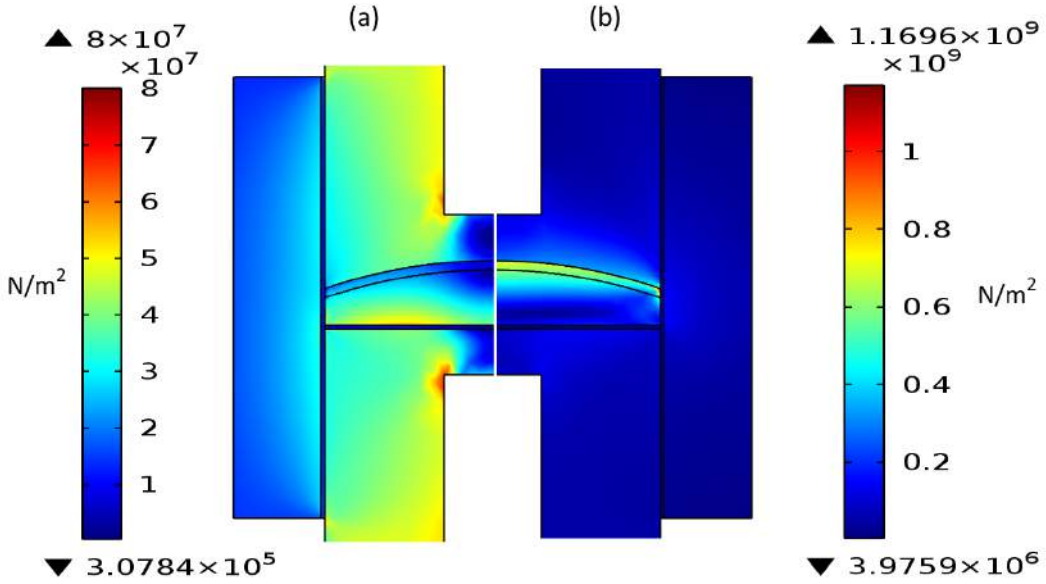

Figure 62: Simulation of the stress during sintering of sample #1 using CTE (a) supplied by comsol and (b) from literature.

Cross-sections of both samples were subjected to Vickers hardness tests using 4 kgf of applied force. The hardness measurements were repeated around the cross-sections and no discernible trends were established. Due to very little difference in the lengths of the diagonals, the samples were likely level. Figure 63 shows an example indentation performed on sample #2.

Cross-sectional investigation of the samples by SEM did not reveal any notable differences in their microstructures. No cracks were detected at locations where

Table 12: The Vickers hardness values of complex shaped sintered WC-12Co samples.

Sample	HV_{avg}	HV_{max}	HV_{min}	St.Dev.
#1	1534	1565	1502	22,00
#2	1530	1598	1489	30,05

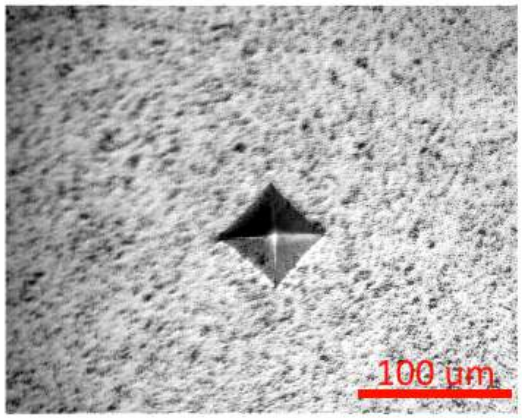

Figure 63: An optical micrograph showing a Vickers indent on the surface of the sample #2.

simulations indicated heightened stress levels. Figure 64 shows micrographs taken at 10k and 25k magnifications from both samples.

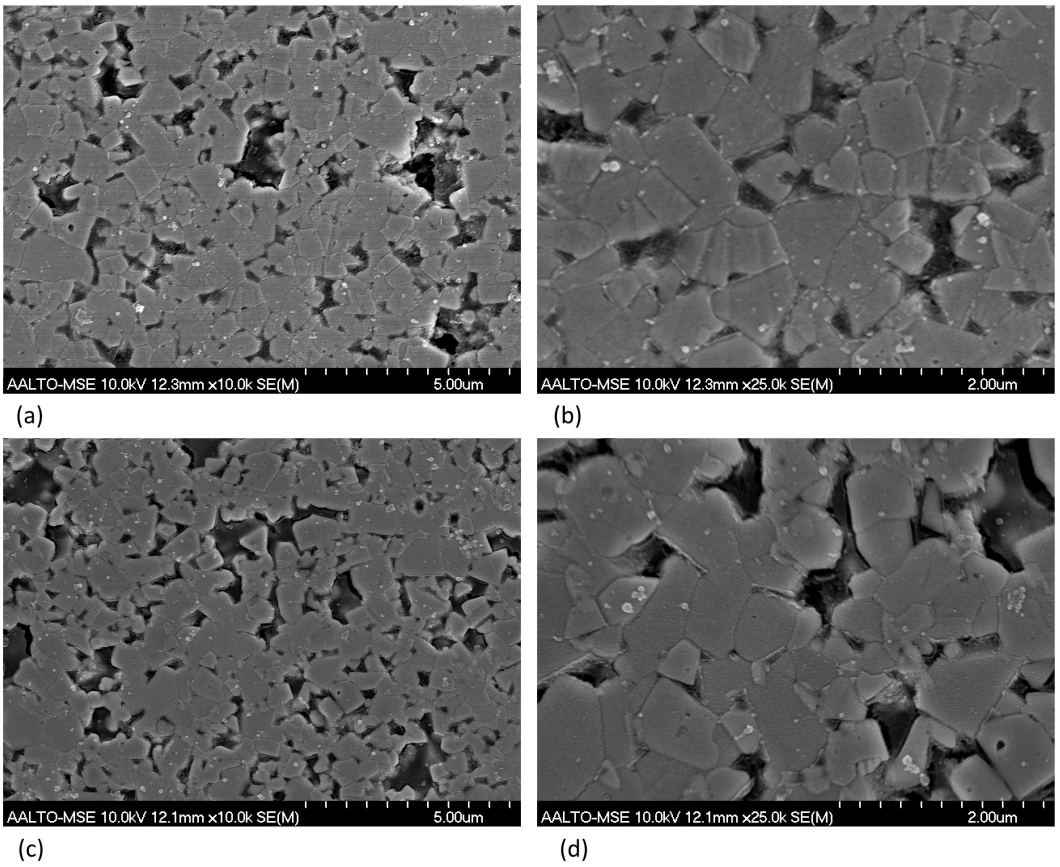

Figure 64: SEM micrographs illustrating the microstructures of the WC-12Co compacts #1 (a,b) and #2 (c,d).

8 Discussion

8.1 The FEM Simulations

Accurate determination of electrical and thermal properties of the graphite components used in PECS was of utmost importance as they affect both the heat generation and transfer. Electrical resistivity and conductivity of the ISO-63 graphite were measured inside the PECS furnace at various stable temperatures. Multiple repetitions of the experiment both removed the possibility of residual volatiles in the graphite from affecting the results and eliminate possibly poor contact quality from affecting the results. The measured values were comparable to those found in literature [56]. Accuracy in the resistivity measurement is important as the amount of heat generated by Joule heating is dependent on it. Electrical properties of graphite foil were determined from literature, experiments and modelling. It was found that the conductivity of graphite changed significantly when placed vertically, which was also supported by literature [56].

Thermal conductivity for the ISO-63 graphite was calculated from thermal diffusivity measured using the laser flash method and specific heat chosen from literature. The calculated thermal conductivity (Table 6) was both higher and lower than values found in literature [47, 54, 56] for other graphite varieties used in PECS. No values were found for the thermal conductivity of ISO-63 graphite in literature outside of room temperature [58] for direct comparison. A comparison to the room temperature value of 70 W/mK to 91 W/mK measured and calculated for 100 °C indicates that graphite batches should be tested individually for their properties to increase the accuracy of simulations.

Convective cooling of the system was simplified to the graphite-electrode interface and determined by finding a coefficient using trial and error that resulted in the best match with experimentally measured temperature profiles during multiple stable temperatures. The convective cooling coefficient depends significantly on the used equipment and has to be determined on a case by case basis. Similar values were found in literature [56] as were significantly different values [54]. The model also dissipates heat using emissivity, literature was in agreement on the value 0.8 for it [48, 50, 51, 56].

The first models were built as stationary, thus they best correspond to stabilized conditions during dwell times. The models were useful as a comparison in validation of the experimentally measured properties. To more accurately match real world conditions PID control was simulated for the heating phase. PID control allows the

use of set heating rates similarly to the PECS furnace. The simulated PID controller was quicker to react to temperature changes than the PECS furnace and thus had smaller temperature overshoots when reaching the dwell stage. The difference between the PID controller reaction times were caused by the latency in temperature measurements from thermocouples and pyrometer.

Validation of the simulation parameters and materials properties was performed using a comparison between simulated and experimentally measured data from PECS of solid α-alumina and copper samples. The agreement between experimental and simulated results was good. Behaviour of the simulated current densities from the centre of the samples to radial surface of the die were similar to those found in literature [47].

Thermal insulation around the die can be used to decrease temperature gradients in the sample [48]. Use of graphite felt as thermal insulator was simulated and experimented on. Both simulated and experimental results showed marked decrease in power consumption due to lower heat losses. The simulation results also demonstrated significantly smaller temperature gradients.

8.2 PECS Compactions

Densification of copper was modelled using the Master Sintering Curve (MSC) to predict its relative density at a known time and temperature. The MSC was constructed using experimentally measured densification rates at two heating rates and validated against a different heating rate. The resulting function for relative density was integrated into the FEM simulation. The small thermal gradients simulated during sintering of the copper samples produced no significant density variations, however the thermal gradients are larger when sintering high temperature materials. The closer the heating rate is to those used in construction of the MSC the more accurate the predicted relative density.

A 80 mm diameter copper disk was modelled and sintered. The model indicated density variations below 10 kg/m^3. The sintered compact had significantly larger density variations. This was likely caused by uneven packing of powder inside the die before sintering evidenced by the significant thickness variations in the sample. The simulation resulted in stresses beyond structural integrity of the graphite die. The high stress values were result of the model being limited to simulation of elastic behaviour and plastic deformation of the copper was not taken into account. The simulated high stresses caused by thermal expansion should be considered if sintering substances harder than the graphite die with larger CTE's.

Two different compacts with complex geometries were both simulated and sintered from WC-12Co. The compacts were fully dense, no difference was observed in their microstructures or hardness. The hardness was also constant regardless of the location on the sample. During sintering the compact with angled step broke a punch used in the sintering, this was likely caused by thermal expansion and the lack of graphite paper to mitigate it. Simulation results indicated high stress concentration at the crack locations. A stronger graphite variety may be one way to avoid the cracking. The punches used in sintering of the dome topped compact stayed intact during sintering indicating different stress distribution, as did simulation results. However the thin lip of the punch cracked during detaching of the sample, this cracking could've been avoided by different design of the punch and die setup.

9 Conclusions

Pulsed electric current sintering was modelled using the finite element method. Both stationary and time dependent models were built. Models were built with thermo–electrical and thermo–electrical–mechanical couplings. The mechanical simulations were limited to elastic behaviour of materials. Master sintering curve was constructed for prediction of relative density of copper and integrated into the simulation. Materials properties and modelling parameters were determined from literature or by a combination of experiments and modelling.

The simulations measured evolution and/or distribution of temperature, current density, voltage, thermal expansion, stress and density. Simulated results were compared to ones obtained experimentally. Accurate simulation results of temperature, current and voltage evolutions and distributions were obtained. The simulated mechanical stresses were useful for qualitative analysis. The simulated density evolution using MSC corresponded well with experimentally measured results.

Temperature gradients could be affected by changing the geometry of the die or by using graphite felt for thermal insulation. While enlarging the die increases electricity usage due to the volumetric nature of Joule heating the graphite felt decreases the electricity usage.

Two complex shaped WC-12Co compacts were sintered to full density at 1180 °C and simulated. In case of the compact with angled step the sintering resulted in a cracked graphite punch likely caused by stress due to thermal expansion. The simulation results displayed stress concentration in the location of the crack. The dome shaped compact had more equally distributed stress and the punches used in its sintering stayed intact.

This thesis shows that accurate materials properties and sintering parameters are a necessity for accurate simulation results. Modelling can be used to predict and avoid problems caused by temperature or stress gradients in production. In the future numerical models that can simulate the behaviour of powders during PECS are desirable, however complex.

References

[1] ASM International Handbook Committee, ed., *ASM Handbook, Volume 07 - Powder Metal Technologies and Applications*. ASM International, 1998.

[2] R. M. German, *Sintering theory and practice*. Wiley-VCH, 1996.

[3] R. Cahn and P. Haasen, *Physical Metallurgy*, vol. 3. North-Holland, 1996.

[4] H. Lee and R. F. Speyer, "Pressureless sintering of boron carbide," *Journal of the American Ceramic Society*, vol. 86, no. 9, pp. 1468–1473, 2003.

[5] E. T. Turkdogan, *Fundamentals of steelmaking*. Institute of Materials London, 1996.

[6] S.-J. L. Kang, *Sintering: densification, grain growth and microstructure*. Butterworth-Heinemann, 2004.

[7] R. M. German, P. Suri, and S. J. Park, "Review: liquid phase sintering," *Journal of Materials Science*, vol. 44, no. 1, pp. 1–39, 2009.

[8] R. Prummer, "Explosive compaction of powders, principle and prospects," *Materialwissenschaft und Werkstofftechnik*, vol. 20, no. 12, pp. 410–415, 1989.

[9] M. Rahaman, *Ceramic Processing and Sintering*. Materials Engineering, Taylor & Francis, 2003.

[10] T. Kimura, T. Yoshimoto, N. Iida, Y. Fujita, and T. Yamaguchi, "Mechanism of grain orientation during hot-pressing of bismuth titanate," *Journal of the American Ceramic Society*, vol. 72, no. 1, pp. 85–89, 1989.

[11] D. E. Clark and W. H. Sutton, "Microwave processing of materials," *Annual Review of Materials Science*, vol. 26, no. 1, pp. 299–331, 1996.

[12] A. G. Bloxam, "Improved manufacture of electric incandescent lamp filaments from tungsten or molybdenum or an alloy thereof," 1906. GB Patent 27,002.

[13] D. Egan and S. Melody, "EDS as a method of manufacturing diamond tools," *Metal Powder Report*, vol. 64, no. 6, pp. 10–36, 2009.

[14] R. Orrú, R. Licheri, A. M. Locci, A. Cincotti, and G. Cao, "Consolidation/synthesis of materials by electric current activated/assisted sintering," *Materials Science and Engineering: R: Reports*, vol. 63, pp. 127 – 287, 2009.

[15] U. Anselmi-Tamburini, J. Garay, and Z. A. Munir, "Fast low-temperature consolidation of bulk nanometric ceramic materials," *Scripta Materialia*, vol. 54, no. 5, pp. 823–828, 2006.

[16] K. Inoue, "Electric discharge heat treatment of metals in electrolytes," 1965. US Patent 3,188,245.

[17] P. Mondalek, *Numerical modeling of the spark plasma sintering process*. PhD thesis, l'École nationale supérieure des mines de Paris, December 2012.

[18] Z. A. Munir, U. Anselmi-Tamburini, and M. Ohyanagi, "The effect of electric field and pressure on the synthesis and consolidation of materials: A review of the spark plasma sintering method.," *Journal of Materials Science*, vol. 41, no. 3, pp. 763 – 777, 2006.

[19] O. Guillon, J. Gonzalez-Julian, B. Dargatz, T. Kessel, G. Schierning, J. Rathel, and M. Herrmann, "Field-assisted sintering technology/spark plasma sintering: Mechanisms, materials, and technology developments," *Advanced Engineering Materials*, vol. 16, no. 7, pp. 830–849, 2014.

[20] W. Chen, U. Anselmi-Tamburini, J. Garay, J. Groza, and Z. Munir, "Fundamental investigations on the spark plasma sintering/synthesis process: I. effect of dc pulsing on reactivity," *Materials Science and Engineering: A*, vol. 394, pp. 132 – 138, 2005.

[21] G. Xie, O. Ohashi, K. Chiba, N. Yamaguchi, M. Song, K. Furuya, and T. Noda, "Frequency effect on pulse electric current sintering process of pure aluminum powder," *Materials Science and Engineering: A*, vol. 359, no. 2, pp. 384 – 390, 2003.

[22] U. Anselmi-Tamburini, J. Garay, and Z. Munir, "Fundamental investigations on the spark plasma sintering/synthesis process: III. Current effect on reactivity," *Materials Science and Engineering: A*, vol. 407, pp. 24 – 30, 2005.

[23] J. G. Santanach, C. Estournes, A. Weibel, G. Chevallier, V. Bley, C. Laurent, and A. Peigney, "Influence of pulse current during spark plasma sintering evidenced on reactive alumina–hematite powders," *Journal of the European Ceramic Society*, vol. 31, no. 13, pp. 2247–2254, 2011.

[24] J. Garay, U. Anselmi-Tamburini, and Z. A. Munir, "Enhanced growth of intermetallic phases in the Ni–Ti system by current effects," *Acta Materialia*, vol. 51, no. 15, pp. 4487–4495, 2003.

[25] Z. A. Munir, D. V. Quach, and M. Ohyanagi, "Electric current activation of sintering: A review of the pulsed electric current sintering process," *Journal of the American Ceramic Society*, vol. 94, no. 1, pp. 1–19, 2011.

[26] Y. Makino, M. Sakaguchi, J. Terada, and K. Akamatsu, "Consolidation of ultrafine alumina powders with SPS method," *Journal of the Japan Society of Powder and Powder Metallurgy*, vol. 54, no. 4, pp. 219–225, 2007.

[27] D. V. Quach, H. Avila-Paredes, S. Kim, M. Martin, and Z. A. Munir, "Pressure effects and grain growth kinetics in the consolidation of nanostructured fully stabilized zirconia by pulsed electric current sintering," *Acta Materialia*, vol. 58, no. 15, pp. 5022 – 5030, 2010.

[28] K. Chen, X. Zhang, H. Wang, L. Zhang, J. Zhu, F. Yang, and L. An, "Making nanostructured ceramics from micrometer-sized powders via grain refinement during sps sintering," *Journal of the American Ceramic Society*, vol. 91, no. 8, pp. 2475–2480, 2008.

[29] J. G. Santanach, A. Weibel, C. Estournes, Q. Yang, C. Laurent, and A. Peigney, "Spark plasma sintering of alumina: Study of parameters, formal sintering analysis and hypotheses on the mechanism(s) involved in densification and grain growth," *Acta Materialia*, vol. 59, no. 4, pp. 1400 – 1408, 2011.

[30] E. A. Olevsky, S. Kandukuri, and L. Froyen, "Consolidation enhancement in spark-plasma sintering: Impact of high heating rates," *Journal of Applied Physics*, vol. 102, no. 11, pp. 114913–114913, 2007.

[31] M. Tokita, "Development of large-size ceramic/metal bulk FGM fabricated by spark plasma sintering," in *Materials Science Forum*, vol. 308, pp. 83–88, Trans Tech Publ, 1999.

[32] D. M. Hulbert, A. Anders, J. Andersson, E. J. Lavernia, and A. K. Mukherjee, "A discussion on the absence of plasma in spark plasma sintering," *Scripta Materialia*, vol. 60, no. 10, pp. 835 – 838, 2009.

[33] O. Yanagisawa, H. Kuramoto, K. Matsugi, and M. Komatsu, "Observation of particle behavior in copper powder compact during pulsed electric discharge," *Materials Science and Engineering: A*, vol. 350, no. 1, pp. 184–189, 2003.

[34] D. Jiang, D. M. Hulbert, J. D. Kuntz, U. Anselmi-Tamburini, and A. K. Mukherjee, "Spark plasma sintering: A high strain rate low temperature forming tool for ceramics," *Materials Science and Engineering: A*, vol. 463, pp. 89 – 93, 2007.

[35] T. Sasaki, T. Ohkubo, and K. Hono, "Microstructure and mechanical properties of bulk nanocrystalline Al-Fe alloy processed by mechanical alloying and spark plasma sintering," *Acta Materialia*, vol. 57, no. 12, pp. 3529 – 3538, 2009.

[36] S. Wei, Z.-H. Zhang, X.-B. Shen, F.-C. Wang, M.-Y. Sun, R. Yang, and S.-K. Lee, "Simulation of temperature and stress distributions in functionally graded materials synthesized by a spark plasma sintering process," *Computational Materials Science*, vol. 60, no. 0, pp. 168 – 175, 2012.

[37] C. Ramirez, S. M. Vega-Diaz, A. Morelos-Gomez, F. M. Figueiredo, M. Terrones, M. I. Osendi, M. Belmonte, and P. Miranzo, "Synthesis of conducting graphene/Si3N4 composites by spark plasma sintering," *Carbon*, vol. 57, pp. 425–432, 2013.

[38] A. Bellosi, F. Monteverde, and D. Sciti, "Fast densification of ultra-high-temperature ceramics by spark plasma sintering," *International Journal of Applied Ceramic Technology*, vol. 3, no. 1, pp. 32–40, 2006.

[39] D. M. Hulbert, D. Jiang, D. V. Dudina, and A. K. Mukherjee, "The synthesis and consolidation of hard materials by spark plasma sintering," *International Journal of Refractory Metals and Hard Materials*, vol. 27, no. 2, pp. 367–375, 2009.

[40] S. I. Cha and S. H. Hong, "Microstructures of binderless tungsten carbides sintered by spark plasma sintering process," *Materials Science and Engineering: A*, vol. 356, no. 1, pp. 381–389, 2003.

[41] M. Omori, "Sintering, consolidation, reaction and crystal growth by the spark plasma system (SPS)," *Materials Science and Engineering: A*, vol. 287, no. 2, pp. 183–188, 2000.

[42] B.-N. Kim, K. Hiraga, K. Morita, and H. Yoshida, "Spark plasma sintering of transparent alumina," *Scripta Materialia*, vol. 57, no. 7, pp. 607–610, 2007.

[43] N. Mahmed, O. Heczko, R. Maki, O. Söderberg, E. Haimi, and S. Hannula, "Novel iron oxide–silica coreshell powders compacted by using pulsed electric current sintering: Optical and magnetic properties," *Journal of the European Ceramic Society*, vol. 32, no. 11, pp. 2981–2988, 2012.

[44] O. Zienkiewicz, J. Zhu, and Z. Taylor, *The Finite Element Method: Its Basis And Fundamentals 6th ed.* Butterworth-Heinemann, 2005.

[45] J. Reddy and D. Gartling, *The Finite Element Method in Heat Transfer and Fluid Dynamics, Second Edition.* Computational Mechanics and Applied Analysis, Taylor & Francis, 2000.

[46] S. Rao, *The Finite Element Method in Engineering.* Elsevier Science, 2011.

[47] U. Anselmi-Tamburini, S. Gennari, J. Garay, and Z. Munir, "Fundamental investigations on the spark plasma sintering/synthesis process: II. Modeling of current and temperature distributions," *Materials Science and Engineering: A*, vol. 394, pp. 139 – 148, 2005.

[48] B. McWilliams, A. Zavaliangos, K. Cho, and R. Dowding, "The modeling of electric-current-assisted sintering to produce bulk nanocrystalline tungsten," *JOM*, vol. 58, no. 4, pp. 67–71, 2006.

[49] K. Vanmeensel, A. Laptev, J. Hennicke, J. Vleugels, and O. V. der Biest, "Modelling of the temperature distribution during field assisted sintering," *Acta Materialia*, vol. 53, no. 16, pp. 4379 – 4388, 2005.

[50] A. Pavia, L. Durand, F. Ajustron, V. Bley, G. Chevallier, A. Peigney, and C. Estournes, "Electro-thermal measurements and finite element method simulations of a spark plasma sintering device," *Journal of Materials Processing Technology*, vol. 213, no. 8, pp. 1327 – 1336, 2013.

[51] J. Allen and C. Walter, "Numerical simulation of the temperature and stress field evolution applied to the field assisted sintering technique," *ISRN Materials Science*, vol. 2012, pp. 1–9, 2012.

[52] C. Wang, L. Cheng, and Z. Zhao, "FEM analysis of the temperature and stress distribution in spark plasma sintering: Modelling and experimental validation," *Computational Materials Science*, vol. 49, no. 2, pp. 351 – 362, 2010.

[53] C. Wolff, S. Mercier, H. Couque, and A. Molinari, "Modeling of conventional hot compaction and spark plasma sintering based on modified micromechanical models of porous materials," *Mechanics of Materials*, vol. 49, pp. 72 – 91, 2012.

[54] A. Cincotti, A. M. Locci, R. Orru, and G. Cao, "Modeling of SPS apparatus: Temperature, current and strain distribution with no powders," *AIChE Journal*, vol. 53, no. 3, pp. 703–719, 2007.

[55] E. A. Olevsky, C. Garcia-Cardona, W. L. Bradbury, C. D. Haines, D. G. Martin, and D. Kapoor, "Fundamental aspects of spark plasma sintering: II. Finite element analysis of scalability," *Journal of the American Ceramic Society*, vol. 95, no. 8, pp. 2414–2422, 2012.

[56] K. Vanmeensel, *Field Assisted Sintering of Zirconia-Based, Electrically Conductive Ceramic Composites*. PhD thesis, Katholieke Universiteit Leuven, May 2007.

[57] B. McWilliams and A. Zavaliangos, "Multi-phenomena simulation of electric field assisted sintering," *Journal of Materials Science*, vol. 43, no. 14, pp. 5031–5035, 2008.

[58] Svenska Tanso AB, "ISO-63 graphite datasheet."

[59] R. Sheppard, D. Morgan, D. Mathes, and D. Bray, "Properties and characteristics of graphite for the EDM industry," February 2002.

[60] SGL CARBON GmbH, "Flexible carbon and graphite felts for the thermal insulation of high-temperature furnaces," 2004.

[61] Carbon Composites, Inc., "Thermshield soft graphite felt datasheet."

[62] CARBONE LORRAINE COMPOSANTS, "Papyex flexible graphite."

[63] K. J. Astrom and R. M. Murray, *Feedback systems: An introduction for scientists and engineers*. Princeton University Press, 2010.

[64] H. Su and D. L. Johnson, "Master sintering curve: A practical approach to sintering," *Journal of the American Ceramic Society*, vol. 79, no. 12, pp. 3211–3217, 1996.

[65] M.-H. Teng, Y.-C. Lai, and Y.-T. Chen, "A computer program of master sintering curve model to accurately predict sintering results," *Western Pacific Earth Sciences*, vol. 2, no. 2, pp. 171 – 180, 2002.

[66] M. Engler, C. Lesniak, R. Damasch, B. Ruisinger, and J. Eichler, "Hexagonal boron nitride (hBN): Applications from metallurgy to cosmetics," in *CFI. Ceramic Forum International*, vol. 84, Goller, 2007.

[67] K. Bauer, D. Garbe, and H. Surburg, "Ullmann's encyclopedia of industrial chemistry," *Ullmann's Encyclopedia of Industrial Chemistry*, vol. 11, 1988.

[68] S. Huang, K. Vanmeensel, L. Li, O. Van der Biest, and J. Vleugels, "Tailored sintering of VC-doped WC–Co cemented carbides by pulsed electric current sintering," *International Journal of Refractory Metals and Hard Materials*, vol. 26, no. 3, pp. 256–262, 2008.